RYDBERG EXCITONS IN CUPROUS OXIDE

MACROSCOPIC QUANTUM SYSTEMS COUPLED TO NANOPLASMONIC AND NANOPHOTONIC COMPONENTS

ANNIKA NEUBAUER

4. Physikalisches Institut der Universität Stuttgart
Oktober 2022

Universität Stuttgart

RYDBERG EXCITONS IN CUPROUS OXIDE
MACROSCOPIC QUANTUM SYSTEMS COUPLED TO NANOPLASMONIC AND NANOPHOTONIC COMPONENTS

Von der Fakultät Mathematik und Physik
der Universität Stuttgart zur Erlangung der Würde
eines Doktors der Naturwissenschaften (Dr. rer. nat.)
genehmigte Abhandlung

vorgelegt von

ANNIKA NEUBAUER, *geb.* KONZELMANN

aus Böblingen

Hauptberichter:	Prof. Dr. Harald Giessen
Mitberichter:	Prof. Dr. Peter Michler
Prüfungsvorsitzende:	Prof. Dr. Maria Daghofer

Tag der mündlichen Prüfung: 30. November 2022

4. Physikalisches Institut der Universität Stuttgart
Oktober 2022

To my family.

Kinder müssen mit den Erwachsenen viel Geduld haben.
(Antoine de Saint-Exupéry)

ABSTRACT

A Rydberg exciton is an exciton that is in a state with large principal quantum number n. Similar to Rydberg atoms, highly-excited Rydberg excitons have properties that are very different from their ground-state counterpart. The semiconductor cuprous oxide (Cu_2O, cuprite), having a Rydberg binding energy of 96 meV, is perfectly suited for the formation of such excitons. The $1/n^2$-dependency of the exciton binding energy impressively emphasizes the quantum mechanical analogy between excitons and the hydrogen atom. Excitons in cuprous oxide can be conveniently investigated with light in the visible range.

In contrast to Rydberg atoms, Rydberg excitons are embedded in a semiconductor, making them the first Rydberg system in a solid. As cuprous oxide is a covalent crystal, the electron-hole pair is loosely bound, spreading over 10 billion crystal unit cells. The exciton radii for principal quantum numbers around $n = 20$ are in the µm-range, making Rydberg excitons in cuprous oxide mesoscopic quantum objects. Due to their giant size, Rydberg excitons are highly sensitive to nearby charges or atoms, rendering them ideal solid-state quantum sensors. They could even be engaged as building blocks for quantum computers.

The aim of this thesis is to investigate Rydberg excitons in cuprous oxide with respect to their application for quantum systems. The key prerequisite for such studies, are high-quality cuprous oxide crystals, which are available from natural occurrences in different mines across the world. For the realization of an integrated and scalable solid state quantum device, Rydberg

excitons in Cu_2O are combined with nanoplasmonic and nanophotonic components, such as plasmonic antennas, quantum wells, and orbital angular momentum (OAM) light, in order to bring together nanophotonics and macroscopic quantum systems.

Orbital angular momentum light possesses in addition to its normal helicity ($s = \pm\hbar$, depending on its circular polarization) an orbital angular momentum l. This means that in principle one can transfer more than a single quantum of $\hbar$ during an optical transition from light to a quantum system. However, quantum objects are usually so small (typically in the nanometer range) that they only locally probe the dipolar character of the local electric field. In order to sense the complete macroscopic electric field, we utilize Rydberg excitons in the semiconductor cuprite, which are single quantum objects of up to micrometer size. Their interaction with focused OAM light allows for matching the focal spot size and the wave-function diameter. Here, the common dipole selection rules ($j = s + l = \pm 1$) should be broken, and transitions of higher angular momentum j with higher-order OAM states should become more probable. Based on group theory, we analyze in detail the optical selection rules governing this process. Then we are able to predict what kind of alternative exciton transitions, characterized by principal quantum number n and orbital angular momentum quantum number l^{exc}, one would expect in absorption spectroscopy on Cu_2O using different kinds of OAM light.

The excitation of different principal and angular momentum quantum number state excitons can be achieved by light engineering. This includes not only the use of orbital angular momentum light, but also of plasmonic nanoantennas. Plasmonic antennas channel incoming light into a confined nearfield that comes along with strong field gradients at the edges. Transverse field gradients are capable of driving quadrupole transitions in a more effective way than the weak longitudinal field gradient in dipolar light.

Cuprous oxide Rydberg excitons with principal quantum number n between 5 and 15 are several tens to a few hundreds of nanometers in diameter and can have different OAM quantum numbers l^{exc}. Usually, only P- and F-excitons ($l^{\text{exc}} = 1, 3$) are electric dipole-allowed, while S- and D-excitons ($l^{\text{exc}} = 0, 2$) remain dark. We use 30 nm wide and 60 to 110 nm long plasmonic aluminum nanoantennas deposited on the cuprous oxide crystal surface to create transverse field gradients in similar spatial dimensions as the size of Rydberg excitons. This way, light field and matter wave function overlap spatially and quadrupole transitions of S-excitons are enhanced.

The mesoscopic size of Rydberg excitons allows for a size match with the OAM or plasmonic light field. It is also advantageous for quantum confinement. We propose first steps towards calculating the energy shifts of confined Rydberg excitons in Cu_2O quantum wells, wires, and dots. The macroscopic size of Rydberg excitons with high quantum numbers n implies that already µm-sized lamellar, wire-like, or box-like structures lead to quantum size effects, which depend on the principal quantum number n. Such structures can be fabricated using focused ion beam milling of cuprite crystals. Quantum confinement causes an energy shift of the confined object, which is attractive for quantum technology. We find in our calculations that the Rydberg excitons gain potential energy in the µeV to meV-range due to quantum confinement. This effect is dependent on the Rydberg exciton size and, thus, the principal quantum number n. The calculated energy shifts in the µeV to meV energy range should be experimentally accessible and detectable.

ZUSAMMENFASSUNG

Ein Rydbergexziton ist ein Exziton in einem hoch-angeregten Zustand mit großer Hauptquantenzahl n. Ähnlich wie Rydbergatome haben hochangeregte Rydbergexzitonen Eigenschaften, die sich stark von denen ihres Grundzustands unterscheiden. Der Halbleiter Kupferoxydul (Cu_2O, Cuprit) ist mit einer Rydberg-Bindungsenergie von 96 meV für die Anregung von Exzitonen besonders geeignet. Die $1/n^2$-Abhängigkeit der Exzitonen-Bindungsenergie zeigt eindrucksvoll die quantenmechanische Analogie zwischen Exzitonen und dem Wasserstoffatom. Energetisch erscheinen die Exzitonen in Kupferoxydul im sichtbaren Spektralbereich.
Im Gegensatz zu Rydbergatomen sind Rydbergexzitonen bereits in einem Halbleiter eingebettet und damit das erste Rydbergsystem in einem Festkörper. Da es sich bei Kupferoxydul um einen kovalenten Kristall handelt, ist das Elektron-Loch-Paar schwach gebunden und erstreckt sich über 10 Milliarden Kristalleinheitszellen. Die Exzitonenradien für Hauptquantenzahlen um $n = 20$ erreichen Werte im µm-Bereich und machen Rydbergexzitonen in Kupferoxydul zu mesoskopischen Quantenobjekten. Aufgrund ihrer gigantischen Größe reagieren Rydbergexzitonen sehr empfindlich auf nahe gelegene Ladungen oder Atome, was sie zu idealen Festkörper-Quantensensoren macht. Sie könnten auch als Bausteine für Quantencomputer eingesetzt werden.

Das Ziel dieser Arbeit ist es, Rydbergexzitonen in Kupferoxydul im Hinblick auf ihre Anwendung für Quantensysteme zu untersuchen. Die wichtigste Voraussetzung für solche Untersuchungen ist die Verfügbarkeit von hochwertigen Cupritkristallen, was durch ihr natürliches Vorkommen in verschiedenen Bergwerken weltweit

gegeben ist. Für die Realisierung von integrierten und skalierbaren Festkörper-Quantenbauelementen werden Rydbergexzitonen in Cu_2O mit nanoplasmonischen und nanophotonischen Strukturen, wie plasmonische Antennen, Quantentöpfe, und Bahndrehimpulslicht, kombiniert, um Nanophotonik und makroskopische Quantensysteme zusammenzubringen.

Bahndrehimpulslicht besitzt zusätzlich zu seiner normalen Helizität ($s = \pm\hbar$, abhängig von seiner Zirkularpolarisation) einen Bahndrehimpuls l. Das bedeutet, dass man bei einem optischen Übergang im Prinzip mehr als ein einzelnes Quant $\hbar$ von Licht auf ein Quantensystem übertragen kann. Jedoch sind Quantenobjekte in der Regel so klein (typischerweise im Nanometerbereich), dass sie nur lokal den dipolaren Charakter des lokalen elektrischen Feldes nachweisen. Um das gesamte makroskopische elektrische Feld zu erfassen, nutzen wir Rydbergexzitonen im Halbleiter Cuprit, bei denen es sich um einzelne Quantenobjekte von bis zu einem Mikrometer Größe handelt. Ihre Wechselwirkung mit fokussiertem Bahndrehimpulslicht ermöglicht es, die Größe von Licht- und Materiewellenfunktion aufeinander abzustimmen. Dabei sollten die üblichen Dipol-Auswahlregeln ($j = s + l = \pm 1$) gebrochen werden und Übergänge höherem Drehimpuls j sollten bei Anregung mit Bahndrehimpulslicht höherer Ordnung wahrscheinlicher werden. Anhand gruppentheoretischer Überlegungen analysieren wir im Detail die optischen Auswahlregeln, die diesen Prozess bestimmen. Damit sind wir in der Lage vorherzusagen, welche Art von alternativen Exzitonenübergängen, beschrieben durch Hauptquantenzahl n und Drehimpulsquantenzahl l^{exc}, man in Absorptionsspektroskopie an Cu_2O unter Verwendung verschiedener Arten von Bahndrehimpulslicht erwarten würde.

Die Anregung von Rydbergexzitonen verschiedener Haupt- und Bahndrehimpulsquantenzahlen kann durch Verändern der Lichteigenschaften erreicht werden. Dies beinhaltet nicht nur die Verwendung von Bahndrehimpulslicht, sondern auch die Nutzung plasmonischer Antennen. Plasmonische Antennen kanalisieren einfallendes Licht in ein begrenztes Nahfeld, das an den Rändern mit starken Feldgradienten einhergeht. Transversale Feldgradienten sind in der Lage, Quadrupolübergänge effektiver anzutreiben als der schwache longitudinale Feldgradient in dipolarem Licht. Rydbergexzitonen in Kupferoxydul mit einer Hauptquantenzahl n zwischen 5 und 15 haben einen Durchmesser von einigen Dutzend bis einigen Hundert Nanometern und können unterschiedliche Bahndrehimpulsquantenzahlen l^{exc} haben. Normalerweise sind nur P- und F-Exzitonen ($l^{\mathrm{exc}} = 1, 3$) für elektrische Dipolübergänge erlaubt, während S- und D-Exzitonen ($l^{\mathrm{exc}} = 0, 2$) verboten sind. Wir verwenden 30 nm breite und 60 bis 110 nm lange plasmonische Nanoantennen aus Aluminium, die auf der Oberfläche eines Kupferoxydulkristalls aufgebracht sind, um transversale Feldgradienten in ähnlichen räumlichen Dimensionen wie die Größe von Rydbergexzitonen zu erzeugen. Auf diese Weise überlappen sich Lichtfeld und Materiewellenfunktion räumlich und die Anregung von Quadrupolübergängen, also von S-Exzitonen, wird verstärkt.

Die mesoskopische Größe von Rydbergexzitonen ermöglicht eine Übereinstimmung der Größe mit dem anregenden Bahndrehimpuls- oder plasmonischen Lichtfeld. Sie ist auch für Quanteneinschränkungen von Vorteil. Wir schlagen erste Schritte zur Berechnung der Energieverschiebungen von eingeschlossenen Rydbergexzitonen in Cu_2O-Quantentöpfen, -drähten und -punkten vor. Die makroskopische Größe von Rydbergexzitonen mit hoher Hauptquantenzahl n impliziert, dass bereits µm-große lamellen-, draht- oder kastenartige Strukturen zu Quanteneffekten führen, die von der Hauptquantenzahl n abhängen. Solche Strukturen können durch fokussierte Ionenstrahllithographie von Kupritkristallen hergestellt werden.

Die Beschränkung im Quantentopf führt zu einer Energieverschiebung des eingeschlossenen Objekts, was für Quantentechnologien attraktiv ist. In unseren Berechnungen stellen wir fest, dass Rydbergexzitonen aufgrund des Quanteneinschlusses potentielle Energie im µeV- bis meV-Bereich gewinnen. Dieser Effekt ist abhängig von der Größe der Rydbergexzitonen und damit von der Hauptquantenzahl n. Die berechneten Energieverschiebungen im µeV- bis meV-Energiebereich sollten experimentell zugänglich und nachweisbar sein.

PUBLICATIONS

JOURNAL PUBLICATIONS RELEVANT FOR THIS THESIS

P1 A. Konzelmann, S.-O. Krüger, and H. Giessen,
"Interaction of orbital angular momentum light with Rydberg excitons: Modifying dipole selection rules,"
Phys. Rev. B **100**, 115308 (2019).

P2 A. Konzelmann, B. Frank, and H. Giessen,
"Quantum confined Rydberg excitons in reduced dimensions,"
J. Phys. B **53**, 024001 (2019).

P3 A. Neubauer, J. Heckötter, M. Ubl, M. Hentschel, B. Panda, M. Aßmann, M. Bayer, and H. Giessen,
"Spectroscopy of nanoantenna-covered Cu_2O: Towards enhancing quadrupole transitions in Rydberg excitons,"
Phys. Rev. B **106**, 165305 (2022).

PUBLICATIONS THAT ARE NOT PART OF THIS THESIS

P4 A. Konzelmann, H. Charaya, B. Gompf, M. Dressel, and A. Berrier,
"Tuning the second harmonic generation of self-generated metallic islands,"
AIP Adv. **8**, 075012 (2018).

P5 A. Farag, M. Ubl, A. Konzelmann, M. Hentschel, and H. Giessen,
"Utilizing niobium plasmonic perfect absorbers for tunable near-

and mid-IR photodetection,"
Opt. Express **27**, 25012-25021 (2019).

P6 A. Konzelmann, M. Slota, B. Gompf, M. Dressel, and A. Berrier,
"Wavelength dependence of the second harmonic generation of percolating gold thin films,"
J. Appl. Phys. **127**, 163101 (2020).

CONFERENCE CONTRIBUTIONS

C1 A. Konzelmann, M. Fischer, and H. Giessen,
"Towards controlled interaction of Rydberg excitons in integrated and scalable solid state devices" (poster),
DFG Priority Programme SPP 1929: GiRyd Kickoff workshop, Heidelberg, Germany (2016).

C2 A. Konzelmann, M. Fischer, and H. Giessen,
"Giant excitonic Rydberg atoms in a solid: Potential for precision sensing and quantum effects" (poster),
SFB TRR 21: 10th international workshop about the control of quantum correlations in tailored matter, Loveno di Menaggio, Italy (2017).

C3 A. Konzelmann, M. Fischer, T. Davis and H. Giessen,
"Rydberg excitons in Cu_2O: Modifying the absoprtion spectrum by tuning the selection rules" (poster and talk),
GiRyd Status and PhD Workshop, Dresden, Germany (2017).

C4 A. Konzelmann and H. Giessen,
"Interaction of Rydberg excitons with higher orbital angular momentum light" (poster),
2nd international workshop on Rydberg excitons in semiconductors, Aarhus, Denmark (2018).

C5 A. Konzelmann and H. Giessen,
"Rydberg excitons in Cu_2O and their interaction with light" (poster),
SPP 1929: International workshop on giant interactions in Rydberg systems, Hamburg, Germany (2018).

C6 A. Konzelmann and H. Giessen,
"Rydberg excitons in Cu_2O: Tailoring of optical transitions" (poster),
SRitp and GiRyd School on Giant interactions in Rydberg systems, Rehovot, Israel (2018).

C7 A. Konzelmann and H. Giessen,
"Optical activation of dipole-forbidden exciton transitions in cuprous oxide (Cu_2O) using orbital angular momentum light" (poster),
DPG Spring Meeting, Rostock, Germany (2019).

C8 A. Konzelmann and H. Giessen,
"Breaking dipolar selection rules with Rydberg excitons" (talk),
GiRyd Status Workshop, Kaiserslautern, Germany (2019).

C9 A. Konzelmann and H. Giessen,
"Breaking dipolar selection rules with Rydberg excitons" (talk),
3rd international workshop on Rydberg excitons in semiconductors, Durham, England (2019).

C10 A. Konzelmann and H. Giessen,
"Breaking dipolar selection rules with Rydberg excitons in Cu_2O" (poster),
IQST Day, TA Esslingen, Germany (2019).

CONTENTS

1

INTRODUCTION AND MOTIVATION

Semiconductors have been of great research interest both in fundamental research and applied physics. An exciton is an elemental excitation in a semiconductor. It is a bound state of an electron and a hole. Excitons have been theoretically proposed by Frenkel and Wannier in the 1930's [1, 2] and experimentally found in cuprous oxide (Cu_2O) by Hayashi and Katsuki as well as Gross and Karryjew in the 1950's [3, 4]. Starting from the 1970's intensive research was performed on excitons in cuprous oxide by means of modulated exciton spectroscopy [5], forbidden resonant Raman scattering [6], and high-pressure X-ray studies [7, 8]. This way, the Cu_2O band structure was analyzed, and the effective electron and hole masses $m_e^* = (0.99 \pm 0.03)\, m_e$ and $m_h^* = (0.69 \pm 0.04)\, m_e$, the unit cell lattice constant $a = 4.26\,\text{Å}$, and the Bohr radius of the 1S yellow exciton $a_B = 7\,\text{Å}$ were determined [9].
Cuprous oxide has in total ten valence and four conduction bands with a direct bandgap $E_g = 2.17\,\text{eV}$. Since the highest conduction and the lowest valence band have the same (positive) parity, the dipole moment between them vanishes and the radiative lifetimes of excitons of the so called yellow series are relatively long. The oscillator strength of the yellow 2P-exciton is $2.8 \cdot 10^{-6}$, which is in good agreement with Eliott's theory of forbidden exciton transitions [10]. The exciton finestructure was not only investigated experimentally by, e.g., applying external fields [11] or in two-photon experiments [12], but also described theoretically [9, 13, 14]. Even- and odd-parity excitons were assigned up to $n = 7$ and it was found that the coupling of electron and hole to longitudinal optical phonons produces a frequency-dependent dielectric

function $\varepsilon\left(k,\omega\right)$, that the exciton fine structure is reproduced by central-cell corrections, and that the effective mass approximation is valid as long as excitons are sufficiently large.

Excitons in cuprous oxide are in many respects different from excitons in other semiconductors. In typical III-V compound semiconductors, such as GaAs, the Rydberg binding energy accounts for only a few meV ($Ry_{\text{GaAs}} = 4.2\,\text{meV}$). Therefore, the energy spacing of higher exciton states is beyond the resolution of conventional spectrometers and the quality of suitable light sources is insufficient to avoid accidental excitation across the band gap into the ionization continuum. In other words, the exciton series is energetically located too closely to the band gap, where free electron-hole pairs are created instead. Its unique bandstructure makes the semiconductor cuprite in this aspect perfectly suited for the formation of excitons with a large Rydberg binding energy of 96 meV. Here, higher-n exciton states are energetically not spaced too closely to each other nor to the ionization continuum. The $1/n^2$-dependency of the binding energy of the exciton series impressively emphasizes the quantum mechanical analogy between excitons and the hydrogen atom. Furthermore, the excitation energy of excitons in Cu_2O lies in the visible light range, which is convenient for investigation and application.

In 2014, the excitation of P-exciton states up to principal quantum number $n = 25$ was achieved [15], which attracted renewed interest in this field of research. The term *Rydberg exciton* was established in analogy to the Rydberg state of atoms. These highly-excited Rydberg excitons have large spatial extensions similar to Rydberg atoms. Rydberg atoms posses a highly-excited valence electron, which gives them properties very much different from ground state atoms. Their giant size makes them highly sensitive to nearby charges or atoms. Rydberg atoms function as important measuring devices and building blocks for quantum physics, such

as optical sensors [16], gas detectors [17], ion microscopes [18], or single-photon sources [19]. Rydberg atoms can also be engaged as building blocks for quantum computers.
In contrast to Rydberg atoms, Rydberg excitons are embedded in a semiconductor and can be moved in the crystal using high-precision, microscopic energy potential landscapes [15, 20]. Their discovery enables access to the first Rydberg system in a solid. In cuprous oxide, the Bohr radii for principal quantum numbers around $n = 20$ amount to values in the µm-range. Dealing with such a macroscopic quantum object is advantageous for the realization of integrated and scalable solid state quantum devices.

In the last couple of years intensive research has been conducted in order to show similarities and differences between Rydberg excitons and Rydberg atoms. Both in Rydberg atoms and Rydberg excitons the Rydberg blockade exists. The excitation of a Rydberg exciton leads to a detuning and, thus, prevents the simultaneous excitation of other Rydberg excitons within a defined volume [15]. Due to the large volume in cuprous oxide, the Rydberg blockade is very dominant and could be used for optical switching. The concept of quantum defect, $E_B = -Ry/\left(n - \delta_l\right)^2$, has proven to be extremely successful in the description of highly excited Rydberg excitons [21]. The exciton concept translates the bound states of an electron-hole pair onto a hydrogen-like series, where the crystal environment is included in the effective masses and the dielectic function of the material [22, 23]. Higher angular momentum excitons have been observed in cuprous oxide by introducing an additional symmetry breaking through external fields [24–26], and quantum-coherent effects among Rydberg excitons have been studied [27]. The bosonic character of the exciton quasiparticle together with high resolution spectroscopy, praises Cu_2O as the most favorable 3D system to search for the quantum statistical phenomenon of Bose-Einstein condensation of yellow 1S-excitons due to their long lifetimes [28].

Much theoretical work was done on the electro- and magneto-optical properties of Rydberg excitons [29–31]. Focus was also laid on solid-state specific effects, like phonon-assisted absorption [32] and the electron-hole plasma [33, 34]. Two-photon absorption and second-harmonic generation were used to probe the dipole-forbidden, even-parity excitons up $n = 12$ [35–38] and detailed theoretical calculations were performed [39, 40]. Rydberg excitons trapped in potential wells [41–43] and in microcrystals [44] were studied. Lately, the research on Rydberg excitons in cuprous oxide has been extended to excitation by orbital angular momentum light [45], and, charge-impurities [46, 47] have been found to be the limiting factor for the existence of high principal quantum number excitons with $n \geq 25$. Very recently, Rydberg exciton-polaritons in a Cu_2O microcavity were investigated [48].

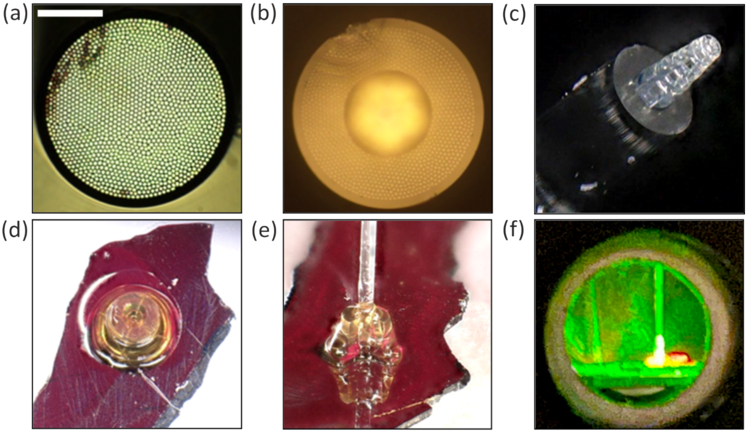

Figure 1.1. (a) End facet of a multicore fiber. Scale bar equals 50 µm. (b) 2D view and (c) 3D view of multicore fiber with 3D printed optical element. (d) Fiber chuck (500 µm diameter) printed onto a cuprite crystal flake. (e) Multicore fiber with optical element inserted into fiber chuck on cuprite crystal flake. (f) Multimode fiber with 3D printed lens attached to a fiber chuck on a cuprite crystal flake inserted into the cryostat. Laser light is sent through the fiber. Reflection signal is collected through the same fiber. Cryostat window diameter equals 10 mm.

The key prerequisite for all above mentioned fundamental studies is the availability of high-quality cuprous oxide crystals. For more integrated applications these crystals, bearing Rydberg excitons, can be combined with nanophotonic components, such as high-quality, 3D-printed micro-optics. In combination with a multicore fiber and pump-probe spectroscopy, this would yield an angle-resolved scanner scheme capable of addressing different spatially neighboring Rydberg excitons. This vision of ours is shown in Fig. 1.1, where we aim at establishing an integrated and scalable quantum system to let two or more neighboring Rydberg excitons interact.

The thesis is outlined as follows. Chapter 2 starts with an introduction to the theory of Rydberg atoms. Their history, properties, and applications are described. Next, the semiconductor cuprous oxide is introduced and a detailed description of the peculiarities of Rydberg excitons in cuprous oxide is given. Exciton binding energy, wave function and lineshapes, as well as exciton symmetry representations are discussed. The interaction of light with matter is discussed in terms of Maxwell's equations for linear optics, nonlinear optics, as well as with a focus on light–exciton interaction. Orbital angular momentum light is characterized mathematically and its creation is explained. The importance of its field gradient with respect to multipolar transitions is demonstrated. Finally, the theory of plasmonic nanostructures is introduced.

The experimental setup is outlined in Chapter 3. It includes low-temperature technique and pump-probe spectroscopy in combination with lock-in detection. Laser sources as well as technical connections are introduced, and the complete laser setups are described. In addition, design and fabrication of sample components, such as plasmonic nanostructures, quantum wells, and 3D-printed micro-optics are explained. Chapter 4 is dedicated to cuprous oxide crystal preparation. The techniques of crystal orientation, slicing, polishing, structuring and mounting are introduced. A complete sample overview is given.

In Chapter 5 we present in a detailed theoretical study the modified selection rules of Rydberg excitons in cuprous oxide when being excited with orbital angular momentum light. We also show the results of corresponding experiments. In Chapter 6 we examine the enhancement of quadrupole transitions in cuprous oxide excitons using plasmonic antennas. Different spectroscopy methods are applied, while the influence of pump-probe spectroscopy on the creation of Rydberg excitons in cuprous oxide is studied. In Chapter 7 we theoretically investigate Rydberg excitons in quantum wells. A detailed German summary is given in the appendix.

2

THEORETICAL BACKGROUND

In this chapter the theoretical background relevant for this thesis is introduced. This includes the theory of Rydberg atoms in Section 2.1 as well as Rydberg excitons in cuprous oxide in Section 2.2. As the experimental approach in this work is optical spectroscopy, the interaction of light with matter will be discussed in Section 2.3. In Section 2.4 the focus is laid on orbital angular momentum light, while Section 2.5 discusses the basic properties of plasmonic nanostructures.

2.1 RYDBERG ATOMS

2.1.1 *History*

The spectral lines of hydrogen were identified by Anders Jonas Ångström in 1862 [49] and described with an empirical formula by Johann Jacob Balmer in 1884 [50]. A more general theoretical description was given by Johannes Robert Rydberg in 1890 for spectral lines emitted by any atoms that have a single valence electron [51]. In 1913 Niels Bohr postulated his quantum model of the atom [52] in accordance with Rydberg's formula,

$$E_n = \frac{-R_H}{n^2}, \tag{2.1}$$

with E_n being the energy of the quantum state, R_H the Rydberg constant for hydrogen, and n the principal quantum number. Rydberg's formula describes in principle any system, where the atom's valence electron is far from the positively charged nucleus, referred to as in a *Rydberg state*, resulting in a specifically ordered energy level series.

Rydberg states can be observed in high-energy environments such as interstellar media in space [53]. The advent of new laser technologies, i.e., the tunable dye laser in the 1970's [54], allowed for the realization of controllable excitation of selected Rydberg states in laboratories [55]. Later, the method of laser cooling and trapping in 1998 [56–58] led to a new level of precision.

2.1.2 *Basic properties*

The basic properties of Rydberg atoms are thoroughly treated in different reviews [59, 60] and will only be shortly summarized here. Rydberg atoms are atoms in a highly-excited state, where the valence electron is, on average, far from the nucleus. They can be described by the same physics as of highly-excited hydrogen atoms, with energy levels given by the Rydberg formula. Rydberg atoms are weakly bound states with large polarizabilities and large extensions, and may be created with high energies close to the ionization energy. Thus, they interact strongly with their environment, i.e., with macroscopic external electric fields, but also with fields induced by other nearby (Rydberg) atoms or molecules. The lifetime of Rydberg atoms reaches hundreds of microseconds, resulting in narrow spectral lines for transitions between Rydberg atoms as well as longer interaction times. The characteristic scalings are summarized in Table 2.1. Rydberg atoms combine the control of both single atoms and single photons. They feature a lot of exaggerated properties, which allow for many practical applications.

Property	Scaling
Binding energy	n^{-2}
Orbital radius	n^2
Dipole moment	n^2
Polarizability	n^7
Radiative lifetime	n^3

TABLE 2.1. Scaling properties of Rydberg atoms [55]. n is the principal quantum number.

2.1.3 *Applications*

Rydberg atoms are ideal for sensing electromagnetic fields in the microwave and terahertz frequency range [16, 61]. Atoms are the same everywhere, with constant properties over time, which makes them a perfect candidate as measurement device. Rydberg atoms can measure in real time and are capable of detecting a single photon without absorbing it [62]. Sensing microwave and terahertz frequency radiation is important for a wide range of applications, such as WiFi, Bluetooth, mobile phone networks, communication in aerospace industry, self-driving cars, and security scanners in airports. Rydberg atoms can function as gas sensors [17] or as an ion microscope [18].

A central aspect of many applications is the Rydberg blockade [63–65]. A single photon that excites an atom into a Rydberg state will interact and significantly shift the Rydberg energy levels of all nearby atoms, and, thus suppress a simultaneous excitation of several atoms into Rydberg states and block the transmission of other incoming photons within a defined blockade volume. After the first experimental observations in 2004 [66, 67], the Rydberg blockade has been used for the generation of non-classical photonic states. This way, Rydberg atoms are capable of creating a medium that is nonlinear at the level of two photons, opening the field of

Rydberg-based quantum optics [19, 68–72].
Furthermore, Rydberg atoms can be used for quantum state engineering [73] and can function as platform for quantum simulations [64, 74–80]. Rydberg atoms realize a two-level system, which is needed for quantum metrology and the processing of quantum information [74, 81, 82]. Having ground state atoms on optically resolvable distances being manipulated by strongly focused optical fields, allows for the storage of large data as well as the handling of complex algorithms required for quantum simulators. Replacing ground state atoms by Rydberg atoms brings new opportunities, like strong interactions on up to distance scales on the order of 10 µm, as well as new dynamics, like the Rydberg blockade effect.

2.2 RYDBERG EXCITONS IN CUPROUS OXIDE

A Rydberg exciton is an exciton that is in a state with large principal quantum number n. Similar to Rydberg atoms, Rydberg excitons have properties that are very different from their ground-state counterpart. In contrast to Rydberg atoms, they are already embedded in a semiconductor, making them the first Rydberg system in a solid. As cuprous oxide is a covalent crystal, the electron-hole pair is loosely bound, spreading over 10 billion crystal unit cells. The exciton radii are large, with a modified Bohr radius,

$$a_B^* = 1.11\,\mathrm{nm}, \tag{2.2}$$

making Rydberg excitons in cuprous oxide mesoscopic quantum objects.

Rydberg excitons are quasiparticles with effective masses m^* and within a crystal environment ε. Cuprous oxide has a complex band structure and features interaction with phonons as well as surface charges. This results in different scalings of binding energy and size as well as the reaction to external fields. As the permittivity is isotropic in cuprous oxide due to its cubic symmetry, the exciton spectrum looks like a scaled Rydberg series as for hydrogen. However, there are small deviations from the ideal series [22, 23]. Atoms are isotropic with respect to rotation, so the angular momentum is conserved. The band dispersion of cuprous oxide is not ideally parabolic and the interaction potential between electron and hole is not purely Coulombic. These deviations, also known as central-cell corrections [9], cause a mixing of angular momentum states in the crystal. The permittivity becomes frequency- and wavevector-dependent (but, $\varepsilon\left(k,\omega\right)\approx$ const. for large Bohr radii) and exchange interactions appear. These deviations can be corrected for through the quantum defect δ_l in the exciton binding energy:

$$E_B^* = -\frac{Ry^*}{\left(n-\delta_l\right)^2}. \tag{2.3}$$

The modified scaling properties with respect to Rydberg atoms, bring some advantages. The whole Rydberg exciton series can be scanned by one single laser, which is not possible for Rydberg atoms. The high-field regime,

$$\hbar\omega_c = \frac{\hbar e B}{m_e} \approx \mathrm{meV}\cdot B\,(\mathrm{T}) >> Ry, \tag{2.4}$$

with reduced Plack constant $\hbar$, electron charge e and mass m_e, magnetic field B, and Rydberg constant Ry, is easily accessible when replacing the Rydberg constant Ry by the modified Rydberg constant Ry^*. 1 T magnetic field in cuprite corresponds to comparable effects with 390 T in hydrogen, which makes Rydberg excitons handier for research in the laboratory or for applications.

As for Rydberg atoms, there exists a Rydberg blockade also for Rydberg excitons. The injection of an exciton blocks further exciton creation in its surrounding. For Rydberg excitons, the blockade radius reaches up to 10 μm. In contrast to Rydberg atoms, highly excited excitons with µm-size extensions can be placed and moved in a crystal with high precision using macroscopic energy potential landscapes. And, similar to Rydberg atoms, they are capable of sensing elementary excitations in their surrounding on a quantum level. This means, that Rydberg excitons in Cu_2O are, as a solid-state analog of Rydberg atoms, of great research interest as they make a well-controllable, macroscopic quantum system.

Excitonic effects are decisive for the optical properties of semiconductors. Usually, in semiconductors the crystal lattice induces phonons. In typical III-V compound semiconductors, such as GaAs, optical phonons are dipole-active. Due to the s- and p-type valence and conduction bands, the total angular momentum is a good quantum number, the ground state excitons are dark states and the first excited S-exciton states are bright states. This, and the existence of phonon decay paths, hinders having a Rydberg series. Due to phonon scattering, the excitons have small lifetimes and are spectrally broad. Due to a small Rydberg energy ($Ry_{\mathrm{GaAs}} = 4.2\,\mathrm{meV}$), the states are not only very close to each other or even overlap, having an energy difference between two adjacent states $\Delta E = 50 - 300\,\mathrm{meV}$, but are also very close to the bandgap. Furthermore, the spatial extension of the excitons is small.

Regarding the formation of (Rydberg) excitons, cuprous oxide is of unique crystal quality. In cuprous oxide, the valence band is formed by d-bonding orbitals and the conduction band is formed by s-antibonding orbitals. This way, angular momentum is no good quantum number. The first-excited S-exciton states are dark, as band-to-band transitions are dipole forbidden. This results in special selection rules. For one-photon excitations, the allowed optical transitions are P-excitons, starting at $n = 2$, with much longer lifetimes τ compared to other semiconductors ($\tau \approx ns$) and with very narrow linewidths going down to below $10\,\mu\mathrm{eV}$ for $n = 25$

due to vanishing decay paths. While the ground state is no exciton state, there exists a slightly allowed, very narrow 1S-exciton state, which interacts with the continuous, square-root dependent, phonon background. This results in a Fano-type shape of the P-excitons. With a factor ten larger Rydberg energy than in other semiconductors, $Ry^* = 96\,\mathrm{meV}$, the energy spectrum of the exciton series is not spaced too closely to each other ($\Delta E \approx 12\,\mathrm{meV}$) nor to the ionization continuum, and can still be addressed with a single laser, covering a wavelength range of only 7 nm.

The absorption spectrum of cuprous oxide in one-photon excitation is shown in Fig. 2.1 [83]. It features many distinct peaks below the bandgap, which belong to the complete yellow nP Rydberg exciton series, including the 1S-orthoexciton. It shows the onset of the interactions between the yellow (S_y) and green (S_g) 1S-excitons with the Γ_3^-- and Γ_4^--phonons as square-root shaped background, as well as the appearance of F-excitons starting from $n = 4$. The nominal bandgap E_g and the end of the exciton series $\tilde{E}_g$ are indicated. The exciton series is limited to $n \approx 25$ due to residual charge impurities in the crystal, which build up an electric field that causes ionization of highly excited excitons [47]. The nP-exciton energies are listed in Table 2.2 [15].

Natural cuprite ocurrs in different mines across the world. While only microscopic crystals are found in the USA (Arizona, New Mexico, Colorado, Utah), Latin America (Mexico, Bolivia, Chile), Europe (France, England), and Russia, very pure, up to 15 cm large crystals come from the Onganja and Tsumeb mines in Namibia [84, 85]. The latter ones are also the purest crystals with respect to exciton formation. Cuprite is said to be one of the rarest of all gems. It can also be grown artificially. This, however yields not yet as pure crystals as can be found in nature [44, 86, 87]. Samples of natural and artifical cuprite crystals are shown in Fig. 2.2.

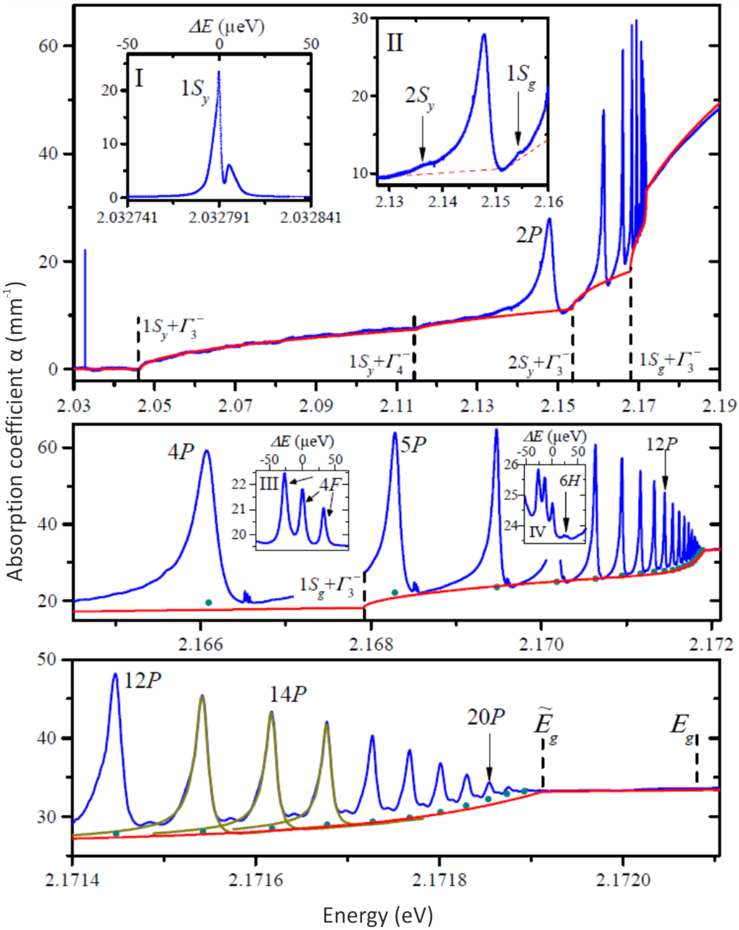

FIGURE 2.1. High-resolution absorption spectrum of the yellow exciton series measured with a probe power of 1 W at 1.35 K [83]. Red line indicates background absorption, dashed vertical lines mark the beginning of a phonon branch. $\tilde{E}_g$ indicates the end of the exciton series and the transition into the continuum at about 172 μeV below the nominal band gap $E_g = 2.172$ eV. Insets show zooms into regions of S-, F-, and H-excitons.

TABLE 2.2. nP-exciton energies E_n of the yellow Rydberg series in cuprous oxide for principal quantum numbers $n = 2 - 25$ [15].

n	E_n (eV)
2	2.1484
3	2.16135
4	2.16609
5	2.16829
6	2.16948
7	2.170182
8	2.170635
9	2.170944
10	2.171163
11	2.171342
12	2.171446
13	2.171541
14	2.1716159
15	2.1716758
16	2.1717248
17	2.1717653
18	2.1717989
19	2.171827
20	2.1718515
21	2.1718724
22	2.1718906
23	2.1719068
24	2.1719202
25	2.1719335

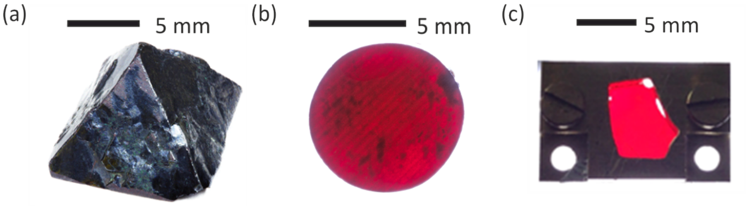

FIGURE 2.2. (a) Natural cuprite crystal. Bottom side length equals 10 mm. (b) Polished, artificial cuprite crystal slice. Diameter is 8 mm. Dark spots are impurities. (c) Natural cuprite crystal slice polished and mounted strainfree to a sample holder with dimensions 10 mm × 15 mm.

2.2.1 *Cuprous oxide crystal structure*

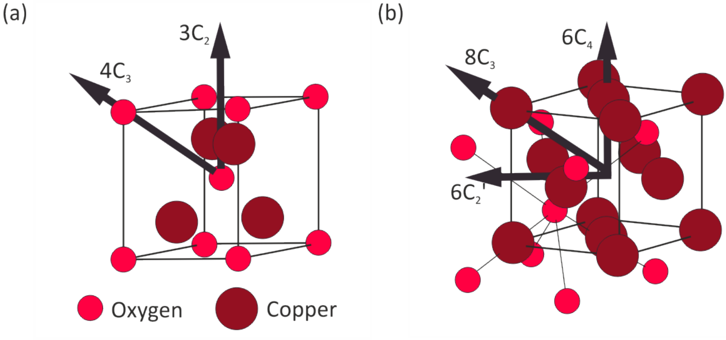

FIGURE 2.3. Cuprous oxide crystal lattice. Oxygen atoms form a bcc lattice (a), while copper atoms form a fcc lattice (b). The rotational operations XC_y of the crystallographic groups T and O fit to the positions of the oxygen and copper atoms respectively. The number of similar operations X is written in front of the rotation symbol C. The subscript label y indicates that a rotation is y-fold. Crystal structures have been reproduced with help of VESTA software.

Cuprous oxide crystallizes in a cubic lattice [8]. The oxygen atoms form a body-centered cubic (bcc) lattice while the copper atoms form a face-centered cubic (fcc) lattice shifted by a quarter of space diagonal from the oxygen atoms. The lattice constant is $a = 4.27\,\text{Å}$. The unit cell contains two oxygen and four copper atoms. Cuprous oxide has a hardness of 3.5 to 4 on Mohs scale and a density or specific gravity of 6.14, meaning that 1 cubic centimeter of cuprous oxide weighs 6.14 times as much as one cubic centimeter of water at 4 °C [84]. Cuprous oxide is composed of 88.8 wt% copper and 11.2 wt% oxygen [85]. The symmetry of cuprous oxide is described by point group O_h, which is of order 48 and contains all operations that transform a cube into itself [88]. The 24 proper rotations are divided into five classes (see also Fig. 2.3):

- E: identity
- $8C_3$: rotations of $2\pi/3$ about the eight threefold space diagonal axes $\langle 111\rangle$, $\langle\bar{1}\bar{1}\bar{1}\rangle$, $\langle 11\bar{1}\rangle$, $\langle\bar{1}\bar{1}1\rangle$, $\langle 1\bar{1}1\rangle$, $\langle\bar{1}1\bar{1}\rangle$, $\langle\bar{1}11\rangle$, $\langle 1\bar{1}\bar{1}\rangle$
- $3C_2$: rotations of π about the three cubic coordinate axes $\langle 100\rangle$, $\langle 010\rangle$, $\langle 001\rangle$
- $6C_4$: rotations of $\pi/2$ about the cubic coordinate axes $\langle 100\rangle$, $\langle\bar{1}00\rangle$, $\langle 010\rangle$, $\langle 0\bar{1}0\rangle$, $\langle 001\rangle$, $\langle 00\bar{1}\rangle$
- $6C_2'$: rotations of π about the six twofold face diagonal axes $\langle 110\rangle$, $\langle 1\bar{1}0\rangle$, $\langle 101\rangle$, $\langle 10\bar{1}\rangle$, $\langle 011\rangle$, $\langle 01\bar{1}\rangle$

The 24 improper rotations are in the classes:

- I: inversion
- $8S_6$: rotations through $\pi/3$ about the eight space diagonal axes followed by a reflection in the plane perpendicular to the axis of rotation
- $3\sigma_h$: reflection in a plane perpendicular to the principal axis of symmetry, i.e., xy-plane (ts0), xz-plane (t0r), yz-plane (0sr)

- $6S_4$: rotations through $\pi/2$ about the six coordinate axes followed by a reflection in the plane perpendicular to the axis of rotation
- $6\sigma_d$: reflection containing a principal axis of symmetry that bisects the angle between two twofold rotation axes perpendicular to the principal axis, i.e., ±45° to xy-, xz-, and yz-plane, (tvv), (tv-v), (usu), (us-u), (wwr), (w-wr)

As the symmetry group O_h contains inversion symmetry, parity is a good quantum number. This means that the electronic, excitonic and phononic states contain a defined parity, so the parity selection rules must be fulfilled during optical transitions.

2.2.2 *Cuprous oxide band structure and selection rules*

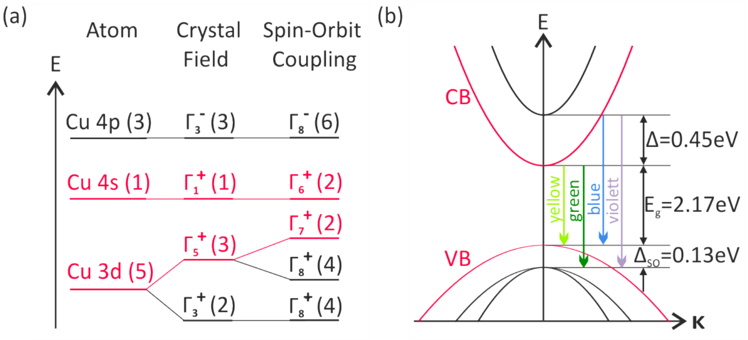

FIGURE 2.4. (a) Electronic band structure of cuprous oxide. (b) Schematic drawing of the dispersion relation at the Γ-point. Energy gap E_g, as well as crystal field Δ and spin-orbit Δ_{SO} splittings are indicated.

The energy bands in semiconductors are formed by 10^{20} atomic orbitals. Energy bands evolve when considering quasi-free electrons with parabolic dispersion of free electrons $E(\boldsymbol{r}) = \hbar^2 k^2/(2m_e^*)$ plus a weak periodic potential $V(\boldsymbol{r}) = V(\boldsymbol{r}+\boldsymbol{R})$. $\hbar$ is the reduced

Planck constant, k the absolute value of the wavevector, m_e^* the modified electron mass, $\boldsymbol{r}$ the position vector, and $\boldsymbol{R}$ the displacement. For a semiconductor the Fermi energy lies within the forbidden band gap. For a direct semiconductor the global valence band maximum and conduction band minimum occur at the same point in k-space. If an electron is excited from the valence to the conduction band, it leaves a hole. This latter quasiparticle carries opposite momentum, spin and charge compared to the electron, and an effective mass m_h^*. Together with the electron, it can form another quasiparticle, the exciton. Repulsive Coulomb forces from other electrons in the semiconductor prevent immediate attraction of electron and hole, resulting in a balanced bound state, with slightly less energy than the unbound electron and hole.

Cuprous oxide is a semiconductor with a direct bandgap at the Γ-point. In this thesis we investigate Rydberg excitons of the yellow series in cuprous oxide, i.e., the states formed by holes from the highest valence and electrons from the lowest conduction band. The highest valence band in cuprous oxide stems from the fivefold degenerate 3d copper orbital, while the lowest conduction band stems from the 4s copper orbital (see Fig. 2.4) [89–91]. Under the influence of the crystal field, the 3d copper orbital splits into a threefold degenerate band with symmetry Γ_5^+ and a lower-lying twofold degenerate band with symmetry Γ_3^+. More details on the symmetry representations will be given in Section 2.2.5. Spin-orbit coupling between the quasispin I and the hole spin S_h causes further splitting of the Γ_5^+ valence band by an amount of $\Delta_{SO} = 130\,\mathrm{meV}$ into a higher-lying twofold degenerate band of symmetry Γ_7^+ and a lower-lying degenerate band of symmetry Γ_8^+ [25]. Including spin, the Γ_1^+ conduction band from the 4s copper orbital becomes twofold degenerate and is described by symmetry Γ_6^+. As a result, the bands of interest, i.e, the highest valence band and the lowest conduction band for the yellow exciton series, have symmetries Γ_7^+ and Γ_6^+, respectively.

The difference in total angular momentum between the two bands is $\Delta j = 2$, so the transition dipole moment for band-to-band transitions vanishes, as it requires $\Delta j = \pm 1$. However, when exciting an exciton, not only the band symmetries (Δl_{ext}) but also the exciton envelope symmetry (Δl_{int}) is decisive for the selection rules, which read:

$$\Delta j = \Delta l_{\text{ext}} \pm \Delta l_{\text{int}} = \pm 1. \tag{2.5}$$

For first-class transitions, i.e., excitation of S-excitons, the envelope function carries no angular momentum ($\Delta l_{\text{int}} = 0$), thus, S-excitons are dipole forbidden between s- and d-type conduction and valence bands, with

$$\Delta j_{1^{\text{st}}\,\text{class}} = \Delta l_{\text{ext}} \pm \Delta l_{\text{int}} = 2 \pm 0 = 2. \tag{2.6}$$

However, so-called second-class transitions are possible. This means, that the yellow P-excitons with an additional envelope angular momentum $\Delta l_{\text{int}} = 1$ can be excited with dipolar light:

$$\Delta j_{2^{\text{nd}}\,\text{class}} = \Delta l_{\text{ext}} - \Delta l_{\text{int}} = 2 - 1 = 1. \tag{2.7}$$

However, the transition dipole moment of a second-class transition is typically one order of magnitude smaller than for a first-class transition, i.e., S-excitons in semiconductors with s- and p-type bands.

2.2.3 *Exciton binding energies, radii, and wave function*

An exciton can be described as an electron of charge $-e$ and mass m_e orbiting at a radius r around the hole with positive charge $+e$. This way, it obeys Newton's law for uniform circular motion:

$$\frac{m_e v^2}{r} = \frac{1}{4\pi\varepsilon_0}\frac{e^2}{r^2}. \tag{2.8}$$

Considering the quantization of angular momentum according to Bohr,

$$m_e v r = n\hbar, \tag{2.9}$$

and combining Eq. (2.8) with Eq. (2.9), yields for the radius r:

$$r = \frac{4\pi\varepsilon_0 n^2\hbar^2}{e^2 m_e}. \tag{2.10}$$

The exciton binding energy is the sum of its kinetic and potential energies:

$$E_B = \frac{m_e v^2}{2} - \frac{1}{4\pi\varepsilon_0}\frac{e^2}{r} = -\frac{e^4 m_e}{32\pi^2\varepsilon_0^2 n^2\hbar^2} = -\frac{Ry}{n^2}, \tag{2.11}$$

with the Rydberg constant

$$Ry = \frac{e^4 m_e}{32\pi^2\varepsilon_0^2\hbar^2} = \frac{\hbar^2}{2m_e a_B^2} = 13.6\,\mathrm{eV}, \tag{2.12}$$

and the Bohr radius

$$a_B = \frac{4\pi\varepsilon_0\hbar^2}{m_e e^2}. \tag{2.13}$$

Note, the exciton binding energy E_B is negative, meaning the electron is bound to the hole, and the binding energy decreases as $1/n^2$, leading to an energy level series as for hydrogen, located slightly below the bandgap energy (see Fig. 2.5 (a)). Nevertheless, the exciton energy series in cuprous oxide deviates from the ideal hydrogen-like series due to the nonparabolicity of the band dispersion [22]. This phenomenon is equivalent to a rescaled Coulomb interaction, as for Rydberg atoms, due to the influence of the ionic core. It can be corrected for by introducing a quantum defect δ_l. Eq. (2.11) then becomes:

$$E_B^* = -\frac{Ry^*}{(n-\delta_l)^2}. \tag{2.14}$$

$Ry^* = \varepsilon^{-2} m^*/m_e Ry$ is the modified Rydberg constant, ε the permittivity in cuprous oxide, and $m^* = m_e^* m_h^* / \left(m_e^* + m_h^*\right)$ the effective exciton mass with m_e^* and m_h^* being the electron and hole masses respectively.

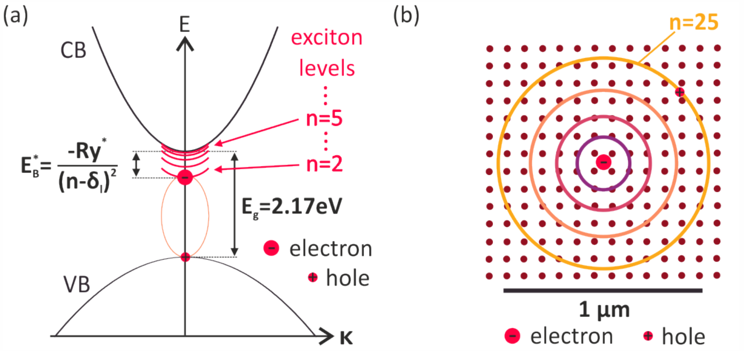

Figure 2.5. (a) Schematic drawing of the dispersion relation of cuprous oxide at the Γ-point together with exciton levels. (b) Schematic drawing of exciton radii in cuprous oxide.

When determining the modified Bohr radius a_B^* from Eq. (2.13) it remains difficult to use the right value for the frequency-dependent permittivity ε. Therefore, it is more convenient to determine a_B^* from Eq. (2.12) with experimental values for Ry^* and m^*. Using

$Ry^* = 96\,\text{meV}$ and $m^* = 0.4m_e$ ($m_e^* = 0.99m_e$, $m_h^* = 0.69m_e$) [9], yields the modified Bohr radius:

$$a_B^* = 1.11\,\text{nm}. \tag{2.15}$$

The exciton radius is given by the expectation value $\langle r \rangle$ for the distance between electron and hole [55]:

$$\begin{aligned}\langle r \rangle &= \int_{\vartheta=0}^{\pi} \int_{\varphi=0}^{2\pi} \int_{r=0}^{\infty} \Psi_{n,l,m}^{*}\left(r, \vartheta, \varphi\right) r \Psi_{n,l,m}\left(r, \vartheta, \varphi\right) r^2 dr \sin\vartheta d\vartheta d\varphi \\ &= \frac{a_B^*}{2}\left(3n^2 - l\left(l+1\right)\right).\end{aligned} \tag{2.16}$$

The resulting exciton radii $\langle r \rangle$ are listed in Table 2.3 for P-excitons ($l = 1$) in selected principal quantum number states $n \in \{2 \ldots 25\}$. Due to the large exciton extension over up to ten billion lattice sites (see schematic drawing in Fig. 2.5 (b)), tiniest impurities can influence the formation of Rydberg excitons.

TABLE 2.3. Exciton radii $\langle r \rangle$ for P-excitons ($l = 1$) in selected principal quantum number states n.

n	2	5	10	15	20	25
$\langle r \rangle$ (nm)	5.55	40.5	165.4	373.5	664.9	1040

The wave function $\Psi_{\boldsymbol{k}}(\boldsymbol{r})$ of an electron in a periodic potential of a crystal is the product of a plane wave $e^{i\boldsymbol{k}\boldsymbol{r}}$ and a lattice periodic function $u_{\boldsymbol{k}}(\boldsymbol{r})$:

$$\Psi_{\boldsymbol{k}}(\boldsymbol{r}) = u_{\boldsymbol{k}}(\boldsymbol{r}) \cdot e^{i\boldsymbol{k}\boldsymbol{r}}. \tag{2.17}$$

The derivation of the exciton wave function can be done analogously to the wave function for the electron, yielding a problem similar to the hydrogen atom. It can be solved by separation Ansatz into relative and center-of-mass coordinates. The resulting exciton wave function reads [92, 93]:

$$\Phi_{K,n,l,m}\left(\boldsymbol{R},\boldsymbol{r_e},\boldsymbol{r_h}\right) \approx e^{i\boldsymbol{KR}} u_0^c\left(\boldsymbol{r_e}\right) u_0^v\left(\boldsymbol{r_h}\right) \Psi_{n,l,m}\left(\boldsymbol{r}\right), \tag{2.18}$$

with the center-of-mass wavevector $\boldsymbol{K} = \boldsymbol{k_e} + \boldsymbol{k_h}$, the center-of-mass spatial coordinate $\boldsymbol{R} = \left(\boldsymbol{r_e} m_e^* + \boldsymbol{r_h} m_h^*\right) / \left(m_e^* + m_h^*\right)$, the relative spatial coordinate $\boldsymbol{r} = \boldsymbol{r_e} - \boldsymbol{r_h}$, and the electron and hole lattice periodic functions u_0^c and u_0^v, respectively. The envelope functions $\Psi_{n,l,m}\left(\boldsymbol{r}\right)$ are identical with the ones for the hydrogen atom. From here, the exciton radial wave function $R_{\mathrm{Cu_2O}}$ can be separated:

$$\begin{aligned} R_{\mathrm{Cu_2O}} =& \frac{2}{n^2}\sqrt{\frac{\left(n-l-1\right)!}{\left(n+l\right)!^3}} e^{-\frac{\alpha_{\mathrm{Cu_2O}} r}{2}} \left(\alpha_{\mathrm{Cu_2O}} r\right)^l \left(-1\right)^{2l+1} \left(\frac{1}{\alpha_{\mathrm{Cu_2O}}}\right)^{2l-1} \\ & \frac{\partial^{2l+1}}{\partial r^{2l+1}} \left(e^{\alpha_{\mathrm{Cu_2O}} r} \left(\frac{1}{\alpha_{\mathrm{Cu_2O}}}\right)^{n+l} \frac{\partial^{n+l}}{\partial r^{n+l}} \left(e^{-\alpha_{\mathrm{Cu_2O}} r} \left(\alpha_{\mathrm{Cu_2O}} r\right)^{n+l}\right)\right). \end{aligned} \tag{2.19}$$

n is the principal quantum number, l the orbital angular momentum quantum number, $\alpha_{\mathrm{Cu_2O}} = 2m^*/\left(n\varepsilon m_e a_0\right)$ the cuprous oxide fine structure constant, and a_0 the Bohr radius. The radial wave functions of Rydberg S-excitons ($l = 0$) in cuprous oxide are shown as $r^2 R^2_{\mathrm{Cu_2O}}\left(r\right)$ in Fig. 2.6 for principal quantum number states $n = 5 - 10$.

From the exciton wave function, one obtains an infinite number of bound states with eigenenergies E_n, being the sum of band gap energy E_g, binding energy E_B^*, and kinetic energy E_{kin}:

$$E_n = E_g + E_B^* + E_{\mathrm{kin}} = E_g - \frac{Ry^*}{\left(n-\delta_l\right)^2} + \frac{\hbar^2 \boldsymbol{K}^2}{2M}. \tag{2.20}$$

The exciton kinetic energy, however, is negligible, as $\boldsymbol{K} \approx 0$. Hereby, the terminology from atomic physics and quantum mechanics have been taken. A difference, however, is the choice of zero energy: while for the H-atom one chooses the ionization limit, for excitons one chooses the ground state of the crystal where no electrons or holes are excited. Therefore the exciton energies lie below the band gap (see Fig. 2.5 (a)).

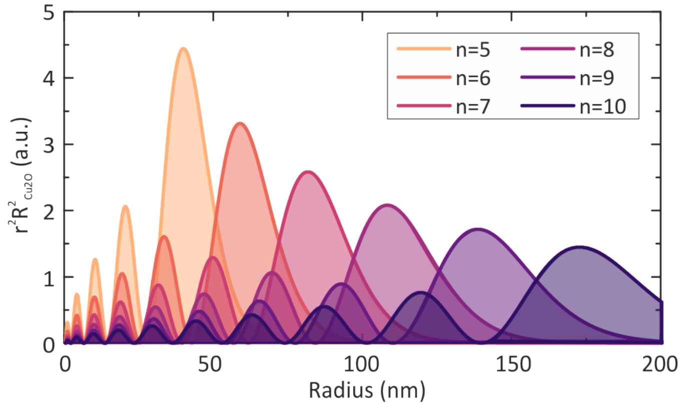

FIGURE 2.6. Cuprous oxide Rydberg S-exciton radial wave function $r^2 R^2_{\mathrm{Cu_2O}}$ for different principal quantum number states $n = 5 - 10$.

2.2.4 *Phonons and exciton lineshapes*

The unit cell in cuprous oxide contains six atoms, so there exist among the three acoustic, $3 \cdot (N - 1) = 15$ optical phonon branches [94]. The amount of optical phonons at the Γ-point is, however, reduced to eight due to degeneracy. Phonons can be probed using inelastic neutron scattering [95]. Optical phonons can also be probed using Raman spectroscopy [96, 97], and their contribution can be seen in absorption spectroscopy [98]. Toyozawa suggested that the large linewidth of the P-excitons is due to phonon scattering [99] and that the strong asymmetry of the lines could be explained by a general theory of phonon-assisted absorption, which take the continuum of the yellow 1S state into account [100]. From luminescence spectroscopy it is known that the Γ_3^- optical phonon with an energy of $\hbar\omega_{3-} = 13.6\,\mathrm{meV}$ at the zone center is the dominant phonon branch, followed by the Γ_4^- optical phonon at $\hbar\omega_{4-} = 82.1\,\mathrm{meV}$ [32, 101]. The phonon background in cuprous oxide is very strong, even at cryogenic temperatures (see Fig. 2.7). The phonon background shown in Fig. 2.7 (a) is due to the coupling of the *green* 1S-exciton ($E_{1S_g} = 2.154\,\mathrm{eV}$) with the Γ_3^- phonon ($E_{\Gamma_3^-} = 0.014\,\mathrm{eV}$). As this continuous background follows a square-root dependence,

$$E_{1S-ph} \propto \sqrt{E - \left(E_{1S} + E_{ph}\right)}, \tag{2.21}$$

the exciton resonances experience an offset starting at an energy around the 5P-exciton: $E_{1S} + E_{ph} = 2.168\,\mathrm{eV}$.

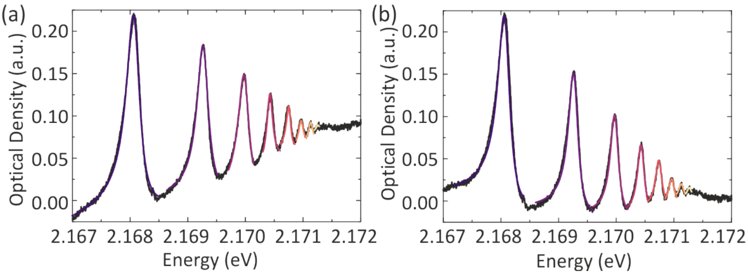

FIGURE 2.7. Absorption spectrum of cuprous oxide P-excitons for states $n = 5 - 12$ with (a) and without (b) phonon background. Even at ultra-low temperatures (1.5 K), there is a reasonable amount of phonon interaction present. The exciton lines have been fitted with asymmetric Lorentzian functions. The phonon background has been subtracted with a simple square root function $y = A \cdot \sqrt{x - E} + B$, with $A = 3.186$, $E = 2.165\,\mathrm{eV}$, and $B = -4.68$.

In atomic transitions, the absorption linewidths are very narrow and given by their lifetimes, according to the energy-time uncertainty relation

$$\Delta E \Delta \tau \geq \hbar. \tag{2.22}$$

The excitation of an atomic transition can be described by an exponentially decaying excited state with a finite life time. It is the time-dependent dipole response of a system after an infinitesimally short excitation (Dirac delta function). Atomic transitions, thus, exhibit a Lorentzian lineshape

$$\alpha\left(\omega\right) = \alpha_0 \frac{\gamma/2}{\left(\omega - \omega_0\right)^2 + \left(\gamma/2\right)^2}, \tag{2.23}$$

with ω_0 being the center frequency, γ the damping constant, and α_0 the amplitude.
In contrast, the P-exciton linewidths in absorption transmission measurements on cuprous oxide are much broader and exhibit an asymmetry with a steeper slope on the high-energy flank. The asymmetry is caused by the coupling of the discrete P-exciton resonance to the phonon-assisted absorption continuum of the 1S-exciton. This leads to a phase change across the resonance, resulting in a Fano-type shape. According to Ref. [99], for $n \leq 10$, the nP-exciton lineshapes can be described by asymmetric Lorentzians of the form

$$\alpha\left(\omega\right) = \alpha_0 \frac{\gamma/2 + 2q\left(\omega - \omega_0\right)}{\left(\omega - \omega_0\right)^2 + \left(\gamma/2\right)^2}, \tag{2.24}$$

with an additional asymmetry parameter q. For higher $n > 10$ the lineshapes become increasingly Gaussian due to the impact of crystal inhomogeneities. The exciton linewidths decrease with increasing principal quantum number n ($\propto n^{-3}$) down to a few µeV for $n = 20$. From Eq. (2.22) and with $\hbar = 6.582 \cdot 10^{-16}$eV $\cdot$ s, this yields exciton lifetimes of several nanoseconds. In cuprous oxide carrier-carrier scattering can be neglected for low excitation powers and relaxation into lower-lying exciton states are strongly suppressed. Furthermore, relaxation by emission of optical phonons scales as n^{-3}. This way, the large excitons are not exposed to too much scattering possibilities, yielding long lifetimes. For $n > 2$ S- and D-excitons follow the same trend as the P-excitons. This was shown by two-photon absorption measurements [13, 36].

The lineshapes change, when absorption spectra are recorded in reflection, as well as in pump-probe configuration. In reflection geometry, the lineshapes become more triangular shaped with a stronger broadening of the resonance at the low-energy flank [102]. Pump-probe spectroscopy has a particular influence on Rydberg excitons in cuprous oxide. The pump beam is introduced to change the optical property of the material in a periodic fashion. To be more specific, the pump laser with energy above the band gap, lifts electrons into the conduction band. These, together with the holes in the valence band, form an electon-hole plasma, which inhibits exciton creation. When the pump laser is off, the probe laser, having intensity several orders of magnitude lower than the pump laser, is being absorbed by the excitons. Pump-probe spectroscopy is a differential spectroscopic method, in which the absorption can decrease or increase due to optical excitation. The signal is a composition of two (asymmetric) Lorentz oscillators. It can be performed in transmission or reflection geometry. For more details on pump-probe spectroscopy see Section 3.2.

2.2.5 *Exciton symmetry representations*

An exciton's symmetry is given by the product of the symmetry of the valence band (hole) Γ_V, the symmetry of the conduction band (electron) Γ_C, and the symmetry of the envelope function (angular momentum l^exc) $\Gamma_\mathrm{env}^{l^\mathrm{exc}}$. In cuprous oxide, the yellow nP-excitons form between the highest valence and the lowest conduction band, which have symmetry Γ_7^+ and Γ_6^+, respectively (see Section 2.2.2). Thus, the exciton symmetry is given by:

$$\Gamma_{\mathrm{exc}} = \Gamma_{\mathrm{V}} \times \Gamma_{\mathrm{C}} \times \Gamma_{\mathrm{env}}^{l^{\mathrm{exc}}} = \Gamma_7^+ \times \Gamma_6^+ \times \Gamma_{\mathrm{env}}^{l^{\mathrm{exc}}} = \left(\Gamma_2^+ + \Gamma_5^+\right) \times \Gamma_{\mathrm{env}}^{l^{\mathrm{exc}}}, \tag{2.25}$$

while in the last step the Algebraic rules for symmetry multiplication have been used [88]. The symmetry property of the pure Coulomb field between electron and hole gives rise to a breaking of degeneracy of all levels with the same principal quantum number n irrespective of their angular momentum quantum number l^{exc}, which is described by the exciton envelope function. The exciton envelope functions are equivalent to the atomic orbitals of the hydrogen wave function and are described by the spherical harmonic functions Y_l^m [103]. These are listed in Table 5.8 in Section 5.1.2 in Cartesian coordinates for $l^{\mathrm{exc}} \in \{0, 1, 2, 3\}$. Their symmetries can be calculated via comparison of character sets with the O_h character table. A complete derivation is given in Section 5.1.2.

The crystal ground state has symmetry Γ_1^+. Therefore, a transition may be allowed if the symmetry of the excitonic state appears in the decomposition of the optical transition driving operator. Furthermore, the influence of Γ_2^+ on the total exciton representation can be neglected, as an optical transition from Γ_1^+ ($s = 0$, $j = 0$) to Γ_2^+ ($s = 0$, $j = 0$) can not be realized with dipolar light ($s_{\mathrm{photon}} = 1$). Henceforth, with the different exciton envelope functions being,

$$\Gamma_{\mathrm{env}}^{S} = \Gamma_1^+ \tag{2.26a}$$

$$\Gamma_{\mathrm{env}}^{P} = \Gamma_4^- \tag{2.26b}$$

$$\Gamma_{\mathrm{env}}^{D} = \Gamma_3^+ + \Gamma_5^+ \tag{2.26c}$$

$$\Gamma_{\mathrm{env}}^{F} = \Gamma_2^- + \Gamma_4^- + \Gamma_5^-, \tag{2.26d}$$

the complete exciton symmetries become:

$$
\begin{aligned}
\Gamma_S &= \Gamma_5^+ \times \Gamma_1^+ &&= \Gamma_5^+ && \text{(2.27a)}\\
\Gamma_P &= \Gamma_5^+ \times \Gamma_4^- &&= \Gamma_2^- + \Gamma_3^- + \Gamma_4^- + \Gamma_5^- && \text{(2.27b)}\\
\Gamma_D &= \Gamma_5^+ \times \left(\Gamma_3^+ + \Gamma_5^+\right) &&= \Gamma_1^+ + \Gamma_3^+ + 2\Gamma_4^+ + 2\Gamma_5^+ && \text{(2.27c)}\\
\Gamma_F &= \Gamma_5^+ \times \left(\Gamma_2^- + \Gamma_4^- + \Gamma_5^-\right) &&= \Gamma_1^- + \Gamma_2^- + 2\Gamma_3^- + 3\Gamma_4^- + 2\Gamma_5^- . && \text{(2.27d)}
\end{aligned}
$$

2.2.6 *The yellow 1S-exciton*

The spatial extension of the yellow 1S-exciton ($a_B^{1S} = 5.3\,\text{Å}$) is comparable to the lattice constant ($a = 4.27\,\text{Å}$). This has several implications for the exciton spectrum, which are considered in the so-called central-cell corrections [9, 104]. Due to the large wave function extension in momentum space, the band structure cannot be taken as parabolic any more. The bands flatten, which results in increased electron and hole masses ($m_{1S} = 2.7 m_e$). The Coulomb interaction screening between electron and hole is reduced, thus, the binding energy is increased. And, the electron-hole exchange interaction lifts the spin degeneracy. The 1S-exciton splits into a threefold degenerate 1S-orthoexciton with total angular momentum quantum number $j = 1$ and binding energy $E_B = 139\,\text{meV}$, and a 12 meV lower lying 1S-paraexciton with $j = 0$ and $E_B = 151\,\text{meV}$. The total S-exciton symmetry is given by $\Gamma_S = \Gamma_2^+\,(1) + \Gamma_5^+\,(3)$.
While the 1S-paraexciton is dipole- and quadrupole-forbidden, the 1S-orthoexciton is weakly quadrupole- and even dipole-allowed when coupling to optical phonons of negative parity. The strongest coupling of the 1S-orthoexciton with the Γ_3^--phonon manifests itself as a square-root shaped density of states, starting one phonon energy above the 1S-exciton. This process, thus, dominates the linear absorption spectrum. The 1S-exciton lifetime accounts for 13 µs, which is ultra-long in semiconductors.

2.3 INTERACTION OF LIGTH WITH MATTER

The investigation of Rydberg excitons in cuprous oxide is based on spectroscopic methods, i.e., interaction of light with matter. Therefore, Maxwell's equations for linear optics as well as the explicit interaction of excitons with a light field are discussed in the following sections. Maxwell's equations for nonlinear optics are shortly outlined with respect to frequency conversion, as second-harmonic generation is used in the experimental setup.

2.3.1 *Maxwell's equations for linear optics*

The interaction of light with matter is theoretically described by Maxwell's equations, the derivation of which can be found in different physics school books for electromagnetism [105–107]. In presence of materia they read in their macroscopic form:

$$\nabla \cdot \boldsymbol{D} = \rho_{\text{ext}} \tag{2.28a}$$

$$\nabla \cdot \boldsymbol{B} = 0 \tag{2.28b}$$

$$\nabla \times \boldsymbol{E} = -\frac{\partial \boldsymbol{B}}{\partial t} \tag{2.28c}$$

$$\nabla \times \boldsymbol{H} = \frac{\partial \boldsymbol{D}}{\partial t} + \boldsymbol{J}_{\textbf{ext}}. \tag{2.28d}$$

These equations link the four macroscopic fields dielectric displacement $\boldsymbol{D}$, magnetic field $\boldsymbol{B}$, electric field $\boldsymbol{E}$ and magnetic induction $\boldsymbol{H}$ with external charge ρ_{ext} and external current density $\boldsymbol{J}_{\textbf{ext}}$.

One can define the constitutive relations:

$$\boldsymbol{B} = \mu_0 \mu \boldsymbol{H} \tag{2.29a}$$

$$\boldsymbol{D} = \varepsilon_0 \varepsilon \boldsymbol{E} \tag{2.29b}$$

$$\boldsymbol{J} = \sigma \boldsymbol{E}, \tag{2.29c}$$

with relative permittivity ε, relative permeability μ, and conductivity σ. From Eq. (2.29b) the polarizability $\boldsymbol{P}$ is introduced via:

$$\boldsymbol{D} = \varepsilon_0 \varepsilon \boldsymbol{E} = \varepsilon_0 \left(1 + \chi\right) \boldsymbol{E} = \varepsilon_0 \boldsymbol{E} + \varepsilon_0 \chi \boldsymbol{E} = \varepsilon_0 \boldsymbol{E} + \boldsymbol{P}, \tag{2.30}$$

with χ being the susceptibility. From calculations in Fourier domain using Eq. (2.29b) and Eq. (2.29c) one can derive the relationship between the relative permittivity ε and the conductivity σ:

$$\varepsilon\left(\omega\right) = 1 + \frac{i\sigma\left(\omega\right)}{\varepsilon_0 \omega}. \tag{2.31}$$

From Eq. (2.31) we see, that relative permittivity and conductivity are complex functions, so is the refractive index $\tilde{n} = \sqrt{\varepsilon}$, too:

$$\tilde{n}\left(\omega\right) = n\left(\omega\right) + i\kappa\left(\omega\right). \tag{2.32}$$

The extinction coefficient κ is linked to the absorption coefficient α from Beer's law $I\left(x\right) = I_0 e^{-\alpha x}$ via:

$$\alpha\left(\omega\right) = \frac{2\kappa\left(\omega\right)\omega}{c}. \tag{2.33}$$

For transmission configuration in absorption spectroscopy, often the optical density is given as a signal measure, in order to avoid inaccuracies due to the sample thickness. It is defined as $OD = \alpha\left(\omega\right) \cdot t$, with t being the thickness of the investigated material.

From Maxwell's equations one can also derive the wave equations. For electromagnetic waves in materia they read:

$$\Delta \boldsymbol{E} - \frac{n^2}{c^2}\frac{\partial^2 \boldsymbol{E}}{\partial t^2} = \mu_0 \frac{\partial^2 \boldsymbol{P}}{\partial t^2}. \tag{2.34}$$

Here, the left-hand side is the wave equation in vacuum conditions, while the right-hand side of Eq. (2.34) describes the interaction of the external light field $\boldsymbol{E}$ with the polarization $\boldsymbol{P}$ of the medium.

2.3.2 *Nonlinear optics: Frequency conversion*

The laser used for experimental investigations is an infrared diode laser that is externally frequency-doubled using a nonlinear crystal in order to obtain visible light. Therefore, the concept of frequency-conversion is shortly discussed.

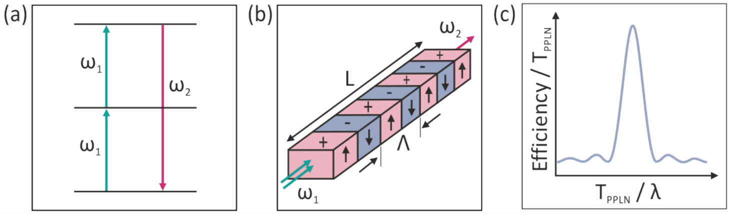

FIGURE 2.8. (a) Principle of second harmonic generation: Two photons of frequency ω_1 are converted to one photon of frequency ω_2. (b) Schematic drawing of a periodically poled lithium niobate (PPLN) waveguide with length L and periodicity Λ. (c) The temperature-dependence of the waveguide efficiency as well as the wavelength-dependence of the optimum waveguide temperature follow a sinc function.

Second harmonic generation (SHG) can be explained in the wave picture as follows: The fundamental electromagnetic wave with frequency ω_1 drives the polarization of a nonlinear optical crystal. Due to the nonlinearity, the polarization oscillates also at the second-harmonic frequency, causing the emission of a coherent electromagnetic wave at the frequency $\omega_2 = 2 \cdot \omega_1$ (see Fig. 2.8 (a)). The derivation is done via Maxwell's equations. The wave equation for nonlinear optical media is given by Eq. (2.34) by inserting a nonlinear polarization $\tilde{\boldsymbol{P}}^{\mathrm{NL}}$ [108]:

$$\nabla^2 \tilde{\boldsymbol{E}} - \frac{n^2}{c^2}\frac{\partial^2 \tilde{\boldsymbol{E}}}{\partial t^2} = \frac{1}{\varepsilon_0 c^2}\frac{\partial^2 \tilde{\boldsymbol{P}}^{\mathrm{NL}}}{\partial t^2}. \tag{2.35}$$

Eq. (2.35) must hold for each frequency component, in particular for the one at the second-harmonic frequency $\tilde{\boldsymbol{E}}_2$. One solution is a plane wave propagating in z-direction:

$$\tilde{\boldsymbol{E}}_2\left(z,t\right) = \boldsymbol{A}_2 e^{i\left(k_2 z - \omega_2 t\right)} + c.c. \tag{2.36}$$

Eq. (2.35) then simplifies to:

$$\frac{d^2}{dz^2}\boldsymbol{A}_2 + 2ik_2\frac{d}{dz}\boldsymbol{A}_2 = -\frac{4d_{\mathrm{eff}}\omega_2^2}{c^2}A_1^2 e^{i\left(2k_1-k_2\right)z}. \tag{2.37}$$

The first term on the left-hand side in Eq. (2.37) can be neglected in the slowly varying amplitude approximation, where

$$\left|\frac{d^2A_2}{dz^2}\right| \ll \left|k_2\frac{dA_2}{dz}\right|. \tag{2.38}$$

Integration from $z = 0$ to $z = L$ gives $A_2\left(L\right)$, and, thus, the second-harmonic intensity

$$I_2 = 2n_2\varepsilon_0 c|A_2|^2 = \frac{8d_{\mathrm{eff}}^2\omega_2^2 I_1^2}{n_1^2 n_2 \varepsilon_0 c^2}L^2 sinc^2\left(\frac{\Delta k L}{2}\right), \tag{2.39}$$

with $d_{\mathrm{eff}} = \frac{1}{2}\chi^{(2)}$. The SHG efficiency increases with the fundamental power I_1, the nonlinearity of the used crystal d_{eff}, and proper phase matching $\Delta k = 2k_1 - k_2$. It follows a sinc function, as shown in Fig. 2.8 (c). Perfect phase matching ($\Delta k = 0$) means that the second-harmonic partial waves generated at different positions within the crystal interfere constructively along the direction of light propagation. Hence, the initial and created wave have to run through the medium with the same phase

$$k_2 = \frac{n\left(\lambda_2\right)\omega_2}{c} \overset{!}{=} 2k_1 = 2\frac{n\left(\lambda_1\right)\omega_1}{c}, \tag{2.40}$$

which implies that the refractive indices $n\left(\lambda\right)$ of the fundamental and the frequency-converted light are equal within the nonlinear optical crystal: $n\left(\lambda_1\right) = n\left(\lambda_2\right)$. This also guarantees momentum conservation. Two photons of momentum $p_1 = n\left(\lambda_1\right) \cdot h/\lambda_1$ are converted into one photon of momentum

$$p_2 = \frac{n\left(\lambda_2\right) \cdot h}{\lambda_2} = \frac{n\left(\lambda_1\right) \cdot h}{1/2 \cdot \lambda_1} = 2p_1. \tag{2.41}$$

Dispersion usually prevents phase matching. But a quasi-phase matching can be achieved by adjusting the temperature of a birefringent crystal and tuning the angle between crystal axis and light propagation as well as using different polarizations of the light waves. In our setup this is realized by using a periodically poled lithium niobate crystal with poling period Λ (see Fig. 2.8 (b)). The quasi-phase matching relation then becomes:

$$\Delta k_Q = 2k_1 - k_2 - \frac{2\pi}{\Lambda}. \tag{2.42}$$

2.3.3 *Light–exciton interaction*

In order to describe the interaction of light with an exciton, we start with treating the Hamiltonian of a charged particle in an electromagnetic field:

$$H = \frac{1}{2m}\left(\boldsymbol{p} - \frac{e}{c}\boldsymbol{A}\right)^2 + V\left(\boldsymbol{r}\right) + e\phi. \tag{2.43}$$

$V\left(\boldsymbol{r}\right)$ is the periodic crystal potential, $\boldsymbol{p}$ the momentum operator, m the effective mass, ϕ and $\boldsymbol{A}$ the scalar and vector potential of the electromagnetic field, respectively. Using Coulomb gauge ($\nabla \cdot \boldsymbol{A} = 0$ and $\phi = 0$) and neglecting higher-order terms proportional to $\boldsymbol{A}^2$, equation Eq. (2.43) simplifies to:

$$H = \left(\frac{\boldsymbol{p}^2}{2m} + V\left(\boldsymbol{r}\right)\right) - \frac{e}{mc}\boldsymbol{A}\cdot\boldsymbol{p} = H_0 + H_{\text{int}}, \tag{2.44}$$

with $H_{\text{int}} = -\frac{e}{mc}\boldsymbol{A}\cdot\boldsymbol{p}$ being the small perturbation describing the interaction between the particle and the field. Using a different gauge

$$\boldsymbol{A}' = \boldsymbol{A} + \nabla\chi \tag{2.45a}$$

$$\phi' = \phi - \frac{1}{c}\frac{\partial\chi}{\partial t} \tag{2.45b}$$

$$\boldsymbol{B}' = \nabla\times\boldsymbol{A}' = \nabla\times\boldsymbol{A} = \boldsymbol{B} \tag{2.45c}$$

$$\begin{aligned}\boldsymbol{E}' &= -\nabla\phi' - \frac{1}{c}\frac{\partial\boldsymbol{A}'}{\partial t}\\ &= -\nabla\phi + \frac{1}{c}\nabla\frac{\partial\chi}{\partial t} - \frac{1}{c}\frac{\partial\boldsymbol{A}}{\partial t} - \frac{1}{c}\frac{\partial}{\partial t}\nabla\chi = \boldsymbol{E},\end{aligned} \tag{2.45d}$$

and using the Ansatz

$$\boldsymbol{E} = \boldsymbol{E}_0 e^{i\left(\boldsymbol{k}\boldsymbol{r}-\omega t\right)} \tag{2.46a}$$

$$\boldsymbol{A} = -\frac{ic}{\omega}\boldsymbol{E}_0 e^{i\left(\boldsymbol{k}\boldsymbol{r}-\omega t\right)} \tag{2.46b}$$

$$\chi = \frac{ic}{\omega}\boldsymbol{E}_0 \cdot \boldsymbol{r} e^{i\left(\boldsymbol{k}\boldsymbol{r}-\omega t\right)}, \tag{2.46c}$$

the vector potential obtains the form:

$$\boldsymbol{A}' = \boldsymbol{A} + \nabla\chi = \boldsymbol{A} + \underbrace{\frac{ic}{\omega}\boldsymbol{E}_0 e^{i\left(\boldsymbol{k}\boldsymbol{r}-\omega t\right)}}_{-\boldsymbol{A}} - \underbrace{\frac{c}{\omega}\left(\boldsymbol{E}_0 \cdot \boldsymbol{r}\right)\boldsymbol{k} e^{i\left(\boldsymbol{k}\boldsymbol{r}-\omega t\right)}}_{\rightarrow 0}. \tag{2.47}$$

The last term in Eq. (2.47) describes higher-order transitions, which, in dipole approximation, vanishes. So, $\boldsymbol{A}' = 0$. With

$$\phi' = \phi - \frac{1}{c}\frac{\partial \chi}{\partial t} = -\boldsymbol{E}_0 \cdot \boldsymbol{r} e^{i\left(\boldsymbol{k}\boldsymbol{r}-\omega t\right)} = -\boldsymbol{E} \cdot \boldsymbol{r}, \tag{2.48}$$

the perturbation term H_{int} becomes the dipole operator with negative parity $-e\boldsymbol{E} \cdot \boldsymbol{r}$:

$$\begin{aligned} H &= \frac{1}{2m}\left(\boldsymbol{p} - \frac{e}{c}\boldsymbol{A}'\right)^2 + V\left(\boldsymbol{r}\right) + e\phi' \\ &= \frac{\boldsymbol{p}^2}{2m} + V\left(\boldsymbol{r}\right) - e\boldsymbol{E} \cdot \boldsymbol{r} = H_0 + H_{\text{int}} \end{aligned} \tag{2.49}$$

This becomes important in Section 5.1, where we investigate optical transitions on the basis of symmetry considerations. For a complete description of the exciton, one adds the corresponding Hamiltonian for the hole and takes into account the Coulomb interaction between electron and hole [92, 93, 109].

2.4 ORBITAL ANGULAR MOMENTUM LIGHT

Light beams with an azimuthal phase dependence of $e^{-il\varphi}$ carry an orbital angular momentum (OAM) of $l\hbar$ per photon. This OAM is independent of the polarization state that is given by the spin angular momentum, $\sigma_z = 0, \pm 1$, for linearly and circularly polarized light. The Poynting vector that is usually parallel to the beam axis, has an azimuthal component, which produces an orbital angular momentum parallel to the beam axis. The momentum circulates about the beam axis, creating an optical vortex [110, 111]. For any given l (unlimited) the beam has l interwined helical phase fronts and looks like a multistart helix [112].

2.4.1 *Mathematical description of OAM light*

The most common form of helically phased beams are the Laguerre-Gaussian laser modes. These cylindrical modes have an explicit phase factor, $e^{-il\varphi}$, and form a complete basis set for paraxial light beams. They read [111, 113, 114]:

$$\begin{aligned} \boldsymbol{A}_{lp}\left(r,\varphi,z\right) =& \boldsymbol{A}_0 e^{ikz}\frac{w_0}{w} exp\left[\frac{-r^2}{w^2}+\frac{ikr^2}{2R}-i\left(2p+|l|+1\right)\phi\left(z\right)\right] \\ & \times\left(\frac{\sqrt{2}r}{w}\right)^{|l|} L_p^{|l|}\left(\frac{2r^2}{w^2}\right)e^{il\varphi}. \end{aligned} \tag{2.50}$$

$\boldsymbol{A}_0$ is the amplitude, w the beam waist, w_0 the beam waist at $z = 0$, R the radius of curvature, $L_p^{|l|}$ the Laguerre polynomials, l the OAM charge number, representing an azimuthal phase change of $2\pi l$ around the circumference, and p the radial index, indicating there are p intensity peaks ($p + 1$ nodes) in radial direction.
Due to a phase singularity on the beam axis, there is zero optical

intensity and neither linear nor angular momentum at the center of the vortex. Therefore the cross-sectional intensity pattern of all such beams looks like a ring that persists no matter how tightly the beam is focused. The angular momentum is associated with regions of high intensity [110]. The time evolution of a helical phase front is indistinguishable from rotation about the beam axis. So, a single rotation of the beam advances or retards its phase by l cycles. All light beams, which possess field gradients, and which are, therefore, not plane waves, will possess a measure of orbital angular momentum [115].

2.4.2 *Creation of OAM light*

Mathematically speaking, OAM light is most easily produced by conversion of Hermite-Gauss beams [110, 111, 114]. When the frequency-degenerate TEM_{01} and TEM_{10} modes oscillate simultaneously in phase quadrature, the resulting TEM_{01}^{*} doughnut modes can exhibit a helical wavefront structure, associated with a phase singularity on the beam axis. Experimentally speaking, OAM arises, whenever a beam‘s phase fronts are not perpendicular to the propagation direction. In other words, the light rays that make up the beam are skewed with respect to its axis. Such light beam can be created by Archimedean spirals or by spiral phase plates.

When circularly polarized light propagates through a slit in the shape of an Archimedean spiral in a metallic plate, the slit edges provide the necessary momentum to excite surface plasmon polaritons on the interface that propagate toward the interior of the spiral [116]. The azimuthally varying radius of the 2D slit profile provides a varying propagation phase to the SPPs excited along the profile. This geometrical phase together with the angular momentum carried by the impinging illumination determines the amount of OAM of the excited plasmonic vortex. Exciting higher order vortices requires highly twisted spirals. To avoid azimuthally varying losses, the Archimedean spirals can be segmented.

Upon transmission through a spiral phase plate with step height Δs, a Gaussian beam of wavelength λ is subject to a phase delay ψ, which depends on the azimuthal angle ϕ [111, 114, 117]:

$$\psi = \frac{\Delta n \cdot s \cdot \phi}{\lambda}. \tag{2.51}$$

Δn is the difference in refractive index between the phase plate and the surrounding. For a pure Laguerre-Gauss beam the total phase delay around the phase plate must be an integer multiple of 2π, thus the physical step height in the spiral phase plate is given by $s = l \cdot \lambda / \Delta n$, and the angular momentum exchanged between the light beam and the phase plate is:

$$L = l \cdot \hbar = \frac{s \cdot \Delta n \cdot \hbar}{\lambda}. \tag{2.52}$$

The evolved helical phase dislocation produced on-axis, causes destructive interference leading to a characteristic ring intensity pattern in the far field. The spiral phase plate, however, is in general not a pure mode converter. Imperfections at the center of the phase plate and slight misalignment of the axis can cause co-production of higher order modes. Furthermore, as the radius r decreases, the above calculations diverge from the exact result, which holds for the paraxial regime only, where $l \cdot \lambda << r$. The order l of the Laguerre-Gauss mode is set by the step height Δs of the spiral phase plate. Using direct laser writing (see Section 3.7.3), spiral phase plates can be either printed directly on a sample, or on the facet of an optical fiber (see Fig. 2.9). The amount of orbital angular momentum imposed to the light by the phase plate can be directly seen from the measured light mode behind the phase plate.

Instead of 3D printing OAM phase plates, one can also use focused ion beam milling in order to mill diffractive optical element structures into the sample (see Fig. 2.10). These include not only an additional amount of orbital angular momentum l but also focusing properties. This might be of advantage for integrated measurements, and strain behavior might be different from 3D printed OAM structures.

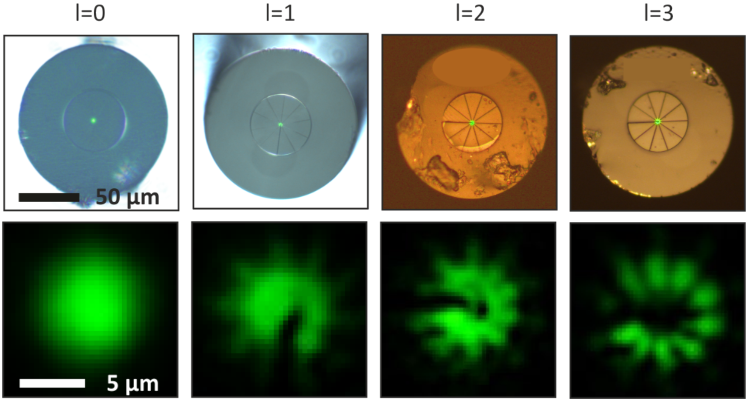

FIGURE 2.9. Top row: Spiral phase plates directly imprinted on the facet of an optical fiber using direct laser writing. Amount of orbital angular momentum l increases from left to right from $l = 0$ to $l = 3$. Bottom row: Measured light mode after propagation through the optical fiber with imprinted phase plate.

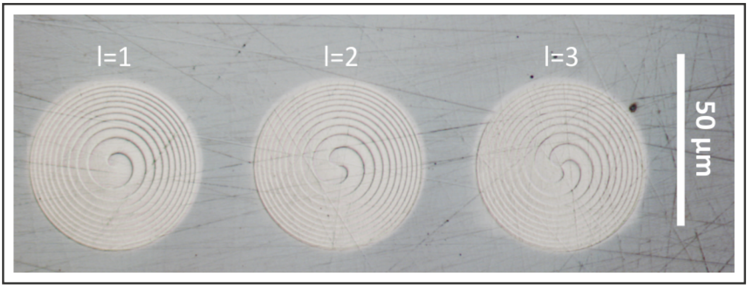

FIGURE 2.10. Diffractive optical element structures with focusing properties and additional orbital angular momentum $l = 1 - 3$ directly milled into the surface of a cuprous oxide crystal.

2.4.3 *Field gradients in OAM light and multipolar transitions*

Light's spatial structure can determine the characteristics of light-matter interaction and lead to strongly modified selection rules [118–123]. Electric quadrupole transitions require a change of two units of angular momentum ($\Delta l = 2$) in an atom and are driven by optical field gradients. A Gaussian beam has a longitudinal field gradient that is very weak. A transverse field gradient due to the spatial structure of the beam front as in Laguerre-Gauss beams, can drive quadrupole transitions, too. In particular, the center of a $\boldsymbol{A}_{10}$ Laguerre-Gauss laser mode exhibits a strong field gradient, where the intensity vanishes. This can be seen from the linear r-dependence in Eq. (2.50) for $l = 1$. In order to make quadrupole transitions similar in magnitude to standard electric dipole transitions ($\Delta l = 1$), good spatial overlap between light field and matter is required, which is guaranteed when using mesoscopic Rydberg excitons with excitation energies in the optical regime. This matter of fact is further developed in Section 5.1.4.

2.5 PLASMONIC NANOSTRUCTURES

Usually, electric dipole transitions determine the outcome of spectroscopic investigations because electric or magnetic quadrupole transitions are three orders of magnitude weaker or even forbidden. By using the transverse field gradients produced by resonant plasmonic antennas, one can manipulate the selection rules and excite quadrupole transitions in a more effective way [124]. Plasmonic antennas channel incoming light into a confined nearfield that comes along with strong field gradients at the edges. Such plasmonic nano-antennas can be directly printed on the cuprite crystal surface using lithography (see Fig. 2.11).

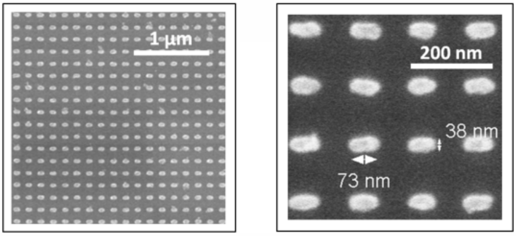

FIGURE 2.11. SEM images of nano-antenna arrays printed onto a polished cuprous oxide crystal flake.

2.5.1 *Optical properties of plasmonic nanostructures*

In 1908, Gustav Mie developed a general theory for the interaction of light with metallic nanoparticles [125]. Upon light incidence, the negatively charged electrons inside the metallic nanoparticle are being displaced from the positively charged ions, while Coulomb interaction leads to a harmonic oscillation. If the nanoparticle diameter is much smaller than the light wavelength ($d \ll \lambda$), the phase of the collective oscillation of the electrons is constant over the entire volume of the nanoparticle and the time-dependence of the electric field can be neglected. This assumption is called the quasistatic approximation.

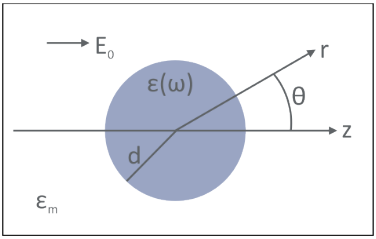

FIGURE 2.12. Sketch of a homogeneous sphere with radius d and dielectric constant $\varepsilon(\omega)$ in a medium with ε_m. The applied external electric field E_0 is parallel to the z axis.

In order to calculate the electric field inside and outside a plasmonic nanoparticle $\boldsymbol{E} = -\nabla\Phi$, one has to solve the Laplace equation for the potential Φ first: $\Delta\Phi = 0$. A complete derivation can be found in [106]. The most simple geometry for the derivation of the optical properties of plasmonic nanostructures is shown in Fig. 2.12. It consists of a homogeneous, isotropic sphere with a radius d and permittivity ε, surrounded by a dielectric environment with permittivity ε_m and an external field in z direction $\boldsymbol{E} = E_0\hat{e}_z$. The general solutions for the potential of a nanosphere read:

$$\Phi_{\text{in}}\left(r,\theta\right) = \sum_{l=0}^{\infty} A_l r^l P_l\left(\cos\theta\right) \tag{2.53a}$$

$$\Phi_{\text{out}}\left(r,\theta\right) = \sum_{l=0}^{\infty} \left[B_l r^l + C_l r^{-(l+1)}\right] P_l\left(\cos\theta\right), \tag{2.53b}$$

with $P_l\left(\cos\theta\right)$ being the Legendre Polynomials of order l, and θ being the angle between the position vector $\boldsymbol{r}$ and the z axis (see Fig. 2.12). The parameters A_l and B_l can be determined by the boundary conditions at $r \to \infty$ $\left(B_1 = -E_0 \text{ and } B_l = 0 \text{ for } l \neq 1\right)$ and $r = d$ $\left(A_l = C_l = 0 \text{ for } l \neq 1\right)$. One obtains:

$$\Phi_{\text{in}}\left(r,\theta\right) = -\frac{3\varepsilon_m}{\varepsilon + 2\varepsilon_m} E_0 r\cos\theta \tag{2.54a}$$

$$\begin{aligned}\Phi_{\text{out}}\left(r,\theta\right) &= -E_0 r\cos\theta + \frac{\varepsilon - \varepsilon_m}{\varepsilon + 2\varepsilon_m} E_0 d^3 \frac{\cos\theta}{r^2} \\ &= -E_0 r\cos\theta + \frac{\boldsymbol{p}\cdot\boldsymbol{r}}{4\pi\varepsilon_0\varepsilon_m r^3}.\end{aligned} \tag{2.54b}$$

From Eq. (2.54b) we see that the potential outside the sphere is a superposition of the applied external field and a dipole field generated by the sphere itself, with the dipole moment of the sphere $\boldsymbol{p}$ accounting for:

$$\boldsymbol{p} = 4\pi\varepsilon_0\varepsilon_m d^3 \frac{\varepsilon - \varepsilon_m}{\varepsilon + 2\varepsilon_m} \boldsymbol{E}_0, \tag{2.55}$$

and the polarizability α:

$$\alpha = 4\pi d^3 \frac{\varepsilon - \varepsilon_m}{\varepsilon + 2\varepsilon_m}. \tag{2.56}$$

In metals, the imaginary part of the permittivity ε can be assumed to be zero. Then, for $\mathrm{Re}\left[\varepsilon\left(\omega\right)\right] = -2\varepsilon_m$, which is known as the *Fröhlich condition*, the denomiator in α is zero, thus, the polarizability exhibits a resonance. In reality, the amplitude of α is of course limited by a non-vanishing contribution of $\mathrm{Im}\left[\alpha\right]$. The resonance frequency is dependent on the nanoparticle diameter d as well as its permittivity ε_m. In air ($\varepsilon_m = 1$), the resonance frequency is $\omega_0 = \frac{\omega_p}{\sqrt{3}}$, with ω_p being the Drude plasma frequency. Having solved the equations for the potential, the electric field $\boldsymbol{E}$ inside and outside the nanosphere can be determined by the Laplace equation:

$$\boldsymbol{E}_{\text{in}} = \frac{3\varepsilon_m}{\varepsilon + 2\varepsilon_m}\boldsymbol{E}_0 \tag{2.57a}$$

$$\boldsymbol{E}_{\text{out}} = \boldsymbol{E}_0 + \frac{3\hat{e}_r\left(\hat{e}_r \cdot \boldsymbol{p}\right) - \boldsymbol{p}}{4\pi\varepsilon_0\varepsilon_m}\frac{1}{r^3}. \tag{2.57b}$$

From Eq. (2.56) and Eq. (2.57a) we see that the resonance in α leads to a resonance in the electric field $\boldsymbol{E}_{\text{in}}$, which can be used for driving enhanced quadrupole transitions (see Chapter 6).

2.5.2 *Tuning of optical properties*

Localized surface plasmon resonances can be excited in particles with arbitrary geometrical shapes, which then act as optical antennas enhancing the optical near-field [126]. Many different antenna structures have been studied [127–129], including discs [130], rod [131, 132] and bowtie [133, 134] antennas, as well as split-ring resonators [135–137]. Also metamaterials [138, 139] and stacked 3D structures [140–142] exhibit plasmon resonances.

The spectral position of plasmon resonances can be tuned by changing their length or aspect ratio [143, 144]. The resonance quality improves with geometrical downsizing [145, 146], which originates from increased radiative damping losses for larger particle size. An increased cross section, and, thus, a boost in optical response can be achieved by using arrays of nanostructures [147, 148]. By designing arrayed structures, one has of course to take care of grating effects by tuning the periodicity away from the antenna resonances to avoid interference of the different modes. Furthermore, in case of close proximity of the single nanoparticles to each other (interparticle distance smaller than about 100 nm) interaction via their optical near-fields sets in. This interaction leads to a hybridization of their modes, which can be observed for example in molecules, where the orbitals of the individual atoms hybridize [149–153].

3

EXPERIMENTAL SETUP

In this chapter the experimental setup used for experiments in this thesis is explained. Spectroscopy on excitons in cuprous oxide requires ultra-low temperatures in order to resolve the exciton lines, which are hidden within a huge phonon background in the crystal. This is realized by using a cryostat, which is explained in Section 3.1. Laser spectroscopy is performed in transmission as well as reflection geometry with a tunable solid state or dye laser. A second solid state or dye laser is used for realizing pump-probe spectroscopy, which is described in Section 3.2. In combination with lock-in detection (see Section 3.3), this technique allows for a more sensitive detection of tiny signals compared to pure absorption spectroscopy. The laser sources are introduced in Section 3.4. The technical connections and data processing are discussed in Section 3.5, while the complete laser setups are shown in Section 3.6. Section 3.7 introduces additional sample components, such as plasmonic nanoantennas, quantum wells, and 3D-printed micro-optics.

3.1 LOW-TEMPERATURE TECHNIQUE: THE CRYOSTAT

The cryostat used is a SM4000-8 Spectromag by Oxford Instruments GmbH (see Fig. 3.1). It features an outer vacuum chamber (OVC) and a 24 l liquid nitrogen (N_2) shield with a liquid nitrogen hold time of at least 48 hours. The OVC is pumped using the HiCube 80 Eco pump by PFEIFFER Vacuum, which reaches a final pressure value below $1 \cdot 10^{-7}$ mbar. The liquid helium (He) bath at the inner of the liquid nitrogen bath has a capacity of 20 l with a hold time longer than 100 hours. In its center there is the variable temperature inset (VTI) with a capillary fed heat exchanger fitted with a heater and a CERNOX sensor for temperature control. The VTI features an automatic needle valve operated via the MercuryITC controller in order to control the helium flow. The samples are placed inside the VTI with a usable sample space diameter of 25 mm. The temperature can be varied from 300 K down to 1.5 K. Optical access is granted from all four sides. The optical windows on the OVC are made of Spectrosil B quartz and have 80 mm diameter on the sides parallel to the magnetic field and 60 mm diameter on the sides perpendicular to the field. The optical windows on the VTI are also Spectrosil B quartz windows with 10 mm diameter. The sample rod can be manually moved by ±15 mm along the axis and rotated by 360 degrees.

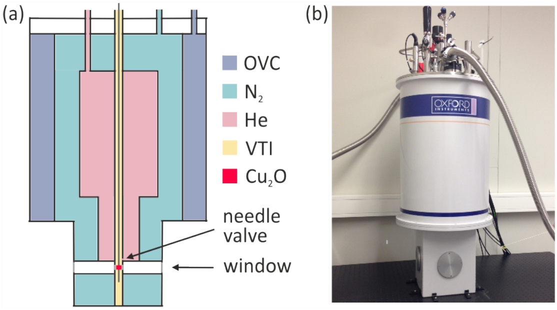

FIGURE 3.1. (a) Schematic drawing of the inner of the cryostat, showing the outer vacuum chamber (OVC), the liquid nitrogen (N_2) and helium (He) tanks, as well as the variable temperature inset (VTI) with needle valve and sample (Cu_2O). (b) Photograph picture of the used cryostat on the laboratory table.

3.2 PUMP-PROBE SPECTROSCOPY

Usually pump-probe spectroscopy is used to measure ultra-fast phenomena using short laser pulses. A pump pulse excites a sample that is then probed by a probe pulse after a certain delay time. Pump-probe spectroscopy in combination with lock-in detection can also be used to enhance small signals hidden within a large background. In cuprous oxide, even at low temperatures, the transmission signal through the crystal is very weak due to its high absorptivity in the visible light range ($\varepsilon = 7.5$). Here the pump beam is introduced to change the optical property of the material in a periodic fashion. The probe beam investigates these changes. Its intensity is several orders of magnitude lower than the pump beam intensity in order not to influence the material optical properties. Pump-probe spectroscopy is a differential spectroscopy method, in which the absorption can decrease or increase due to optical excitation, also known as induced transparency and induced absorption, respectively. It can be performed in transmission or reflection configuration.

The transmission $I(\omega)$ through a sample of thickness t is exponentially dependent on the absorption coefficient $\alpha(\omega)$, following Beer's law:

$$I(\omega) = I_0(\omega)\, e^{-\alpha(\omega)t}, \tag{3.1}$$

with I_0 being the spectrum of the probe laser source. The induced optical density $\Delta\alpha(\omega)\, t$ is then defined as difference of the optical density with and without (α^*, I^*) pump laser:

$$\Delta\alpha t(\omega) = \alpha^*(\omega)\, t - \alpha(\omega)\, t = ln\left(\frac{I(\omega)}{I^*(\omega)}\right). \tag{3.2}$$

One sees from Eq. (3.2) that the induced absorption spectrum is independent of the probe beam source. However, the intensity of the probe beam is indeed very decisive for the singal-to-noise ratio and, therefore, for the detection limit of the induced absorption.

In addition, pump-probe spectroscopy has a particular influence on the investigated system. Light impinging on a semiconductor with energy higher than the band gap energy, lifts electrons into the conduction band. Being more precise, the pump laser will create an electron-hole plasma, which reduces the band gap energy [33, 154]. Furthermore, the probe laser now measures exciton lines with decreased intensity, which will vanish for a band gap shift down to the respective exciton energy. During this, the absorption background stays constant. Accordingly, the pump laser intensity must not be chosen too high.

3.3 LOCK-IN DETECTION

A lock-in amplifier is also known as phase-sensitive rectifier. It can be described as narrow bandpass filter that improves the signal-to-noise ratio. It extracts small signals at a specific (reference) frequency by filtering out DC as well as AC signals of other frequencies and noise. The most important elements in a lock-in amplifier are a signal input for the modulated measurement signal plus an input amplifier, a signal input for the reference signal, a phase shifter and a multiplier for adjustment between reference and measurement signal, and a low-pass for averaging over several signal periods in time. The lock-in amplifier calculates the cross-correlation between measurement and reference signal for a given phase shift. The cross-correlation for signals of different frequencies is zero.

Typically an experiment is excited at a fixed frequency and the lock-in detects the signal at this reference frequency ω_r, which has the form:

$$V_{\text{sig}} \sin\left(\omega_r t + \theta_{\text{sig}}\right). \tag{3.3}$$

The lock-in generates its own reference signal:

$$V_L \sin\left(\omega_L t + \theta_{\text{ref}}\right). \tag{3.4}$$

After amplification and multiplication of the signal with the lock-in reference, the output V_{psd} is composed of two AC signals at frequencies $(\omega_r - \omega_L)$ and $(\omega_r + \omega_L)$:

$$\begin{aligned} V_{\text{psd}} &= V_{\text{sig}} V_L \sin\left(\omega_r t + \theta_{\text{sig}}\right) \sin\left(\omega_L t + \theta_{\text{ref}}\right) \\ &= 1/2 V_{\text{sig}} V_L \cos\left(\left[\omega_r - \omega_L\right] t + \theta_{\text{sig}} - \theta_{\text{ref}}\right) \\ &- 1/2 V_{\text{sig}} V_L \cos\left(\left[\omega_r + \omega_L\right] t + \theta_{\text{sig}} + \theta_{\text{ref}}\right). \end{aligned} \tag{3.5}$$

If the frequencies ω_r and ω_L are the same and the output is filtered through a low pass filter, the output reads:

$$V_{\text{psd}} = 1/2 V_{\text{sig}} V_L \cos\left(\theta_{\text{sig}} - \theta_{\text{ref}}\right). \tag{3.6}$$

In case the phase between the signals, $\theta_{\text{sig}} - \theta_{\text{ref}}$, changes with time, $\cos\left(\theta_{\text{sig}} - \theta_{\text{ref}}\right)$ will change and V_{psd} will not be a DC signal. Therefore a phase-locked-loop locks the internal reference oscillator to the external reference. Furthermore, by adjusting θ_{ref} one can make $\theta = \theta_{\text{sig}} - \theta_{\text{ref}} = 0$. This way, one would measure V_{sig} only. And for $\theta = 90^\circ$ there will be zero output. In order to eliminate this phase dependence, a second phase-sensitive detector is added, which multiplies the signal with the reference oscillator shifted by 90°, i.e.,

$$V_L \sin\left(\omega_L t + \theta_{\text{ref}} + 90^\circ\right). \tag{3.7}$$

The low-pass filtered output then becomes:

$$V_{\text{psd},2} = 1/2 V_{\text{sig}} V_L \sin\left(\theta_{\text{sig}} - \theta_{\text{ref}}\right). \tag{3.8}$$

This results in two outputs: the in-phase component X and the quadrature component Y:

$$X = V_{\text{sig}} \cos\left(\theta\right) \tag{3.9a}$$

$$Y = V_{\text{sig}} \sin\left(\theta\right). \tag{3.9b}$$

By computing the magnitude R of the signal vector (see Eq. (3.10a)), the phase dependency is removed. The phase θ between the signal and lock-in reference, can be measured according to Eq. (3.10b):

$$R = \sqrt{X^2 + Y^2} = V_{\text{sig}} \tag{3.10a}$$

$$\theta = \tan^{-1}\left(Y/X\right). \tag{3.10b}$$

The lock-in amplifier used is SR830 DPS by Stanford Research Systems. It has a variable sensitivity range adjustable from 2 nV to 1 V. Depending on the sensitivity setting, the full scale DC output of signal amplitude R is 10 V. When changing the sensitivity setting S, the output value $U_{out,R}$ needs to be adjusted according to:

$$U_{out,R} = \frac{R}{S} \cdot 10\,\text{V} \Leftrightarrow R = U_{out,R} \frac{S}{10\,\text{V}}. \tag{3.11}$$

3.4 LASER SOURCES

For pure transmission or reflection spectroscopy on cuprous oxide Rydberg excitons, one tunable probe laser is required. In order to perform pump-probe spectroscopy an additional modulated pump laser is needed. Experiments for this thesis have been performed in our own lab in Stuttgart as well as in a lab in Dortmund. The Stuttgart lab features solid state lasers (in the following named pump and probe laser 1), while the Dortmund lab features dye lasers (in the following labeled pump and probe laser 2). The different laser systems and main optical elements used for the experiments are explained in the following subsections.

3.4.1 *Pump laser 1*

The pump laser RLTMGL-561-30 by Roithner Lasertechnik, used in the Stuttgart lab, lases at 561 nm (2.21 eV), which is 10 nm above the band gap of cuprous oxide. It introduces an electron-hole plasma in the semiconductor, so exciton states cannot be formed with the pump laser on. The maximum laser power is 30 mW, however, above 6 mW output power, the pump laser operates unstable and is not suitable for a pump-probe experiment with lock-in detection scheme. The pump laser can be modulated internally using a TTL signal up to 10 kHz, but, turning on and off the laser constantly leads to additional noise. Therefore, the pump laser is modulated externally using an acousto-optical modulator (AOM) at max. 10 kHz modulation frequency.

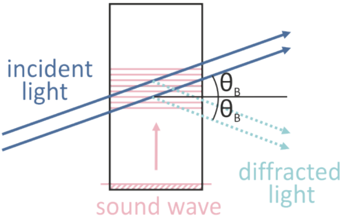

FIGURE 3.2. (a) Schematic drawing of an acousto-optical modulator. Sound waves create a grating, which the incident light is diffracted on when the Bragg angle condition (θ_B) is met.

The AOM used is the model AOMO 3200-125 together with the controller AODR 1200AF.AUF0-1.0 by Gooch & Housego. It is made of TeO_2, requires a 1 mm laser beam diameter, and features a Bragg angle of 15.1 mrad at 633 nm and a 200 MHz frequency shifter. Acousto-optical devices operate by Bragg diffraction of an incident light beam from a moving acoustic wavefront (see Fig. 3.2). The acoustic wave generates a refractive index wave, which acts as a sinusoidal grating in the optical material. An incident laser beam passing through this grating will be diffracted into several orders when certain requirements are met: First, the laser beam polarization should be perpendicular to the mounting surface of the modulator. Second, the acoustic beam must be slightly rotated off perpendicular to the optical beam so that the Bragg angle condition is met. Third, the optical beam focus should be located at the acoustic column. When the laser beam passes through the acoustic wave in the acousto-optic material, the interaction causes the frequency of the light to be shifted by an amount equal to the acoustic frequency. This shift, however, is small enough to be neglected in the experiments.

3.4.2 *Probe laser 1*

In order to perform spectroscopy on the complete yellow Rydberg exciton series in cuprous oxide, the probe laser has to be tunable over a 7 nm wavelength range from 577 nm to 570 nm. The laser linewidth needs to be small enough in order to resolve the single exciton lines. The linewidths of 15P- and 5F-excitons account for 20 µeV or 5 GHz only, and even less for respective higher principal quantum number states.
Diode lasers are cheap, compact, and highly efficient. They operate at low powers, have a high resolution, and are tunable. Unfortunately, some wavelengths or power regions can't be accessed yet. For our experiments in the Stuttgart lab, we use the infrared external cavity diode laser (ECDL) DL pro by Toptica, which covers

the wavelength range from 1115 nm to 1163 nm. In combination with a nonlinear frequency conversion technique, we are then able to access the yellow Rydberg exciton series in cuprous oxide.

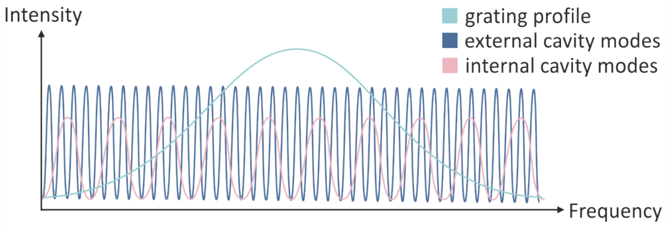

FIGURE 3.3. Competing modes in an ECDL. Adjusting the grating angle shifts the center of the grating profile and simultaneously changes the external cavity length, thus, shifts the external cavity modes as well. Adjustment of diode current and temperature shifts the internal cavity modes.

The DL pro diode laser by Toptica features an anti-reflection (AR) diode with an antireflection-coated output facet, so it does not lase without external feedback and its internal resonator affects the mode selection much less. The AR coating further improves the tuning properties and mode stability of an ECDL. In addition, the ECDL is grating-stabilized. An optical grating is mounted in front of the laser diode, while a second resonator forms externally between the diode's back facet and the feedback element. The laser diode is in Littrow configuration, meaning that the first-order beam from the grating is directly reflected into the diode. The grating filter, the semiconductor gain profile, the internal laser diode modes, and the external cavity modes determine the lasing mode(s). This is illustrated in Fig. 3.3. Precise temperature and current control as well as proper matching of the components are important for a stable single-mode operation. A mode-hop free tuning range of at least 20 GHz can be reached with a laser linewidth below 1 MHz.

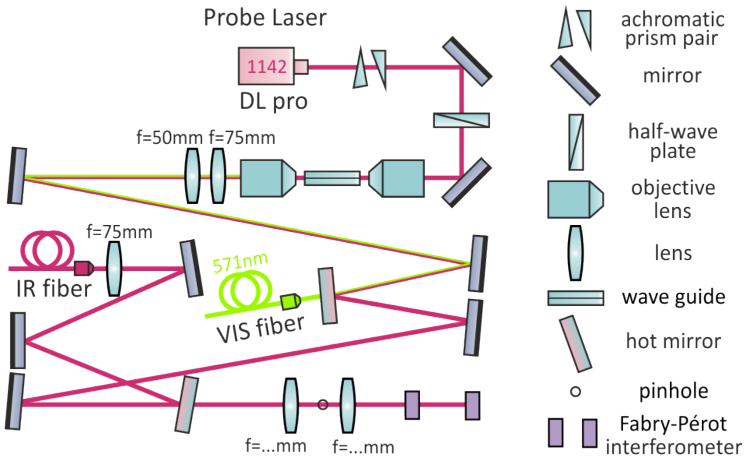

FIGURE 3.4. Schematic drawing of probe laser 1 used in the Stuttgart lab.

In Fig. 3.4 a schematic drawing of the probe laser is shown. Laser light at 1142 nm is emitted from the Toptica DL pro diode laser. An achromatic prism pair corrects the laser spot shape to be circular. A half-wave plate adjusts the polarization to be horizontal. An aspheric objective lens (5725-C-H by Newport, 16x magnification, NA=0.3, 1050-1600 nm) focuses onto the periodically poled lithium niobate (PPLN) waveguide for second harmonic generation. Another objective lens (10x magnification, NA=0.25) collimates the fundamental and second-harmonic beam. Two further lenses adjust the laser spot size, and two mirrors couple the visible light at 571 nm into an optical fiber. A hot mirror separates the infrared (IR) light from the visible light. The IR light is aligned into a Fabry-Pérot interferometer after laser spot size adjustment using two lenses (focal length $f_1 = 75$ mm, $f_2 = 50$ mm). Another hot mirror separates parts of the infrared light, which is coupled into another optical fiber using two mirrors and a lens with focal length $f = 75$ mm. This second fiber is connected to a spectrometer, which is used for wavelength monitoring.

3.4.2.1 *Frequency conversion, tuning and monitoring*

In order to frequency-double the laser light from the ECDL used in our setup, a periodically poled, MgO-doped lithium niobate crystal is used. Due to its poor performance with respect to SH conversion, waveguides have been fabricated on the $+Z$ facet of the crystal with channel depth of 2 to 4 μm with a single grating of dimension $20 \times 3.9 \times 0.5\,\mathrm{mm}^3$. The crystal is designed for SH conversion from 1142 to 571 nm with 50% input coupling efficiency. It has been fabricated by GWU Lasertechnik using the proton exchange technique. The waveguides only support the tranverse-magnetic modes. Therefore coupling into the waveguide is difficult. Two objective lenses are used to couple light into and out of the crystal. Furthermore, waveguides are quite vulnerable to high-power irradiating light, because the temperature distribution along the optical path might be uneven. As the temperature is crucial for quasi phase matching, the noise level in waveguides is higher. A temperature controller monitors and adjusts the waveguide temperature for quasi-phase matching and maximum frequency conversion efficiency.

In order to coarsely change the ECDL wavelength λ, the angle of incidence α on the grating is varied by turning the grating screw manually. Under light incidence, a grating yields a diffractive pattern according to:

$$2d \sin(\alpha) = m\lambda, \tag{3.12}$$

with d being the grating spacing, and m being the diffracted order. At the blaze angle α_B, the grating has the maximum reflection. Because the laser always runs at the largest overall gain, by changing the angle, it hops to another longitudinal mode and emits at a new wavelength. This way, rough tuning of 50 pm wavelength steps (20 GHz and 80 μeV) can be achieved. Fine-tuning of the laser wavelength is realized by changing the length of the external cavity. This smoothly shifts the supported single longitudinal mode the laser is running on. Mode-hops occur whenever the overlap of the external cavity modes with the internal ones is larger at a different spectral position. Therefore, a large mode-hop-free tuning range is difficult to achieve and succeeds only with accurate synchronization (feed forward) of as many contributions as possible, i.e., simultaneously varying grating angle, length of external cavity and laser diode current.

Absolute spectral position determination is done via a spectrometer. For the experiments in this thesis we use the AQ6317B Optical Spectrum Analyzer by ANDO electric co., which features a wavelength acurracy of ±50 pm in the infrared spectral range. This corresponds to shifts in the visible spectrum of up to 0.1 meV. Later, by comparison with literature values, we noticed that the spectrometer yields a systematic absolute energy shift of 1.3 meV. This energy shift has been corrected for in all data shown in this thesis. In future experiments the spectrometer is going to be replaced by the wavelength meter WS6-200 by TOPTICA Photonics AG with higher accuracy and negligible uncertainty in absolute frequency position (below 200 MHz / 0.8 pm / 0.9 eV).
In combination with the spectrometer, the relative wavelength range is monitored by a Fabry-Pérot interferometer with a linewidth of below 2 MHz in order to ensure mode-hop-free tuning. The Fabry-Pérot interferometer FPI100 by TOPTICA Photonics is made of two partially reflecting surfaces in a confocal arrangement. The cavity diameter is $d = 75\,\text{mm}$ and the free spectral range (FSR) is 1 GHz, corresponding to 4 µeV. For a Fabry-Pérot ethalon we have:

$$2d\sqrt{n^2 - \sin^2\alpha} = m\lambda, \tag{3.13}$$

meaning that for each wavelength λ one can calculate an angle α with maximum transmission. The angle dispersion for order $n = 1$ reads:

$$\frac{d\alpha}{d\lambda} = \frac{1}{\lambda \tan \alpha}. \tag{3.14}$$

For fixed d, n, α, several spectral lines are transmitted simultaneously. For $\alpha = 0$ and $n = 1$ these have a frequency distance of:

$$\Delta f_D = c/2d. \tag{3.15}$$

If the frequency width $\delta\lambda$ is smaller than the dispersion range $\Delta\lambda$ a unique frequency selection is possible. This is characterized by the finesse, given by the mirror reflectivity R:

$$F = \frac{\Delta\lambda}{\delta\lambda} = \frac{\pi\sqrt{R}}{1 - R}. \tag{3.16}$$

3.4.2.2 *Laser power stabilization*

In a diode laser, the laser power increases with increasing diode current. As we scan the diode current during a wavelength scan, the output power varies. For spectroscopic measurements, the laser power should be constant for all wavelenghts. Therefore, the output power must be stabilized. We use the laser power controller (LPC) by Brockton Electro-Optics Corp.. Horizontally polarized light passes through a liquid crystal modulator followed by a T:R 98:2 beam splitter. The reflected light is used for indirect power measurement by an internal photodiode. The LPC operates in continuous loops of reading out the photodiode and adapting the transmitted power to the set value using a liquid crystal modulator. This loop is done multiple thousand times per second. This way, the output power is stabilized during the laser scan. Nevertheless, the maximum output power is limited when scanning over the maximum laser tuning range of 20 GHz. For fine-tuning the laser wavelength, the diode current is continuously decreased from 245 mA to 150 mA, so the output power decreases as well. Furthermore, very fast changes can hardly be stabilized. Therefore, a 15 GHz range, which corresponds to 60 pm or 60 μeV, is scanned within 1 s.

3.4.3 *Pump and probe lasers 2*

For measurements in the Dortmund lab two dye lasers (Sirah Matisse DS) were used, which offer a high spectral resolution of 5 neV. The dye used is Rhodamine 6G, which covers the wavelength range from 620 nm to 565 nm. The wavelength can be scanned continuously via software control and is read out by a high-precision wavelengthmeter (HighFinesse WSU). One dye laser is pumped by the laser *Verdi V-10* from Coherent company, the other by the laser *Finesse* from Laser Quantum company with a power of 7 W each. The laser light is coupled into a fiber to maintain a stable beam diameter for all wavelengths.

3.5 TECHNICAL CONNECTIONS AND DATA PROCESSING

The collimated measurement signals are detected via photodiodes, which are read out by high-speed multimeters or an oscilloscope connected to a computer. A reference signal is always recorded in order to compensate for laser interferences. For pump-probe measurements a lock-in amplifier is interconnected between photodiode and multimeter or oscilloscope. The precise configurations used in the different lab setups are described in the following subsections and illustrated in Fig. 3.5, Fig. 3.6, and Fig. 3.7.

3.5.1 *Stuttgart lab*

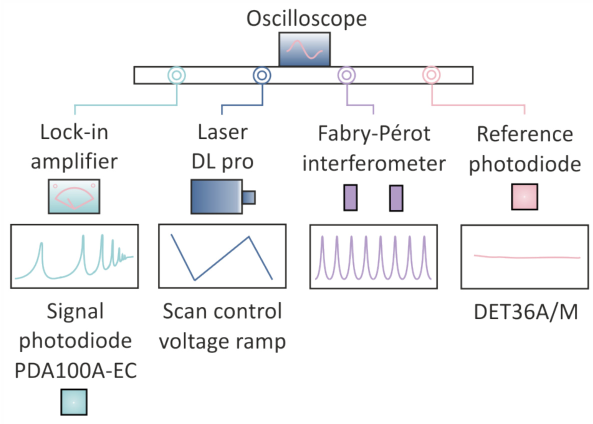

FIGURE 3.5. Schematic drawing of the technical connections in the measurement setup used for pump-probe measurements in reflection geometry in our lab in Stuttgart.

The setup used for measurements in the Stuttgart lab has been built and optimized during this thesis. A schematic drawing illustrating the technical connections is shown in Fig. 3.5. The measurement signal is detected using the photodiode PDA100A-EC by Thorlabs with adjustable gain. By increasing the gain, the signal is increased. However, at the same time, the bandwidth is reduced. While at 0 dB gain the bandwidth is 2.4 MHz, at 70 dB gain it is only 5.9 kHz. The reference signal is detected using the Si biased photodiode DET36A/M by Thorlabs. A photodiode generates a photocurrent when light is absorbed. It is a fast and highly linear measurement device. The silicon photodiodes used, feature a low dark current and are sensitive in the region from visible to near infrared light. The bandwidth f_{BW} and the rise time response t_r can be cacluated via the junction capacitance C_j and the load resistance R_{LOAD}:

$$f_{BW} = \frac{1}{2\pi R_{\text{LOAD}} C_j}, \tag{3.17}$$

$$t_r = \frac{0.35}{f_{BW}}. \tag{3.18}$$

The noise equivalent power (NEP) is the generated root-mean-square signal voltage at a signal-to-noise ratio SNR = 1. The NEP determines the ability of the detector to detect low level light. In general, the NEP increases with the active area of the detector and is given by:

$$NEP = \frac{E_{\text{inc}} \cdot Area}{\text{SNR} \cdot \sqrt{\Delta f}}, \tag{3.19}$$

with Δf being the noise bandwidth, and E_{inc} the incident energy in units of W/cm^2.

The photodiode signals are read out by the USB oscilloscope PicoScope 4824 by Pico Technology Ltd., which is connected to a computer. The oscilloscope features eight input channels with 12 bit vertical resolution and a 80 MS/s sampling rate. It has a 20 MHz bandwidth, a 256 MS buffer memory, and a fast USB 3.0 interface. For pump-probe measurements the signal photodiode is linked to the oscilloscope via the lock-in amplifier SR830 DPS by Standford Research Systems (see Section 3.3). The probe laser diode current ramp as well as the Fabry-Pérot interferometer peaks are monitored on the oscilloscope in order to calculate the frequency scale. The data are evaluated using Python and Origin software.

3.5.2 *Dortmund lab*

The setup in the Dortmund lab has been partly rearranged for measurements for this thesis. The cryostat is slightly tilted around its

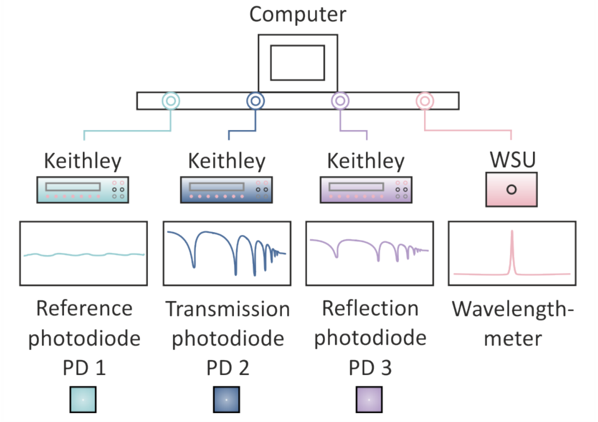

FIGURE 3.6. Schematic drawing of the technical connections in the measurement setup used for pure transmission and reflection measurements in Dortmund.

vertical axis in order to eliminate interference patterns from the cryostat windows. Pump and probe lasers are focused onto the sample in the cryostat. The probe spot has a diameter of about 100 µm while the pump spot has a slightly larger diameter of 300 µm in order to guarantee a homogeneously spread pump power density. The pump laser is set to a fixed wavelength, $\lambda_{\text{pump}} = 561\,\text{nm}$, and modulated at 5 kHz with a chopper wheel. While the pump beam is blocked, the probe beam is collimated behind the cryostat and detected by a photodiode with variable gain (New Focus Large-Area Photoreceiver). Two other photodiodes in front of the cryostat collect a reference as well as a reflection signal. The photodiodes are read out by high-speed multimeters (Keithley 2000) connected to a computer (see Fig. 3.6 and Fig. 3.7).

In order to measure an absorption spectrum, the probe laser wavelength is continuously scanned and signals from all photodiodes are recorded simultaneously with a LabView program. The scan speed is typically 8 µeV per second (2 GHz/s). In order to remove interferences in the measurement data, the probe signal $V_{\text{probe}}\left(\lambda\right)$

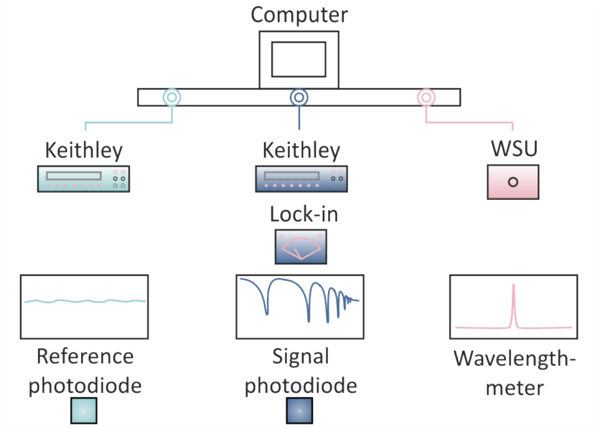

FIGURE 3.7. Schematic drawing of the technical connections in the measurement setup used for pump-probe measurements in transmission configuration in Dortmund.

is divided by the reference signal $V_{\mathrm{ref}}(\lambda)$. As all diode voltages are directly proportional to the detected light intensity $V \propto I$, the optical density $OD(\lambda)$ can be evaluated, except for an unknown offset:

$$\begin{aligned} OD(\lambda) = \alpha(\lambda)\, t &= -\ln\left(I(\lambda)/I_0\right) \\ &= -\ln\left(V_{\mathrm{probe}}(\lambda)/c_{\mathrm{loss}} V_{\mathrm{ref}}(\lambda)\right) \\ &= -\ln\left(V_{\mathrm{probe}}(\lambda)/V_{\mathrm{ref}}(\lambda)\right) + \ln\left(c_{\mathrm{loss}}\right), \end{aligned} \tag{3.20}$$

with $\alpha(\lambda)$ being the wavelenght-dependent absorption coefficient, t the sample thickness, and c_{loss} a factor that accounts for all gain and conversion factors. It is equivalent to I_0, which does not need to be measured explicitly. The overlap of pump and probe lasers is optimized by maximizing the signal height of the differential transmission measured with the lock-in scheme.

3.6 COMPLETE LASER SETUPS

Different setups have been used throughout this thesis: A pure transmission and reflection spectroscopy setup in the Dortmund lab, a pump-probe spectroscopy setup in transmission configuration in Dortmund, and a pump-probe spectroscopy setup in reflection configuration in our lab in Stuttgart. The respective schematic drawings are shown in Fig. 3.8, Fig. 3.9, and Fig. 3.10.

For constant, moderate, and interference-free laser intensity, different laser stabilization and tuning units, as well as different optical elements are included in all three setups. The freely propagating laser light is focused onto the sample in the cryostat and the scattered transmitted or reflected signals are collimated using optical lenses. In order to map the sample surface, a CCD camera is installed in the light path – in transmission or reflection configuration – via a flip-mirror, accompanied by additional illumination provided by a flash lamp.

In the Dortmund setups (see Fig. 3.8 and Fig. 3.9), the dye laser output intensity may vary strongly during a wavelength scan. Therefore, each light beam is stabilized by a BEOC laser power controller (same as in Section 3.4.2.2) to reduce fluctuations in the signal to a minimum. The combination of a half-wave plate and a Glan-Taylor prism allows for further attenuation of the laser light. To avoid interferences, these optical elements are slightly tilted. A pellicle beamsplitter is placed in the light path in order to capture a probe reference beam with photodiode PD 1. In pure transmission and reflection spectroscopy (Fig. 3.8), the collimated transmitted signal is focused onto photodiode PD 2, while the reflected signal is captured by photodiode PD 3. The pump laser in pump-probe experiments (Fig. 3.9) is modulated using a chopper wheel.

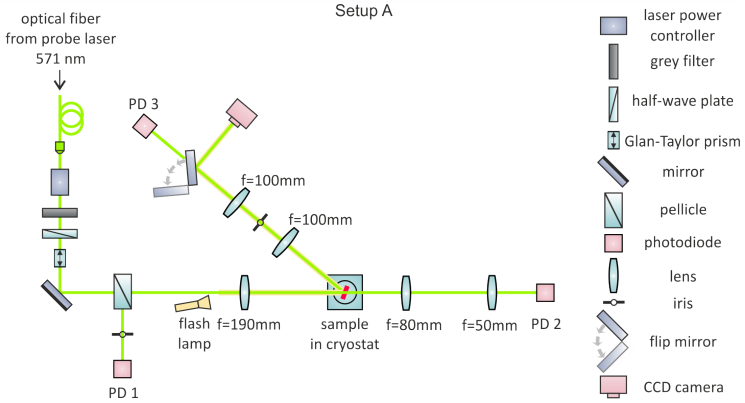

FIGURE 3.8. Pure transmission and reflection spectroscopy setup in Dortmund.

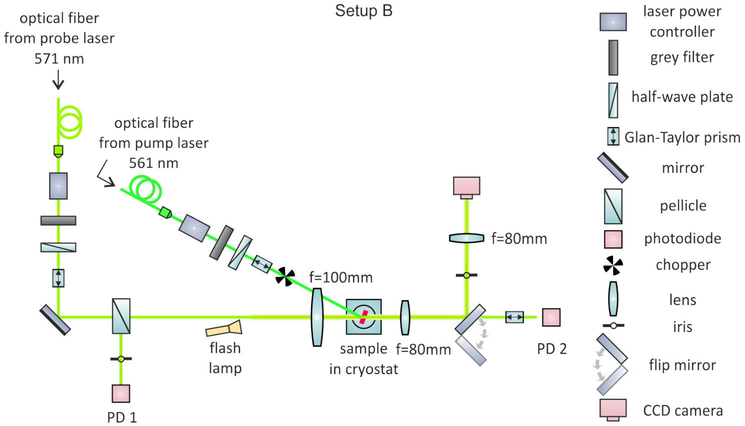

FIGURE 3.9. Pump-probe setup in transmission configuration in the Dortmund lab.

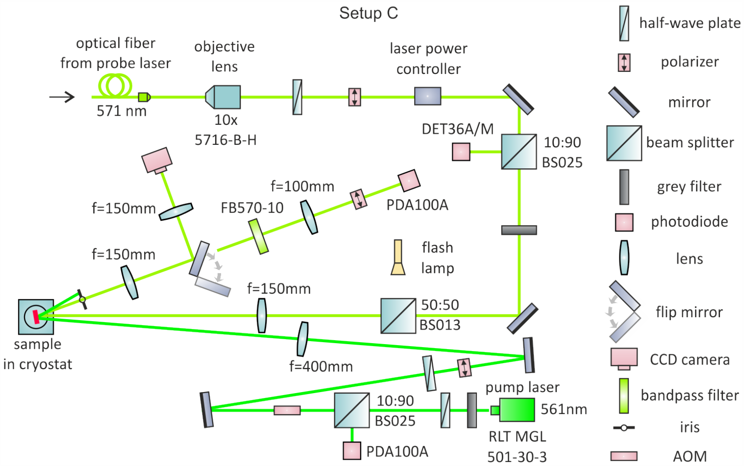

FIGURE 3.10. Pump-probe setup in reflection configuration in our lab in Stuttgart.

In pump-probe experiments it is important to filter out the pump beam from the probe beam for signal detection. This can be done by using different polarizations of the two beams and a Glan-Taylor prism (see Fig. 3.9) or by using narrow bandpass filters and mechanical shutters (see Fig. 3.10).

Also in the Stuttgart setup (Fig. 3.10) a BEOC laser power controller stabilizes the probe laser beam, after the beam diameter is adjusted using an objective lens and the polarization is defined using a half-wave plate and a polarizer. A probe laser reference as well as a pump laser reference are captured using silicon photodiodes DET36A/M and PDA100A, respectively. The pump laser is modulated using an acousto-optical modulator (AOM). Polarization is adjusted by the combination of a half-wave plate and a polarizer. The reflected sample signal is detected by photodiode PDA100A.

Setup A (Fig. 3.8) is used for absorption spectroscopy in transmission configuration on cuprous oxide with orbital angular momentum light. The results are shown in Section 5.2. It is also used for acquisition of pure reflection spectra from antenna-coupled cuprous oxide Rydberg excitons, treated in Section 6.2. Relative transmittance and reflectance spectra from antenna-coupled cuprous oxide Rydberg excitons are obtained with Setup B (Fig. 3.9) and C (Fig. 3.10), respectively, and discussed in Section 6.3.1 and Section 6.3.2. Setup C is also used for examining possible influences of pump-probe spectroscopy on antenna-coupled cuprous oxide Rydberg excitons, covered in Section 6.4.

3.7 SAMPLE COMPONENTS

3.7.1 *Plasmonic nanostructures*

An in-house implementation of a numerical Maxwell solver based on the Fourier modal method is used in order to simulate the antenna response and, thus, to design the antenna [155, 156]. We use 30 nm wide and 60 to 110 nm long aluminum antennas, arranged in $200 \times 200\,\mu\text{m}^2$ large arrays with periodicity of 160 nm. This guarantees optical access in the experiment. The surface becomes equipped with a large number of field gradients when being illuminated with a focused light beam. Under ideal conditions the nanoantenna geometry we employed may result in a field enhancement factor of ten [157, 158]. The field gradient enhancement, however, is difficult to determine. A Rayleigh anomaly at $\lambda = 450$ nm, the cuprous oxide absorption edge at 590 nm, and the large width of the resonances ($\geq$ 100 nm), limit our abilities in shifting the resonance across the optimum exciton wavelength at 571 nm.

The nanoantennas are fabricated directly onto the polished cuprous oxide surface with standard electron beam lithography (Raith eLINE Plus). The bare cuprite sample is cleaned in an ultrasonic bath with acetone and propanol. The sample is glued onto a glass substrate using resin with $T_{\mathrm{melt}} = 60°\mathrm{C}$ (Struers GmbH). The positive, high-resolution photoresist AR-P 6200 (CSAR 62, Allresist) is spin-coated onto the sample. The antenna arrays are defined and written by electron beam exposure at 20 kV and an area dose of 65 µm/cm^2. At the exposed areas the photoresist chains break up so they become dissolvable in the developer. After development, an adhesive layer of 2 nm titanium then 20 nm aluminum are consecutively evaporated using an electron gun evaporator. A lift-off process is started with a commercial n-ethyl-2-pyrrolidon (NEP)-based remover (Allresist) at 60 °C. Afterwards the structured cuprite flake is cleaned with acetone and propanol. The different fabrication steps are visualized in Fig. 3.11. For more details about the fabrication process see Ref. [128].

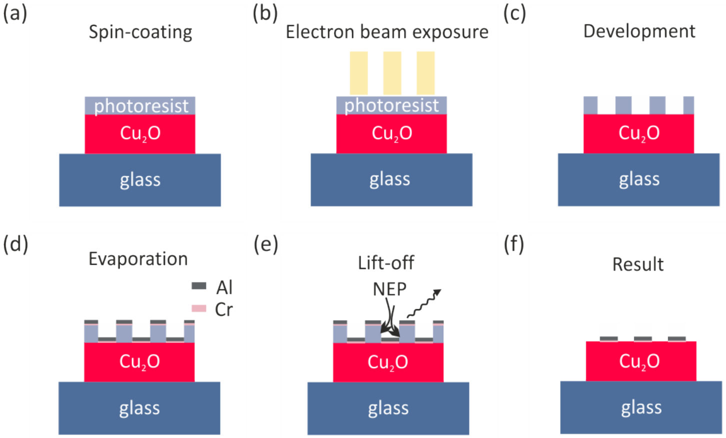

FIGURE 3.11. Scheme of single layer electron beam lithography. The main steps are exposure of PMMA resist, development, Au (or other metal) evaporation, and lift-off. Figure based on Ref. [128].

3.7.2 *Quantum wells in cuprous oxide*

A quantum object being confined into one or several dimensions, experiences an energy shift on quantum scale, which can be useful for quantum technology, such as optical switching applications. Typically, the Bohr radius of an exciton in a semiconductor, such as GaAs or CdTe, is on the order of 10 nm. To achieve quantum confinement, the quantum well width needs to be somewhat smaller than the object to be confined. For GaAs this makes typically 6 nm small quantum wells, which need to be grown in complicated processes. In Cu_2O the Bohr radius of a Rydberg exciton excited to a state with principal quantum number $n = 13$ is 250 nm, which is 25 times larger than in GaAs. These mesoscopic dimensions can easily be fabricated using focused ion beams, milling the wells directly into the cuprite substrate.

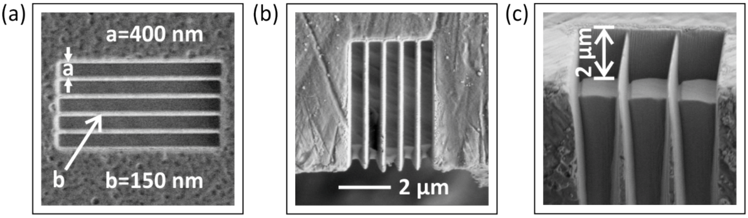

Figure 3.12. Cuprous oxide quantum wells for Rydberg excitons. The huge size of Rydberg excitons allows mesocopic confinement geometries in the hundreds of nanometer to a few micrometer range that can be fabricated using focused ion beams.

Recent advances in focused ion beam milling make it possible to fabricate tailored quantum wells with widths in the hundreds of nm range, as shown in Fig. 3.12. We use the Raith IonLine Plus. Au^+ ions are focused by an aperture system and hit the cuprous oxide sample with high energy. This way, atoms are knocked out from the crystal and sucked inside the vacuum. The IonLine system contains a pattern generator that allows to use the focused ion beam for writing complex lithographic structures with high precision.

3.7.3 *Micro-optics by direct laser writing*

In order to design an integrated and scalable quantum system, we combine Rydberg excitons with nanophotonic structures, such as high-quality 3D-printed micro-optics. We fabricate 3D-printed microlenses and OAM phase plates on optical fiber facets, as well as OAM phase plates and fiber chucks on cuprite crystal surfaces. Prior to printing, the fiber facets are cleaved and the polished cuprite crystals are exposed to an oxygen plasma to increase the adhesion of the polymerized structures. The designs of a phase plate and a fiber chuck are shown in Fig. 3.13.

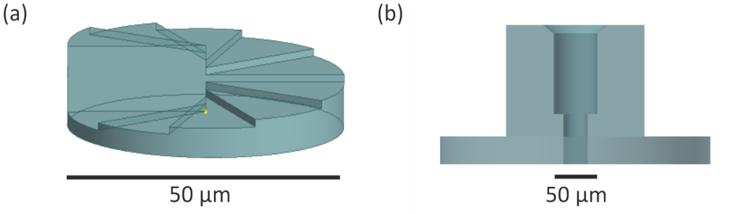

FIGURE 3.13. Design of 3D-printed phase plate (a) and fiber chuck (b).

The system used for direct laser writing is the commercial microfabrication system Photonic Professional GT (Nanoscribe GmbH). This 3D printer uses laser-induced two-photon polymerization to harden a liquid photoresist (see Fig. 3.14 (a)). The photoresist is drop-coated on a substrate. The laser is focused by a microscope objective that is directly immersed into the resist (dip-in laser lithography). A small polymerized region, called voxel (volume pixel, see Fig. 3.14 (b)), is created in the laser focus and can be moved through the resist. This way, arbitrary 3D structures can be created. The setup is in dip-in configuration, meaning the sample is flipped upside down. It is mounted on a 3D piezo stage as well as on a mechanical xy-stage (see Fig. 3.14 (c)). The focusing microscope objective is mounted on a z-drive, and a pair of galvanometric mirrors allow for scanning through the xy-plane. Before starting the printing process, a 3D model of the structure is designed and decomposed into slices. Each slice consists of many parallel hatching lines. For each slice the voxel is scanned along the lines. After the printing process is finished, the remaining liquid photoresist is dissolved by immersion in a developing solution (mr-Dev 600, micro resist technology) for 25 min and subsequently in isopropyl alcohol for 5 min. The printed micro-optics and samples are dried with nitrogen.

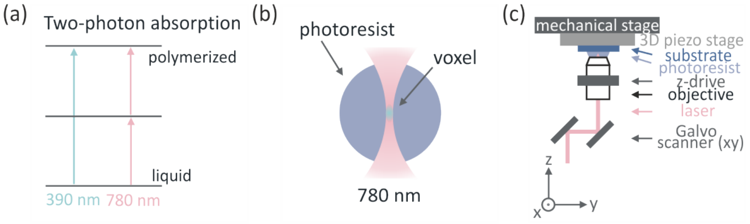

Figure 3.14. Concept of direct laser writing: (a) Scheme of two-photon absorption. (b) Scheme of a voxel. (c) Scheme of the 3D-printer.

4

CUPROUS OXIDE CRYSTAL PREPARATION

In order to be able to detect excitons in cuprous oxide, the crystals need to be prepared in a special manner. The different steps, such as orienting, slicing, polishing, structuring, and mounting the crystal, are described in this chapter.

4.1 CRYSTAL ORIENTATION

Depending on the crystal orientation with respect to the incident light field, optical transitions to different exciton states are allowed or forbidden. By knowing the crystal orientation and the incident light configuration, one can predict, which excitons are in principle excitable in the experiment.

The cuprite crystals are oriented via the Laue backscattering method. We use a Siemens Röntgen generator with a Wolfram tube and use its Brems-spectrum at 20 kV (30 mA) with 30 s exposure time. The resulting white Röntgen light hits the crystal, which is mounted onto a goniometer at 40 mm distance to the 0.5 mm aperture. This way, the resulting scattering points of the low-idexed planes appear on a memory sheet placed opposite to the crystal. Upon illumination with red laser light, the memory sheet is phosphorescencing. The readout is done by a scanner (CR35NDT by Dürr) and sent to a computer. Using *Corel Draw* software image distortions are corrected. With *Orient express* software, the scattering points are read out. Knowing the lattice constant, the corresponding planes of orientation can be assigned. These are shown in a Laue simulation (Fig. 4.1 (a)), as well as in a stereoscopic view of the Wulf net (angle-conserving projection, see Fig. 4.1 (b)).

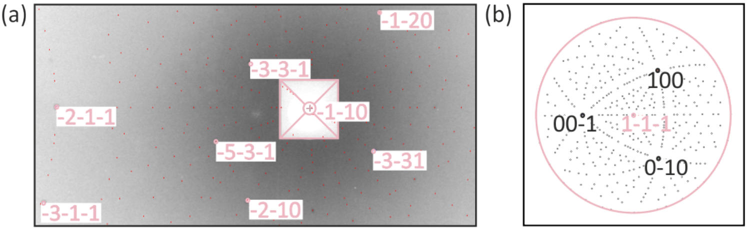

FIGURE 4.1. Laue simulation (a) and stereoscopic view of the Wulf net (b) for crystal plane determination after Laue backscattering.

4.2 CRYSTAL SLICING AND POLISHING

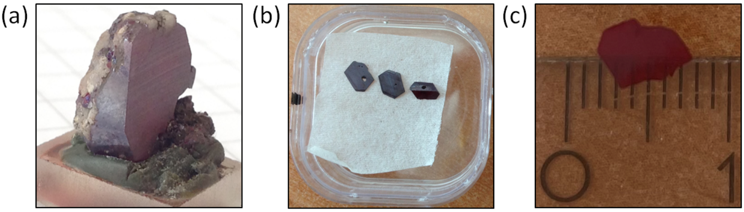

FIGURE 4.2. (a) Natural bulk cuprite crystal prepared for slicing. (b) 300 µm thick cuprous oxide slices in a box with 3.5 cm length. (c) 33 µm thin, polished cuprous oxide flake.

It is of utmost importance to avoid strain inside the crystal during its processing. Strain not only alters the crystal symmetry and, thus, the dipole selection rules, which results in modified absorption spectra, but also hinders the formation of excitons. From the oriented bulk crystals (see Fig. 4.2 (a)) slices of 200 to 300 µm are cut along chosen directions using a sawing machine with a 30 µm wire (see Fig. 4.2 (b)). The slices should not be thinner than 200 µm in order to avoid frequent slipping-off of the sawing wire.

This would result in steps in the cutting facet and additional strain inside the crystal. Cuprous oxide is strongly absorbing light in the visible. This coincides with the energy region, in which excitons are excited. Therefore, the cuprite crystals need to be thinner than 100 µm in order to be able to record absorption spectra in transmission configuration. For achieving such thin crystal flakes, different methods, including etching, as well as wet and dry polishing, have been tested.

4.2.1 *Etching*

In literature we find different methods for etching cuprous oxide. Using ammonia solution (NH_4OH) comes along with an altered surface morphology with greater roughness or even a change in surface facets. The crystal plane exposed on $\mathrm{Cu_2O}$ nanocrystals, strongly influences the etching process. For electrodeposited $\mathrm{Cu_2O}$ films, the ammonia etchant has been found to preferentially interact with the {100} facets and expose a greater number of {111} facets in $\mathrm{Cu_2O}$ [159], while for $\mathrm{Cu_2O}$ nanocrystals the chemical stability is largest for {100} (cubic) surface and decreases for {111} octahedral towards {110} rhombic dodecahedral surfaces [160]. The same holds for etching in acetic acid solution [161] (see Fig. 4.3). Moreover, NaOH completely converts $\mathrm{Cu_2O}$ nanoparticles into CuO nanoparticles after etching in aquaeous solution for 20 min [162]. When etching with 0.01 M oxalic acid ($C_2H_2O_4$) or 0.1 M triethylamine (TEA) there is no compositional change of $\mathrm{Cu_2O}$ nanoparticles but a shape evolution towards ill-defined cubes with rough surfaces. Hence, etching the cuprous oxide slices will not give us a smooth surface.

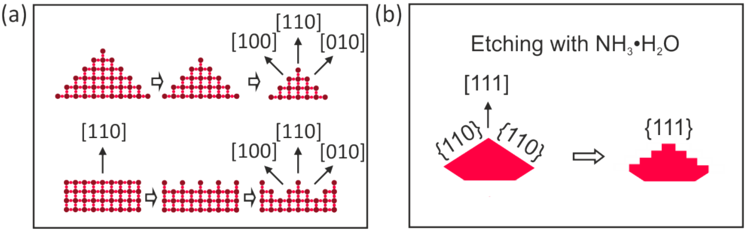

Figure 4.3. (a) Two etching scenarios for cuprous oxide with acid solution. Adapted from [161]. Dark red dots represent oxygen atoms, bright red dots are copper. (b) Preferential etching facets for cuprous oxide according to [159] and the resulting nano-structured facets after etching with $NH_3 \cdot H_2O$.

4.2.2 *Wet and dry polishing*

Wet polishing with aluminum oxide microparticles (diameter 5 µm and 1 µm, from Pieplow & Brandt GmbH) in combination with water is a good way to obtain in a well-controlled manner stepwise thinner crystal flakes with smooth facets. However, due to the hardness of water, small holes are torn into the crystal during polishing. This can be circumvented by replacing water by glycerine. Even smoother surfaces can be achieved by additionally dry-polishing the crystal flakes using 1 µm aluminum oxide and 0.3 µm calcined alumina lapping sheets (Thorlabs GmbH). This way, 30 to 100 µm thin samples with a smoothness of $Sq_{\mathrm{rms}} < 0.3\,\mu\mathrm{m}$ and shiny appearance without major scratches are obtained (see Fig. 4.2 (c)). The thickness is measured using a mechanical thickness measuring gauge as well as the *µscan* technology by NanoFocus AG. The latter one is also used to determine the sample roughness, defined as Sq_{rms} parameter for the root mean square height of the surface (see Fig. 4.4). The importance of a well polished crystal can be seen in Fig. 4.5. For a poorly polished crystal, the exciton peaks are less pronounced and tend to split up.

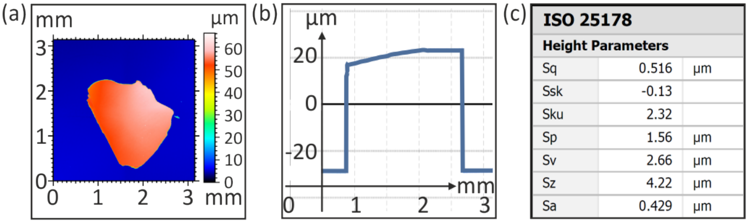

ISO 25178		
Height Parameters		
Sq	0.516	µm
Ssk	-0.13	
Sku	2.32	
Sp	1.56	µm
Sv	2.66	µm
Sz	4.22	µm
Sa	0.429	µm

FIGURE 4.4. 3D surface scan (a), 2D profile (b), and height parameters (c) of a polished cuprous oxide flake measured using the *µscan* technology by NanoFocus AG.

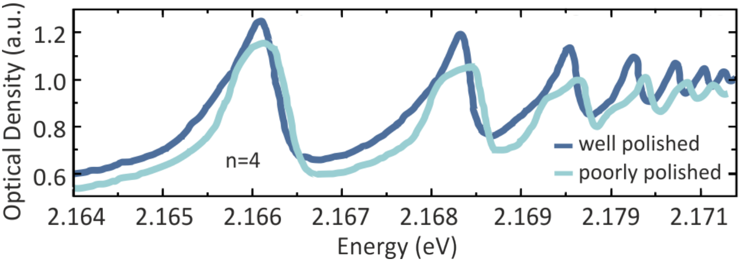

FIGURE 4.5. Exciton spectrum comparison of a well and a poorly polished cuprous oxide crystal flake.

Besides polishing crystal flakes in our own lab with the above mentioned method, some samples were polished by Gabriele Untereiner at the 1st Physics Institute at the University of Stuttgart. She used calcined aluminum lapping sheets by Thorlabs GmbH with 0.3 µm particle size as well as diamond lapping sheets by 3M company with 0.5 µm and 0.1 µm particle sizes. The crystals were dry-polished on the lapping sheets along one defined direction only. Hereby, after polishing with the very fine 0.1 µm lapping sheet, a more coarsely-grained lapping sheet was used for final polish in order to achieve the best polishing result.

Other samples were polished by Dirk Schemionek from the *Präparationslabor* of the Technical University in Dortmund. He mounted the crystal slices onto a sample holder using the resin Alco Wachs 5402 SL by Logitech. The sample holder's weight was adjusted according to the sample, not to exceed 100 g per 1 cm^2 sample surface. The sample was then polished on a lapping wheel made of cast iron using an aqueous suspension with 9 µm Al_2O_3 particles (60 g/l by Logitech) until the correct thickness was reached. In order to control erosion and sample thickness, measuring probes by Mitotoyo (Digmatic, 0-30 mm, 0.001 mm resolution) were used. In addition, the surface was monitored frequently by a microscope. The procedure was repeated with 3 µm Al_2O_3 particles. A thickness of at least three times the particle size of the previous step (~ 30 µm) was removed. Afterwards the samples were polished using a polishing cloth made of polyurethane in combination with colloidal silica suspension. Again, a three-times larger amount of sample surface than the previous particle size was removed (~ 10 µm) in order to obtain a strain-free sample. The silica suspension is added onto the lapping wheel using a peristaltic pump (ISMATEC Reglo Analog ISM827). The suspension must not dry out, as the dry particles cause scratches in the sample. Therefore water was continuously added to the edges of the polishing wheel. Erosion and sample thickness were monitored with measuring probes and microscope. After removing the sample from the lapping sheet, it was detached from the sample holder and placed into a bath of 2-propanol and toluene at 70 °C in order to remove the adherent resin.

4.3 CRYSTAL STRUCTURING

The polished crystals used in this thesis are further structured in one of the three following ways:

1. Aluminum nanoantennas are imprinted directly onto the crystal surface using lithography technique. See Section 3.7.1 for more information.

2. Quantum wells are milled into the crystal surface using focused ion beam milling. This technique is described in detail in Section 3.7.2.

3. Optical phase plates and fiber chucks are written directly onto the crystal surface using direct laser writing. A detailed description can be found in Section 3.7.3.

4.4 CRYSTAL MOUNTING

Strainfree mounting of the Cu_2O crystals is crucial for spectroscopic investigations at ultra-low temperatures. Strain appears during temperature changes if different materials are attached to each other. It will in particular modify the symmetry properties of cuprous oxide. Therefore, special sample holders have been developed. The crystal is placed inside an aluminum foil mask that is slightly thicker than the crystal itself. A top and a bottom mounting plate are then screwed together, pressing only against the aluminum foil, while the cuprite crystal is enclosed strain-free. Top and bottom mounting plates feature a hole in their center so that the crystal surface can be accessed optically. A schematic drawing as well as a photograph picture of a mounted crystal flake are shown in Fig. 4.6.

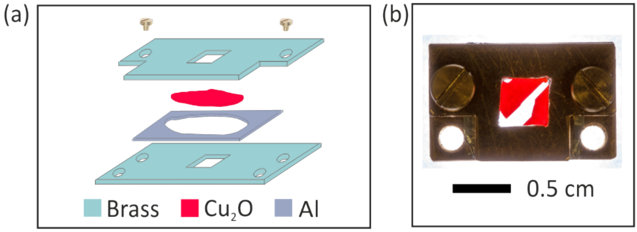

FIGURE 4.6. (a) Schematic drawing of the mounting procedure of a cuprous oxide flake into a sample holder. (b) Photograph picture of a mounted cuprous oxide flake.

4.5 SAMPLE OVERVIEW

Different crystals have been used throughout this thesis. The facets of the different crystal slices are all oriented along {110}. The crystals stem all from mines in Africa and are between 30 and 100 µm thick. They feature OAM plates or antenna fields and are measurend in pure transmission or pure reflection spectroscopy (Setup A), or pump-probe spectroscopy in transmission (Setup B) or reflection (Setup C) geometry. Details are listed in Table 4.1.

Name	Origin	Thickness (µm)	Features	Setup
Sample 0	Namibia	80-100	OAM plate	Setup A (Fig. 3.8)
Sample 1	Namibia	46	Antenna (F5), Reference	Setup A (Fig. 3.8)
Sample 2	Kongo	55-75	Antenna (I3)	Setup B (Fig. 3.9)
Sample 3	Namibia	104	Antenna (F1-F4), Reference	Setup C (Fig. 3.10)
Sample 4	Namibia	32	Antenna (F1-F4) Reference	Setup C (Fig. 3.10)

TABLE 4.1. Overview over the samples used for measurements in this thesis.

5

RYDBERG EXCITONS IN CUPROUS OXIDE: MODIFYING DIPOLE SELECTION RULES USING ORBITAL ANGULAR MOMENTUM LIGHT

Atomic transitions can be driven if the overlap of ground and excited state contains the symmetry of the corresponding light excitation. The complete interaction between light and matter is described by a multipole expansion of the electromagnetic field coupled with the different moments of the atomic charge distribution. While the electric dipole moment $\boldsymbol{d}$ couples with the electric field amplitude $\boldsymbol{E}$ as $\boldsymbol{d} \cdot \boldsymbol{E}$, the quadrupole transition moment Q interacts with the next multipole moment of the field proportional to the field gradient, $Q\nabla\boldsymbol{E}$. An electric dipole transition requires a change of total angular momentum $\Delta j = 1$, whereas an electric quadrupole transitions requires a change of two units of angular momentum, $\Delta j = 2$.

Usually, optical beams have a longitudinal field gradient, which allows for driving electric quadrupole transitions, however, with a strength of three orders of magnitude weaker than the electric dipole transition. A transverse field gradient due to the spatial structure of the beam front, such as in orbital angular momentum (OAM) light, can drive quadrupole transitions, too [119, 120, 122, 123, 163, 164]. However, to make these quadrupole transitions similar in magnitude to standard electric dipole transitions, an atom usually has to be placed precisely (no further displaced than the atomic distance a_0) in the light field center, and the probe beam has to be focused close to the diffraction limit [118].

Rydberg excitons in cuprous oxide (Cu_2O, cuprit) exist with different envelope functions (S, P, D,...), given by their OAM quantum number l^{exc} (see Fig. 5.1). These envelope functions exhibit different symmetry properties (Γ_1^+, Γ_4^-, $\Gamma_3^+ + \Gamma_5^+$, ...), thus, only parts of them (P- and F-excitons) are allowed transitions for excitation with dipolar light. Mesoscopic Rydberg excitons with sizes in the µm-region match the size of a focused OAM beam. Hence, the realization of enhanced quadrupole transitions (S- and D-excitons) in cuprous oxide Rydberg excitons triggered by the transverse field gradient in the center of an OAM beam should be realizable in experiment [165].

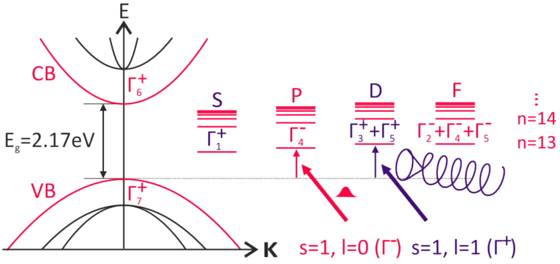

FIGURE 5.1. Formation of exciton series between the highest valence (VB) and the lowest conduction (CB) band in cuprous oxide. Depending on the amount of angular momentum l of the exciting light field, Rydberg series with different envelope functions (S, P, D, F) become allowed transitions.

In this chapter, we show how to modify the selection rules for Rydberg excitons in cuprous oxide by tuning the properties of the exciting light, in particular, by adding angular momentum to the light. In Section 5.1 we evaluate by symmetry considerations, that the transition selection rules can be modified. One-photon-forbidden transitions become allowed transitions, as the spatial mode of the OAM light is transferred to the exciton state due to phase (angular momentum) conservation. In Section 5.2 we discuss corresponding experimental results, and in Section 5.3 we give a conclusion and an outlook on OAM light in combination with Rydberg excitons.

5.1 THEORETICAL INVESTIGATIONS

This section is based on the following publication [45]:
A. Konzelmann, S.-O. Krüger, and H. Giessen, *Interaction of orbital angular momentum light with Rydberg excitons: Modifying dipole selection rules*, Phys. Rev. B **100**, 115308 (2019).

Our aim is to predict whether optical transitions between the cuprite crystal ground state and exciton states with different OAM quantum numbers l^{exc} are allowed or forbidden when exciting with OAM light ($l = 0, 1, 2, 3$). Using symmetry considerations from group theory we know that for allowed transitions the overlap of crystal ground state and excited state contains the symmetry of the exciting light, i.e., the optical transition driving operator $\boldsymbol{A} \cdot \boldsymbol{p}$. The questions to be answered are:

1. What symmetry do excitons with different OAM quantum number l^{exc} obey in cuprous oxide?
2. How does OAM light behave under the symmetry conditions imposed by the Cu_2O crystal?

The symmetries of the excitonic states are derived from the cuprous oxide band symmetries. The OAM light symmetries must be determined with respect to the symmetry group of cuprous oxide O_h, as the excitation takes place inside the crystal.
First, we consider the coordinate functions of OAM light and excitons, and investigate how they change when undergoing O_h symmetry operations. The fundamental coordinates are understood as basis functions for the irreducible representation within the corresponding point group. Second, we derive a reducible representation and decompose it into irreducible representations, which gives the total symmetry. Third, we compare the symmetries of OAM light and excitons. The calculations are performed with help of the tables by Koster [88].

5.1.1 *Symmetries of orbital angular momentum light*

The properties of orbital angular momentum light have already been discussed in Section 2.4. We will shortly examine the mode structure again under the aspect of transition matrix elements, and then lay focus onto its symmetry properties.

The complete OAM light field is described by a Laguerre-Gauss mode, which is a Gaussian beam times an additional phase factor $e^{il\varphi}$. It has the form:

$$A_{lp}\left(r,\varphi,z\right) = A_0 e^{ikz}\frac{w_0}{w} exp\left[\frac{-r^2}{w^2} + \frac{ikr^2}{2R} - i\left(2p+|l|+1\right)\phi\left(z\right)\right] \times \left(\frac{\sqrt{2}r}{w}\right)^{|l|} L_p^{|l|}\left(\frac{2r^2}{w^2}\right) e^{il\varphi}, \tag{5.1}$$

with light field amplitude A_0, wave vector k, beam waist $w\left(z\right)$, $w_0 = w\left(z=0\right)$, Gouy phase $\phi\left(z\right)$, radius of curvature $R\left(z\right)$, and generalized Laguerre polynomial $L_p^{|l|}$.

Usually, the extension of an atom's wavepacket is much smaller than the wavelength of the interacting light: $a_0 \ll \lambda$. Therefore, $r \ll w_0$, and one can approximate at $z = z_0$:

$$A_{00} = A_0 e^{ikz} exp\left[\frac{-r^2}{w^2} + \frac{ikr^2}{2R} - i\phi\left(z_0\right)\right] \approx A_0\left(1+ikz\right), \tag{5.2}$$

with A_0 being responsible for dipole transitions, and $A_0 ikz$ for quadrupole transitions. Even by increasing the power of the interacting laser or focusing down to a small waist size in order to increase A_0, the standard electric quadrupole excitation remains very weak.

Treating OAM light with one amount of orbital angular momentum $l = 1$, gives as leading term in the vector potential:

$$\boldsymbol{A}_{10} \approx \boldsymbol{A}_0 \frac{\sqrt{2}r}{w_0} e^{i\varphi}. \tag{5.3}$$

Here, directly the spatial coordinate r appears, implying that dipole-forbidden (quadrupole) transitions are now allowed transitions.

The exact transition probabilities from an initial $|i\rangle$ to a final $|f\rangle$ state,

$$w_{if} \propto \frac{2\pi}{\hbar} \langle f|\boldsymbol{A} \cdot \boldsymbol{p}|i\rangle \rho_f, \tag{5.4}$$

with ρ_f being the density of final states, can be calculated analytically via Fermi's golden rule [118]. This includes to write the interaction Hamiltonian in terms of products of the spherical tensors. These are then rewritten as a sum of spherical tensors using the Clebsh-Gordan coefficients. After rotation of the different states to obey the same basis, the Wigner-Eckart theorem is used to calculate the relative weight of each term in the total transition probability. This elaborate procedure of calculating transition matrix elements can, however, be avoided by performing symmetry considerations.

We are going to assign a symmetry to the (different factors of the) optical transition driving operator $\boldsymbol{A} \cdot \boldsymbol{p}$ for OAM light modes with different amounts of OAM l. We consider only OAM light propagating in z direction. The exciton is assumed to be located in the vortex center in the xy plane, so the overall symmetry is maintained and the r dependence of the mode does not influence the transformational properties. We develop the light field in z. In dipole approximation the Gaussian beam part simplifies to $\boldsymbol{A}_0 e^{ikz} \approx \boldsymbol{A}_0 \left(1 + ikz\right) \approx \boldsymbol{A}_0$. From the OAM part, the only relevant factor for symmetry considerations is $e^{il\varphi}$. Then, the optical transition driving operator becomes:

$$\boldsymbol{A} \cdot \boldsymbol{p} = e^{il\varphi} \boldsymbol{A}_0 \cdot \boldsymbol{p}. \tag{5.5}$$

The symmetries of $\boldsymbol{A}_0$ and $\boldsymbol{p}$ with respect to group O_h are $\varGamma_1^+$ and $\varGamma_4^-$, respectively. The function $e^{il\varphi}$ is cylindrically symmetric and can be aligned along the three coordinate axes in the cubic cuprite crystal. We choose the six linearly independent basis functions

$$e^{+il\varphi_x},\ e^{-il\varphi_x},\ e^{+il\varphi_y},\ e^{-il\varphi_y},\ e^{+il\varphi_z},\ e^{-il\varphi_z}, \tag{5.6}$$

into which $e^{il\varphi}$ can be transformed under the symmetry operations of point group O_h.

The case $l = 0$, i.e. the dipolar light field, is considered separately. For $e^{i\left(l=0\right)\varphi} = 1$ we cannot find six linear independent basis functions. In this case, the symmetry is directly assigned to $\varGamma_1^+$.

For $l = 1$ we write the phase factor in Cartesian coordinates:

$$e^{i\left(l=1\right)\varphi} = \frac{1}{\sqrt{x^2 + y^2}} \left(x + iy\right). \tag{5.7}$$

In order to assign a symmetry to OAM light, we go through the following steps:

1. We analyze how the coordinates x, y, z change under symmetry operations of O_h. We repeat the analysis for the functions $x + iy$, $y + iz$, $z + ix$ and $\frac{1}{\sqrt{x^2+y^2}}$, $\frac{1}{\sqrt{z^2+y^2}}$, $\frac{1}{\sqrt{x^2+z^2}}$. The results can then immediately be generalized to all six basis functions for arbitrary l, $e^{il\varphi}$.

2. We decompose the resulting functions into basis functions in order to calculate the trace of the transformation matrix, also known as characters.
3. We multiply the characters of the different functions in order to get a character set for the light field operators. Last, we assign symmetries to the complete set of characters according to the character tables of group O_h.

1. Symmetry operations on coordinates and functions

A coordinate transformation of order n leads to the original coordinate after performing the transformation n times, i.e., three times for the eight threefold symmetry axes $8C_3$ of group O_h:

$$x \longrightarrow y \longrightarrow z \longrightarrow x. \tag{5.8}$$

It suffices to select one element per class, i.e., axis (111) in class $8C_3$, as all elements of the same class transform the same way. In contrast, it is important to perform the symmetry considerations for a complete basis, i.e., x, y, and z, in order to extract the character of a transformation (trace of transformation matrix).
The complete transformations of the coordinates x, y, z under symmetry operations $\hat{O}$ of group O_h are listed in Table 5.1. Knowing how the coordinates behave under the different symmetry operations, one can write down the transformations of the basis functions of $e^{il\varphi}$ (see Table 5.2).

TABLE 5.1. Coordinate transformations under O_h symmetry operations.

$\hat{O}$	**Vector**	x	y	z
E		$x \to x$	$y \to y$	$z \to z$
$8C_3$	(111)	$x \to y \to z \to x$	$y \to z \to x \to y$	$z \to x \to y \to z$
	(-1-1-1)	$x \to z \to y \to x$	$y \to x \to z \to y$	$z \to y \to x \to z$
	(-111)	$x \to -z \to -y \to x$	$y \to -x \to z \to y$	$z \to y \to -x \to z$
	(1-1-1)	$x \to z \to y \to x$	$y \to z \to -x \to y$	$z \to -x \to y \to z$
	(1-11)	$x \to -y \to z \to x$	$y \to -z \to -x \to y$	$z \to x \to -y \to z$
	(-11-1)	$x \to z \to -y \to x$	$y \to -x \to -z \to y$	$z \to -y \to x \to z$
	(11-1)	$x \to -z \to -y \to x$	$y \to x \to -z \to y$	$z \to -y \to -x \to z$
	(-1-11)	$x \to -y \to -z \to x$	$y \to -z \to x \to y$	$z \to -x \to -y \to z$
$3C_2$	(100)	$x \to x \to x$	$y \to -y \to y$	$z \to -z \to z$
	(010)	$x \to -x \to x$	$y \to y \to y$	$z \to -z \to z$
	(001)	$x \to -x \to x$	$y \to -y \to y$	$z \to z \to z$
$6C_4$	X	$x \to x \to x \to x \to x$	$y \to -z \to -y \to z \to y$	$z \to y \to -z \to -y \to z$
	-X	$x \to x \to x \to x \to x$	$y \to z \to -y \to -z \to y$	$z \to -y \to -z \to y \to z$
	Y	$x \to z \to -x \to -z \to x$	$y \to y \to y \to y \to y$	$z \to -x \to -z \to x \to z$
	-Y	$x \to -z \to -x \to z \to x$	$y \to y \to y \to y \to y$	$z \to x \to -z \to -x \to z$
	Z	$x \to -y \to -x \to y \to x$	$y \to x \to -y \to -x \to y$	$z \to z \to z \to z \to z$
	-Z	$x \to y \to -x \to -y \to x$	$y \to -x \to -y \to x \to y$	$z \to z \to z \to z \to z$
$6C_2'$	(110)	$x \to y \to x$	$y \to x \to y$	$z \to -z \to z$
	(1-10)	$x \to -y \to x$	$y \to -x \to y$	$z \to -z \to z$
	(101)	$x \to z \to x$	$y \to y \to y$	$z \to x \to z$
	(10-1)	$x \to -z \to x$	$y \to -y \to y$	$z \to -x \to z$
	(011)	$x \to -x \to x$	$y \to z \to y$	$z \to y \to z$
	(01-1)	$x \to -x \to x$	$y \to -z \to y$	$z \to -y \to z$

TABLE 5.2. Transformations of functions $e^{\pm il\varphi_x}$, $e^{\pm il\varphi_y}$, and $e^{\pm il\varphi_z}$ under O_h symmetry operations.

Operator $\hat{O}$	$\hat{O}\lvert e^{\pm il\varphi_x}\rangle$	$\hat{O}\lvert e^{\pm il\varphi_y}\rangle$	$\hat{O}\lvert e^{\pm il\varphi_z}\rangle$
E	$e^{\pm il\varphi_x}$	$e^{\pm il\varphi_y}$	$e^{\pm il\varphi_z}$
$8C_3$	$e^{\pm il\varphi_z}$	$e^{\pm il\varphi_x}$	$e^{\pm il\varphi_y}$
$3C_2$	$e^{\pm il\left(\varphi_x+\pi\right)}$	$e^{\mp il\left(\varphi_y+\pi\right)}$	$e^{\mp il\varphi_z}$
$6C_4$	$e^{\pm il\left(\varphi_x+\pi/2\right)}$	$e^{\mp il\left(\varphi_z\pm\pi/2\right)}$	$e^{\pm il\left(\varphi_y\mp\pi/2\right)}$
$6C_2'$	$e^{\pm il\left(\varphi_y-\pi/2\right)}$	$e^{\pm il\left(\varphi_x+\pi/2\right)}$	$e^{\mp il\left(\varphi_z-\pi/2\right)}$

TABLE 5.3. Matrix elements of the transformation matrices $\hat{O}|f_i\rangle = \sum_k N_{i,k}|f_k\rangle$ and their common characters for OAM light ($e^{il\varphi}$) with arbitrary amount of angular momentum l as well as character sets for OAM light field operator $\boldsymbol{A} = \boldsymbol{A}_0 e^{il\varphi}$ and OAM first-class ($\boldsymbol{A} \cdot \boldsymbol{p} = e^{il\varphi} \boldsymbol{A}_0 \cdot \boldsymbol{p}$) and second-class ($\boldsymbol{A} \cdot \boldsymbol{p} = ikze^{il\varphi} \boldsymbol{A}_0 \cdot \boldsymbol{p}$) transition driving operator.

	O_h	E	$8C_3$	$3C_2$	$6C_4$	$6C_2'$	I	$8S_6$	$3\sigma_h$	$6S_4$	$6\sigma_d$
I	$e^{+il\varphi_x}$	1	0	$e^{+il\pi}$	$e^{+il\pi/2}$	0	$e^{+il\pi}$	0	1	$e^{+il\pi/2}$	0
	$e^{-il\varphi_x}$	1	0	$e^{+il\pi}$	$e^{+il\pi/2}$	0	$e^{+il\pi}$	0	1	$e^{+il\pi/2}$	0
	$e^{+il\varphi_y}$	1	0	0	0	0	$e^{+il\pi}$	0	0	0	0
	$e^{-il\varphi_y}$	1	0	0	0	0	$e^{+il\pi}$	0	0	0	0
	$e^{+il\varphi_z}$	1	0	0	0	0	$e^{+il\pi}$	0	0	0	0
	$e^{-il\varphi_z}$	1	0	0	0	0	$e^{+il\pi}$	0	0	0	0
	$e^{il\varphi}$ (Sum)	6	0	$2\,(-1)^l$	$2\cos\left(l\pi/2\right)$	0	$6\,(-1)^l$	0	2	$2\cos\left(l\pi/2\right)$	0
II	$\boldsymbol{A}_0$	1	1	1	1	1	1	1	1	1	1
	$\boldsymbol{A} = \boldsymbol{A}_0 \cdot e^{il\varphi}$	6	0	$2\,(-1)^l$	$2\cos\left(l\pi/2\right)$	0	$6\,(-1)^l$	0	2	$2\cos\left(l\pi/2\right)$	0
	$l = 1$	6	0	-2	0	0	-6	0	2	0	0
	$l = 2$	6	0	2	-2	0	6	0	2	-2	0
	$l = 3$	6	0	-2	0	0	-6	0	2	0	0
III	$\boldsymbol{p}$	3	0	-1	0	-1	-3	0	1	-1	1
	$\boldsymbol{A} \cdot \boldsymbol{p}$ (first class)	18	0	$-2\,(-1)^l$	$2\cos\left(l\pi/2\right)$	0	$-18\,(-1)^l$	0	2	$-2\cos\left(l\pi/2\right)$	0
	$l = 1$	18	0	2	0	0	18	0	2	0	0
	$l = 2$	18	0	-2	-2	0	-18	0	2	2	0
	$l = 3$	18	0	2	0	0	-18	0	2	0	0
IV	$\boldsymbol{z}$	3	0	-1	1	-1	-3	0	1	-1	1
	$\boldsymbol{A} \cdot \boldsymbol{p}$ (second class)	54	0	$2\,(-1)^l$	$2\cos\left(l\pi/2\right)$	0	$54\,(-1)^l$	0	2	$2\cos\left(l\pi/2\right)$	0
	$l = 1$	54	0	-2	0	0	-54	0	2	0	0
	$l = 2$	54	0	2	-2	0	54	0	2	-2	0
	$l = 3$	54	0	-2	0	0	-54	0	2	0	0

2. Decomposition into basis functions and calculation of characters

In order to calculate the transformation matrix diagonal elements, the transformed functions $\hat{O}|f_i\rangle$ are decomposed into basis vectors $|f_k\rangle$ according to:

$$\hat{O}|f_i\rangle = \sum_k N_{i,k}|f_k\rangle. \tag{5.9}$$

The characters of the OAM light for each symmetry class are then given by the sum of the results $N_{k,k}$ of all six basis vectors, i.e., the trace:

$$\chi\left(\hat{O}\right) = Tr\left(N_{i,k}\right) = \sum_k N_{k,k}. \tag{5.10}$$

The single transformation matrix diagonal elements $N_{k,k}$ for one representative class element of all symmetry classes of group O_h, as well as the resulting character set $\sum_k N_{k,k}$ for different OAM light ($e^{il\varphi}$) are listed in part I in Table 5.3.

3. Character multiplication and symmetry assignment

Table 5.4. Character set for OAM light field operator ($\boldsymbol{A} = \boldsymbol{A}_0 e^{il\varphi}$) and first-class ($\boldsymbol{A} \cdot \boldsymbol{p} = e^{il\varphi}\boldsymbol{A}_0 \cdot \boldsymbol{p}$) and second-class ($\boldsymbol{A} \cdot \boldsymbol{p} = ikze^{il\varphi}\boldsymbol{A}_0 \cdot \boldsymbol{p}$) transition driving operator for arbitrary amount of angular momentum l.

O_h	E	$8C_3$	$3C_2$	$6C_4$	$6C_2^1$
$\boldsymbol{A} = \boldsymbol{A}_0 e^{il\varphi}$	6	0	$2\left(-1\right)^l$	$2\cos\left(l\pi/2\right)$	0
$\boldsymbol{A} \cdot \boldsymbol{p}$ (First class)	18	0	$-2\left(-1\right)^l$	$2\cos\left(l\pi/2\right)$	0
$\boldsymbol{A} \cdot \boldsymbol{p}$ (Second class)	54	0	$2\left(-1\right)^l$	$2\cos\left(l\pi/2\right)$	0

Multiplication of the characters of $e^{il\varphi}$ with the ones of $\boldsymbol{A}_0$ yields the character set for the complete OAM light field operator $\boldsymbol{A} = \boldsymbol{A}_0 e^{il\varphi}$. The amplitude $\boldsymbol{A}_0$ is described by symmetry Γ_1^+, which acts like a 1 in multiplication (identity). Further multiplication with the characters for the momentum operator $\boldsymbol{p}$, which is described by symmetry Γ_4^-, yields the characters for the optical transition driving operator $\boldsymbol{A} \cdot \boldsymbol{p}$. The resulting character sets for first- and second-class transitions for an arbitrary amount of orbital angular momentum l are listed in parts II-IV in Table 5.3. They are also shown in Table 5.4 in a clearer way for the first five classes in group O_h only.

Table 5.5 shows the different light field operators for dipole and quadrupole OAM light expressed by a sum of symmetry operators. $l = 1$ and $l = 3$ OAM light exhibit the same symmetry. If the dipolar light field operator is of positive parity, the corresponding quadrupole light field operator is of negative parity and vice versa. For successive increase of OAM l, the parity changes alternatively. The assignment of symmetries is done by using the character table for symmetry group O_h (Table 5.6) [88]. The character sets of the light field operators are compared with the character sets of the symmetry operators $\Gamma_i^\pm$. A linear combination of the symmetry operators then reproduces the light field operator symmetry.

TABLE 5.5. Symmetries of dipole and quadrupole transition driving operator of OAM light with different amounts of OAM l.

OAM l	Dipole	Quadrupole
0 (Even)	Γ_4^-	$\Gamma_3^+ + \Gamma_5^+$
1 (Odd)	$\Gamma_1^+ + \Gamma_2^+ + 2\Gamma_3^+ + 2\Gamma_4^+ + 2\Gamma_5^+$	$\Gamma_1^- + \Gamma_2^- + 2\Gamma_3^- + 4\Gamma_4^- + 4\Gamma_5^-$
2 (Even)	$\Gamma_2^- + \Gamma_3^- + 2\Gamma_4^- + 3\Gamma_5^-$	$2\Gamma_1^+ + \Gamma_2^+ + 3\Gamma_3^+ + 4\Gamma_4^+ + 3\Gamma_5^+$
3 (Odd)	$\Gamma_1^+ + \Gamma_2^+ + 2\Gamma_3^+ + 2\Gamma_4^+ + 2\Gamma_5^+$	$\Gamma_1^- + \Gamma_2^- + 2\Gamma_3^- + 4\Gamma_4^- + 4\Gamma_5^-$
4 (Even)	$\Gamma_1^- + \Gamma_3^- + 3\Gamma_4^- + 2\Gamma_5^-$	$\Gamma_1^+ + 2\Gamma_2^+ + 3\Gamma_3^+ + 3\Gamma_4^+ + 4\Gamma_5^+$

TABLE 5.6. Character table and basis functions for point group O_h [88].

O_h	E	$8C_3$	$3C_2$	$6C_4$	$6C_2'$	I	$8S_6$	$3\sigma_h$	$6S_4$	$6\sigma_d$	Bases
Γ_1^+	1	1	1	1	1	1	1	1	1	1	R
Γ_2^+	1	1	1	-1	-1	1	1	1	-1	-1	$\left(x^2-y^2\right)\left(y^2-z^2\right)\left(z^2-x^2\right)$
Γ_3^+	2	-1	2	0	0	2	-1	2	0	0	$\left(2z^2-x^2-y^2\right), \sqrt{3}\left(x^2-y^2\right)$
Γ_4^+	3	0	-1	1	-1	3	0	-1	1	-1	$S_x, S_y\ S_z$
Γ_5^+	3	0	-1	-1	1	3	0	-1	-1	1	yz, xz, xy
Γ_1^-	1	1	1	1	1	-1	-1	-1	-1	-1	$\Gamma_2^- \times \Gamma_2^+$
Γ_2^-	1	1	1	-1	-1	-1	-1	-1	1	1	xyz
Γ_3^-	2	-1	2	0	0	-2	1	-2	0	0	$\Gamma_3^+ \times \Gamma_2^-$
Γ_4^-	3	0	-1	1	-1	-3	0	1	-1	1	x, y, z
Γ_5^-	3	0	-1	-1	1	-3	0	-1	-1	-1	$\Gamma_5^+ \times \Gamma_1^-$
Γ_6^+	2	1	0	$\sqrt{2}$	0	2	1	0	$\sqrt{2}$	0	$\phi\left(1/2,-1/2\right), \phi\left(1/2,1/2\right)$
Γ_7^+	2	1	0	$-\sqrt{2}$	0	2	1	0	$-\sqrt{2}$	0	$\Gamma_6^+ \times \Gamma_2^+$
Γ_8^+	4	-1	0	0	0	4	-1	0	0	0	$\phi\left(3/2,-3/2\right), \phi\left(3/2,-1/2\right), \phi\left(3/2,1/2\right), \phi\left(3/2,3/2\right)$
Γ_6^-	2	1	0	$\sqrt{2}$	0	-2	-1	0	$-\sqrt{2}$	0	$\Gamma_6^+ \times \Gamma_1^-$
Γ_7^-	2	1	0	$-\sqrt{2}$	0	-2	-1	0	$\sqrt{2}$	0	$\Gamma_6^+ \times \Gamma_2^-$
Γ_8^-	4	-1	0	0	0	-4	1	0	0	0	$\Gamma_8^+ \times \Gamma_1^-$

5.1.2 *Cuprous oxide symmetries*

The symmetries of Rydberg excitons in cuprous oxide are composed of the cuprous oxide valence and conduction band symmetries, Γ_V and Γ_C, respectively (see Section 2.2.2), as well as the exciton envelope symmetry $\Gamma_{\text{env}}^{l_{\text{exc}}}$:

$$\Gamma_{\text{exc}} = \Gamma_{\text{V}} \times \Gamma_{\text{C}} \times \Gamma_{\text{env}}^{l_{\text{exc}}} = \Gamma_7^+ \times \Gamma_6^+ \times \Gamma_{\text{env}}^{l_{\text{exc}}} = \left(\Gamma_2^+ + \Gamma_5^+\right) \times \Gamma_{\text{env}}^{l_{\text{exc}}} . \tag{5.11}$$

Symmetry multiplication is performed according to the multiplications rules given by the multiplication table for point group O_h in Table 5.7. The exciton envelope functions are described by spherical harmonics functions Y_l^m. These are listed in Table 5.8 in Cartesian coordinates for S-, P-, D-, and F-excitons.

TABLE 5.7. Multiplication table for point group O_h. Parity is taken into account via $\Gamma^\pm \times \Gamma^\pm = \Gamma^+$ and $\Gamma^\pm \times \Gamma^\mp = \Gamma^-$.

Γ_1	Γ_2	Γ_3	Γ_4	Γ_5	Γ_6	Γ_7	Γ_8	$\times$
Γ_1	Γ_2	Γ_3	Γ_4	Γ_5	Γ_6	Γ_7	Γ_8	Γ_1
	Γ_1	Γ_3	Γ_5	Γ_4	Γ_7	Γ_6	Γ_8	Γ_2
		$\Gamma_1+\Gamma_2$ $+\Gamma_3$	$\Gamma_4+\Gamma_5$	$\Gamma_4+\Gamma_5$	Γ_8	Γ_8	$\Gamma_6+\Gamma_7+\Gamma_8$	Γ_3
			$\Gamma_1+\Gamma_3$ $+\Gamma_4+\Gamma_5$	$\Gamma_2+\Gamma_3$ $+\Gamma_4+\Gamma_5$	$\Gamma_6+\Gamma_8$	$\Gamma_7+\Gamma_8$	$\Gamma_6+\Gamma_7+2\Gamma_8$	Γ_4
				$\Gamma_1+\Gamma_3$ $+\Gamma_4+\Gamma_5$	$\Gamma_7+\Gamma_8$	$\Gamma_6+\Gamma_8$	$\Gamma_6+\Gamma_7+2\Gamma_8$	Γ_5
					$\Gamma_1+\Gamma_4$	$\Gamma_2+\Gamma_5$	$\Gamma_3+\Gamma_4+2\Gamma_5$	Γ_6
						$\Gamma_1+\Gamma_4$	$\Gamma_3+\Gamma_4+2\Gamma_5$	Γ_7
							$\Gamma_1+\Gamma_2+\Gamma_3$ $+2\Gamma_4+2\Gamma_5$	Γ_8

Table 5.8. Spherical harmonics functions Y_l^m in Cartesian coordinates.

S-envelope ($l = 0$):	P-envelope ($l = 1$):
$Y_0^0\left(\vartheta,\varphi\right) = \frac{1}{2}\sqrt{\frac{1}{\pi}}$	$Y_1^{-1}\left(\vartheta,\varphi\right) = \frac{1}{2}\sqrt{\frac{3}{2\pi}}\frac{\left(x-iy\right)}{r}$
F-envelope ($l = 3$):	$Y_1^0\left(\vartheta,\varphi\right) = \frac{1}{2}\sqrt{\frac{3}{\pi}}\frac{z}{r}$
$Y_3^{-3}\left(\vartheta,\varphi\right) = \frac{1}{8}\sqrt{\frac{35}{\pi}}\frac{\left(x-iy\right)^3}{r^3}$	$Y_1^1\left(\vartheta,\varphi\right) = -\frac{1}{2}\sqrt{\frac{3}{2\pi}}\frac{\left(x+iy\right)}{r}$
$Y_3^{-2}\left(\vartheta,\varphi\right) = \frac{1}{4}\sqrt{\frac{105}{2\pi}}\frac{\left(x-iy\right)^2 z}{r^3}$	D-envelope ($l = 2$):
$Y_3^{-1}\left(\vartheta,\varphi\right) = \frac{1}{8}\sqrt{\frac{21}{\pi}}\frac{\left(x-iy\right)\left(4z^2-x^2-y^2\right)}{r^3}$	$Y_2^{-2}\left(\vartheta,\varphi\right) = \frac{1}{4}\sqrt{\frac{15}{2\pi}}\frac{\left(x-iy\right)^2}{r^2}$
$Y_3^0\left(\vartheta,\varphi\right) = \frac{1}{4}\sqrt{\frac{7}{\pi}}\frac{z\left(2z^2-3x^2-3y^2\right)}{r^2}$	$Y_2^{-1}\left(\vartheta,\varphi\right) = \frac{1}{2}\sqrt{\frac{15}{2\pi}}\frac{\left(x-iy\right)z}{r^2}$
$Y_3^1\left(\vartheta,\varphi\right) = -\frac{1}{8}\sqrt{\frac{21}{\pi}}\frac{\left(x+iy\right)\left(4z^2-x^2-y^2\right)}{r^3}$	$Y_2^0\left(\vartheta,\varphi\right) = \frac{1}{4}\sqrt{\frac{5}{\pi}}\frac{2z^2-x^2-y^2}{r^2}$
$Y_3^2\left(\vartheta,\varphi\right) = \frac{1}{4}\sqrt{\frac{105}{2\pi}}\frac{\left(x+iy\right)^2 z}{r^3}$	$Y_2^1\left(\vartheta,\varphi\right) = -\frac{1}{2}\sqrt{\frac{15}{2\pi}}\frac{\left(x+iy\right)z}{r^2}$
$Y_3^3\left(\vartheta,\varphi\right) = -\frac{1}{8}\sqrt{\frac{35}{\pi}}\frac{\left(x+iy\right)^3}{r^3}$	$Y_2^2\left(\vartheta,\varphi\right) = \frac{1}{4}\sqrt{\frac{15}{2\pi}}\frac{\left(x+iy\right)^2}{r^2}$

For symmetry assignment it suffices to use one representative envelope function per orbital l, as different functions of the same orbital belong to the same symmetry group. This means, we choose one magnetic quantum number value m, i.e., Y_0^0 for S-excitons, Y_1^1 for P-excitons,... for symmetry considerations. In the simplest case, the orbital functions are pure basis functions, so their symmetry can be directly assigned according to the character table of point group O_h. The orbital functions are then irreducible representations. This is the case for S and P orbitals:

$$Y_0^0 = 1/\sqrt{4\pi} \sim 1 \tag{5.12a}$$

$$Y_1^1 = \sqrt{3/8\pi}\left(x - iy\right)/r \tag{5.12b}$$

Accordingly, the S orbital transforms as Γ_1^+ and the P orbital transforms as Γ_4^-.

If the bases cannot be seen directly, one has to apply the different symmetry operations of group O_h to the orbital function and decompose them via $N_{m_1,m_2} = \langle Y_l^{m_1}|\hat{O}|Y_l^{m_2}\rangle$. The decomposition of the spherical harmonics in Cartesian coordinates into basis functions yields the complete character sets, which are shown in Table 5.9 [88]. The resulting orbital symmetries, known via comparison of the character sets with the O_h character table, are shown in Table 5.10 together with the complete exciton symmetries for different envelope functions.

TABLE 5.9. Character sets and symmetries of exciton envelope functions.

l^{exc}	E (000)	$8C_3$ (111)	$3C_2$ (100)	$6C_4$ (X)	$6C_2'$ (110)	$\Gamma_{\text{env}}^{l^{\text{exc}}}$
0	1	1	1	1	1	Γ_1^+
1	3	0	-1	1	-1	Γ_4^-
2	5	-1	1	-1	1	$\Gamma_3^+ + \Gamma_5^+$
3	7	1	-1	-1	-1	$\Gamma_2^- + \Gamma_4^- + \Gamma_5^-$

TABLE 5.10. Exciton envelope ($\Gamma_{\text{env}}^{l^{\text{exc}}}$) and exciton total transition (Γ_{exc}) symmetries [5, 24, 166].

Envelope	Exciton envelope symmetry	Exciton total symmetry
S ($l^{\text{exc}} = 0$)	Γ_1^+	$\Gamma_2^+ + \Gamma_5^+$
P ($l^{\text{exc}} = 1$)	Γ_4^-	$\Gamma_2^- + \Gamma_3^- + \Gamma_4^- + 2\Gamma_5^-$
D ($l^{\text{exc}} = 2$)	$\Gamma_3^+ + \Gamma_5^+$	$\Gamma_1^+ + 2\Gamma_3^+ + 3\Gamma_4^+ + \Gamma_5^+$
F ($l^{\text{exc}} = 3$)	$\Gamma_2^- + \Gamma_4^- + \Gamma_5^-$	$2\Gamma_1^- + \Gamma_2^- + 2\Gamma_3^- + 4\Gamma_4^- + 3\Gamma_5^-$
G ($l^{\text{exc}} = 4$)	$\Gamma_1^+ + \Gamma_3^+ + \Gamma_4^+ + \Gamma_5^+$	$\Gamma_1^+ + 2\Gamma_2^+ + 3\Gamma_3^+ + 4\Gamma_4^+ + 5\Gamma_5^+$

5.1.3 *Interaction of OAM light with Rydberg excitons*

When illuminating cuprous oxide with dipolar light ($l = 0$), P-excitons are visible in the absorption spectrum. According to our calculations P-excitons can also become allowed transitions in quadrupole excitation using $l = 1$ or $l = 3$ OAM light. In contrast, the usually dipole-forbidden S-exciton states can not only be driven by the quadrupole field of even OAM light ($l = 0, 2, 4$), but also by dipole transitions with odd OAM light ($l = 1, 3$). The same holds for D- and G-excitons, while F- and H-excitons follow the excitation rules of P-excitons. These results are summarized in Table 5.11.

TABLE 5.11. Exciton total transition symmetries Γ_{exc}, their parity (+/-), and dipole as well as quadrupol light field with different amount of OAM l^{Dipole} / $l^{\text{Quadrupole}}$ (even/odd), which they can be excited with.

Envelope	Γ_{exc}	Parity	l^{Dipole}	$l^{\text{Quadrupole}}$
S	$\Gamma_2^+ + \Gamma_5^+$	+	odd	even
P	$\Gamma_2^- + \Gamma_3^- + \Gamma_4^- + 2\Gamma_5^-$	-	even	odd
D	$\Gamma_1^+ + 2\Gamma_3^+ + 3\Gamma_4^+ + \Gamma_5^+$	+	odd	even
F	$2\Gamma_1^- + \Gamma_2^- + 2\Gamma_3^- + 4\Gamma_4^- + 3\Gamma_5^-$	-	even	odd
G	$\Gamma_1^+ + 2\Gamma_2^+ + 3\Gamma_3^+ + 4\Gamma_4^+ + 5\Gamma_5^+$	+	odd	even
H	$\Gamma_1^- + 2\Gamma_2^- + 4\Gamma_3^- + 5\Gamma_4^- + 6\Gamma_5^-$	-	even	odd

5.1.4 *Rydberg exciton and light mode spatial extension*

A large spatial overlap of light field and matter wave yields an enhanced optical excitation. Rydberg excitons are mesoscopic quantum objects with variable sizes in the hundreds of nanometer range depending on the principal quantum number n, and excitation energies in the visible light range. OAM light in the visible can be focused down to a few hundreds of nanometer. Comparing the Rydberg exciton radial wave function with the Laguerre-Gauss mode extension, we can predict, for which principal quantum number n a Rydberg exciton in Cu_2O would most likely interact with focused OAM light.

The excitonic radial wave function $r^2 R^2_{\mathrm{Cu_2O}}(r)$ is calculated in analogy to the hydrogen radial wave function $R_{nl}(r)$ (see Eq. (2.19) in Section 2.2.3). The light mode spatial extension is calculated from the formula for Laguerre-Gauss modes in Eq. (2.50) in Section 2.4.1.

At the focus $z = 0$, $R_{z=0} = \infty$, $\exp\left(ikr^2/2R_{z=0}\right) = 1$, $w_{z=0} = w_0$, $\phi_{z=0} = \arctan(0) = 0$, $e^{i\phi_{z=0}} = 1$, and $L_0^1 = 1$. For $l = 1$, the Laguerre-Gauss mode at the focal point then becomes:

$$A_{10}\left(r, \varphi = 0, z = 0\right) = \frac{4r^3}{\sqrt{\pi} w_0^4} e^{-\frac{r^2}{w_0^2}} e^{i\varphi}. \tag{5.13}$$

As the mode is cylindrically symmetric, we set $\varphi = 0$ and plot the intensity distribution given by the absolute value squared as a function of r:

$$|\boldsymbol{A}_{10}\left(r, \varphi = 0, z = 0\right)|^2. \tag{5.14}$$

The beam waist in a Laguerre-Gauss mode refers to the thickness of the Laguerre-Gauss ring. We evaluate the maximum of the intensity cross section curve $max|\boldsymbol{A}_{10}\left(r,\varphi=0,z=0\right)|^2$ and calculate the radius at which the function is decayed to the $1/e^2$ of its maximum value, which we then define as the radius of the Laguerre-Gauss mode. For a beam waist $w_0 = 250\,\text{nm}$ this gives a radius $r = 497\,\text{nm}$.

The S-exciton radial wave functions $r^2R^2_{\text{Cu}_2\text{O}}\left(r\right)$ for principal quantum numbers $n = 8\ldots14$ are visualized in Fig. 5.2 together with the radial intensity distribution of a Laguerre-Gauss-mode $|\boldsymbol{A}_{10}\left(r,\varphi=0,z=0\right)|^2$ with beam waist $w_0 = 250\,\text{nm}$ and orbital angular momentum $l = 1$. From here we see that S-exciton states with principal quantum number $n = 12$ show the largest overlap with the spatial mode of $l = 1$ OAM light when focused down to a spot of $w_0 = 250\,\text{nm}$ beam waist.

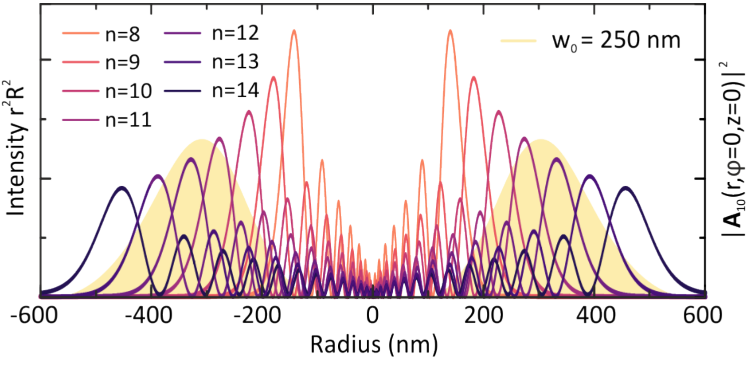

FIGURE 5.2. Comparison of Rydberg S-exciton radial wave functions $r^2R^2_{\text{Cu}_2\text{O}}\left(r\right)$ with principal quantum numbers $n = 8\ldots14$ and radial intensity distribution of a Laguerre-Gauss mode $|\boldsymbol{A}_{10}\left(r,\varphi=0,z=0\right)|^2$ with beam waist $w_0 = 250\,\text{nm}$ and orbital angular momentum $l = 1$.

5.2 EXPERIMENTAL INVESTIGATIONS

Using orbital angular momentum light will modify the absorption spectrum of Cu_2O Rydberg excitons. It will, in particular, alter the parity of the visible Rydberg states. The studies of the even-parity S- and D-excitons [13, 14, 35, 36, 39] are much fewer compared to the studies of the dipole-allowed odd-parity P-excitons [30, 44, 46, 47, 87, 102, 167, 168]. Our aim is to experimentally verify different transition probabilities of Rydberg exciton states in dependence on their principal quantum number n, the exciton envelope wave function (angular momentum quantum number l^{exc}), as well as the OAM quantum number l of the light. This way, we directly combine experimentally structured light fields, such as OAM light, and mesoscopic quantum objects, such as Rydberg excitons in Cu_2O, where a perfect size match of light and matter is prevalent.

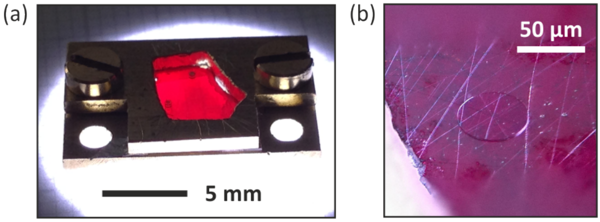

FIGURE 5.3. (a) Photograph picture of a Namibian cuprous oxide crystal mounted in a brass sample holder. 3D-printed lenses on top of OAM phase plates can be seen as dark dots on the crystal surface. (b) Close-up of an OAM phase plate on the cuprite crystal surface.

Preliminary measurements have been performed on Sample 0 (see Table 4.1) with Setup A in the Dortmund lab (see Fig. 3.8). Absorption spectroscopy in transmission configuration has been conducted. The Namibian crystal is 80 µm to 100 µm thick, oriented along {110} crystal plane, and glued on a glass substrate. OAM plates are directly printed onto the crystal surface using direct laser writing (see Fig. 5.3). The laser spot diameter is 100 µm, the laser power accounts for 8 µW. The measured spectra are shown in Fig. 5.4. 3S- and 4S-excitons appear within the crystal upon excitation with $l = 1$ OAM light. In contrast, for excitation with $l = 0$ light, i.e. a Gaussian beam, no S-exciton appears on the lower energy side of the P-excitons.

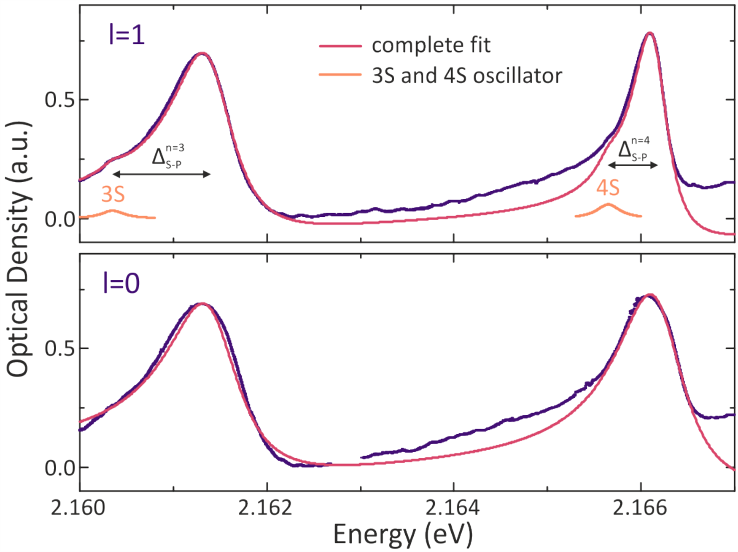

Figure 5.4. 3S- and 4S-excitons appear on the low-energy side of the P-excitons for excitation with $l = 1$ OAM light (see upper panel), while they are absent for excitation with $l = 0$ (dipolar) light (see lower panel).

The data have been shifted and scaled in y direction for a better comparison. For excitation with $l = 1$ OAM light, oscillators for P- as well as S-excitons have been fitted for principal quantum numbers $n = 3$ and $n = 4$. For excitation with a Gaussian beam, only P-exciton oscillators have been fitted. While the S-exciton is

TABLE 5.12. Fit parameters of 3P-, 3S-, 4P-, and 4S-excitons for excitation with $l = 1$ OAM light and a Gaussian beam ($l = 0$). A Lorentzian line shape has been fitted to the S-excitons, while an asymmetric Lorentzian has been fitted to the P-excitons. The displayed fit parameters are: oscillator strength C, damping constant Γ, and asymmetry parameter q_n. Energy positions are given as 2.160 eV + Δ_E.

Parameter	3S	3P	3P	4S	4P	4P
	$l = 1$		$l = 0$	$l = 1$		$l = 0$
$C\ (\cdot 10^{-4})$	0.05	2.5	2.8	0.09	1.75	3.15
$\Gamma\ (\cdot 10^{-4})$	3.0	8.0	9.3	3.0	4.6	8.8
q	0	-0.3	-0.3	0	-0.25	-0.25
Δ_E (meV)	0.35	1.42	1.44	5.65	6.15	6.20

described by a Lorentzian oscillator $S_n(x)$, analogously to Eq. (2.23) in Section 2.2.4,

$$S_n(x) = C_n \frac{\Gamma_n/2}{(\Gamma_n/2)^2 + (x - E_n)^2}, \tag{5.15}$$

with principal quantum number n, oscillator strength C_n, damping constant Γ_n, and energy E_n, the P-exciton is reproduced by an asymmetric Lorentzian oscillator $P_n(x)$, analogously to Eq. (2.24) in Section 2.2.4,

$$P_n(x) = C_n \frac{\Gamma_n/2 + 2q_n(x - E_n)}{(\Gamma_n/2)^2 + (x - E_n)^2}, \tag{5.16}$$

with an additional asymmetry parameter q_n. All fit parameters are listed in Table 5.12.

With our preliminary measurements, we were able to detect small hints of modified selection rules in cuprous oxide Rydberg excitons using OAM light. S-excitons appear according to the calculated selection rules for excitation with $l = 1$ OAM light (see Table 5.11 in Section 5.1), while they are not visible for excitation with $l = 0$ (dipolar) light. Although selection rules allow the new transitions, they might still be very weak. The spectral distance between S- and P-excitons accounts for $\Delta^{n=3}_{SP,fit} = 1.07\,\text{meV}$ and $\Delta^{n=4}_{SP,fit} = 0.50\,\text{meV}$ for the $n = 3$ and $n = 4$ states, respectively. This is in good agreement with literature values $\Delta^{n=3}_{SP,lit} = 1.06\,\text{meV}$ and $\Delta^{n=4}_{SP,lit} = 0.54\,\text{meV}$ [83].
Nevertheless, the P-excitons do not disappear in measurements with $l = 1$ OAM light, but are nearly unchanged compared to in measurements with dipolar light. Unfortunately, we were not able to achieve a light focus smaller than the spiral phase plate. This way, a non-negligible part of excitons might have been excited with pure dipolar light outside the phase plate, leading to a strong P-exciton resonance. Furthermore, with the new selection rules for $l = 1$ OAM light, P-excitons are predicted to be dipole-forbidden. However, they become quadrupole-allowed, so their oscillator strength might still be considerable in the absorption spectrum.

5.3 CONCLUSION AND OUTLOOK

Orbital angular momentum light is a light field, where phase and intensity vary with position. Its role in exciting optical transitions in materials has been little examined so far [169]. Exciting materials by light is one of the most fundamental ways to study their physical properties. The emergence of OAM light has provided intriguing possibilities to induce optical transitions beyond the framework of electric dipole interaction [170].

In this chapter we have given a detailed group-theoretical analysis of orbital angular momentum light and exciton symmetries in cuprite. The symmetries of OAM light with different amounts of OAM l as well as the symmetries of excitons with different envelope functions (angular momentum quantum number l^{exc}) have been calculated. Comparing their overlap allows us to predict that the alteration of the OAM of light modifies the optical transition selection rules, and that, hence, usually dipole-forbidden Rydberg excitons in Cu_2O can be excited.

We find that excitons with S- and D-envelope wave function should be excitable with $l = 1$ and $l = 3$ OAM light. The precise oscillator strength of the transitions, however, requires further detailed theoretical investigation, meaning elaborate numerical calculations, taking the exact band structure, the exciton envelope wave function, and the exact spatial shape and extension of the OAM beam into account. However, it has been shown that the normally weak optical quadrupole interaction in atoms is enhanced significantly when the atom interacts at near resonance with an optical vortex [123]. Furthermore, such transition amplitudes have been calculated for excitation of hydrogen-like atoms with OAM light [120]. Here, if the target atom is located at distances of the order of atomic size near the phase singularity in the vortex center, the transition rates into states with OAM $l > 1$ become comparable with the rates for electric dipole transitions. As the mesoscopic Rydberg exciton is per se centered with respect to the OAM beam upon excitation and senses the complete light field, we assume the effect to be substantially enhanced in solids as well.

Our first experiments show this expected enhancement, however, not with the expected strength. The increase in S-exciton oscillator strength does not exceed the decrease in P-exciton oscillator strength. Unfortunately, we were not able to achieve an optimum size match of light field and matter in our experiments. The investigated $n = 3$ and $n = 4$ excitons had sizes of only a few tens of nanometers, while the OAM light focal spot was as large as 100 µm.

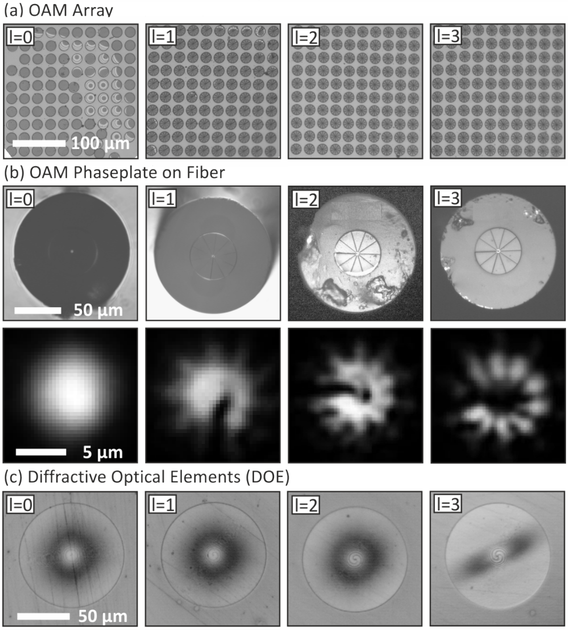

FIGURE 5.5. (a) Microscope images of OAM phase plate arrays directly printed onto the cuprite crystal surface using direct laser writing. The phase plate diameter is 20 µm. The center-to-center distance between phase plates equals 25 µm. The arrays consist of 10×10 phase plates with a total array size of 245 µm × 245 µm. Arrays with orbital angular momentum $l = 0 - 3$ are shown from left to right. (b) OAM phase plate directly printed on a fiber facet. The phase plate diameter is 50 µm. The imposed amount of orbital angular momentum increases from left to right from $l = 0$ to $l = 3$. Microscope images of the corresponding light modes are also shown. (c) Microscope images of diffractive optical elements directly milled into the cuprite crystal. The diffractive optical elements combine a certain amount of orbital angular momentum ($l = 0 - 3$ from left to right) with focusing properties. Their diameter is 100 µm.

In order to even further enhance the new transitions, one could use more effective OAM arrays consisting of many OAM phase plates, as shown in Fig. 5.5 (a). This way, an additional amount of OAM l is added to the light hitting the crystal at different nearby positions simultaneously. Even more success is expected when phase plates are printed directly on fiber facets. An additional amount of OAM l is added to the light, before it then is focused on independent positions on the crystal. Photograph pictures of an OAM phase plate on a fiber facet are shown in Fig. 5.5 (b) for $l = 1 - 3$ together with microscope images of the different light modes. In this case, the Cu_2O crystal remains bare, which guarantees that no additional strain is caused to the crystal by 3D printed optics. Furthermore, the freely-propagating OAM light could be focused to smaller diameters, as no visual poof of hitting an OAM phase plate is required. Last, the method of focused ion beam milling could be used in order to mill diffractive optical elements directly into the cuprous oxide surface. These structures can feature different amounts of OAM ($l = 0 - 3$, see Fig. 5.5 (c)) together with focusing properties. This would also help to achieve smaller focal spot sizes in the order of a few hundreds of nanometers.

OAM light is a new and ideal tool for selectively exciting dipole-forbidden states by linear optical absorption. In particular, cuprous oxide Rydberg excitons with extended wave functions are expected to provide an ideal platform for studying vortex light–matter interaction. The efficient OAM exchange between light and elementary excitations in solid-state systems will form the foundation of innovative solid-state devices for OAM applications [170]. Furthermore, the novel selection rules for OAM beams not only unlock forbidden excitations in cuprous oxide Rydberg excitons, but also enable new spectroscopic techniques in a wide range of physical systems [169]. The ability of OAM light to drive transitions beyond the dipole limit is an exciting potential application for quantum information and for enabling room-temperature quantum technologies [171].

6

SPECTROSCOPY OF NANOANTENNA-COVERED Cu_2O – TOWARDS ENHANCING QUADRUPOLE TRANSITIONS IN RYDBERG EXCITONS

This chapter is based on the following publication [172]:
A. Neubauer, J. Heckötter, M. Ubl, M. Hentschel, B. Panda, M. Aßmann, M. Bayer, and H. Giessen, *Spectroscopy on nanoantenna-covered Cu_2O: Towards enhancing quadrupole transitions in Rydberg excitons*, Phys. Rev. B **106**, 165305 (2022).

Plasmonic antennas channel incoming electromagnetic energy into a confined nearfield. This results in a strongly inhomogeneous field-line distribution, and strong transverse field gradients at the edges of the antenna. Hence, the quadrupole moment is very strong, and the quadrupole operator, having symmetry $\Gamma_Q = \Gamma_3^+ + \Gamma_5^+$ is capable of driving quadrupole transitions to S- and D-excitons with symmetries $\Gamma_S = \Gamma_2^+ + \Gamma_5^+$ and $\Gamma_D = \Gamma_1^+ + 2\Gamma_3^+ + 3\Gamma_4^+ + \Gamma_5^+$ (see Fig. 6.1 (a)). Details on plasmonic nanostructures, selection rules, and exciton symmetry representations, can be found in Section 2.5, Section 2.2.2, and Section 2.2.5, respectively. Such plasmonic antennas can be directly printed on the cuprite crystal surface using lithography. By writing 200 × 200 μm-large arrays, the cuprite surface becomes equipped with lots of field gradients when being illuminated with a focused light beam.

Without plasmonic antennas, S- and D-excitons are dipole-forbidden. Addressing a variety of angular momentum exciton states is interesting for quantum information processing [173]. In particular, it is attractive to switch on and off optical transitions. We are able to

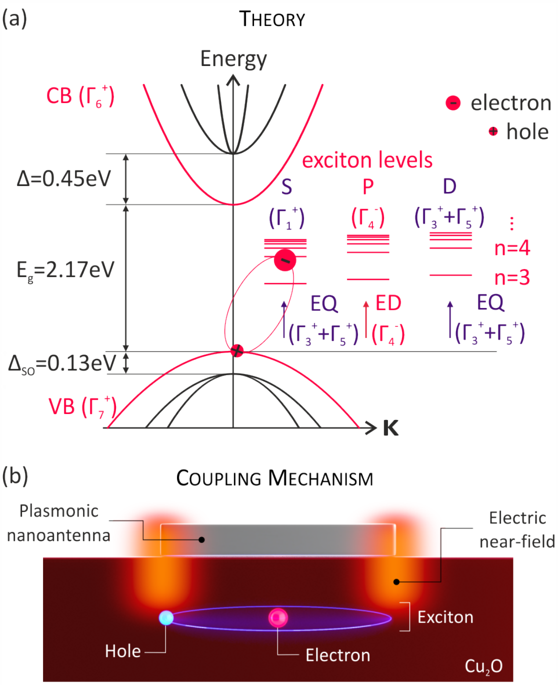

FIGURE 6.1. (a) Schematic drawing of the dispersion relation of cuprous oxide at the Γ-point. Energy gap (E_g), as well as crystal field (Δ) and spin-orbit (Δ_{SO}) splitting are indicated. The symmetries of conduction (CB) and valence (VB) bands, of S-, P- and D- exciton levels, as well as as of the corresponding light field operators (electric dipole ED / electric quadrupole EQ) are shown. (b) Illustration of the coupling mechanism between plasmonic nanoantenna and Rydberg excitons in cuprous oxide. Strong field gradients at the antenna tips are expected to strongly interact with the Rydberg excitons when brought in close distance.

design customized plasmonic antennas by adjusting their length, width, period, and material, so that we can tune the antenna plasmon resonance across the excitation wavelength for cuprous oxide Rydberg excitons, which is at 571 nm. Furthermore, the antennas can be designed in a way that the plasmon resonances are active along their long axis only, so the resonance can be turned on and off by changing the polarization direction of the illuminating light. In addition, the size of the Rydberg excitons will be comparable to the plasmon field gradient extension. This implies an interaction of the Rydberg exciton with the complete optical light field and should lead to an additional enhancement of the quadrupole transitions (see Fig. 6.1 (b)). The samples investigated in this chapter are specified in Table 4.1 in Section 4.5.

Section 6.1 shows measurements of the plasmonic antenna resonances of different antenna fields. The spectroscopy data of antenna-coupled cuprous oxide Rydberg excitons are discussed in Section 6.2 and Section 6.3 for reflection spectroscopy as well as pump-probe spectroscopy in transmission and reflection configuration. Section 6.4 treats the influence of pump-probe measurements on (antenna-coupled) cuprous oxide Rydberg excitons, and Section 6.5 summarizes this chapter and gives an outlook onto future experiments with antenna-coupled Rydberg excitons.

6.1 PLASMONIC ANTENNA RESONANCES

The samples used for pure reflection spectroscopy and pump-probe measurements in reflection geometry (Sample 1 and Sample 3) contain plasmonic aluminum antennas that are designed to be 30 nm wide and 60 nm to 110 nm long (see Table 6.1) in order to exhibit plasmon resonances along the long axis at exciton energies around 2.17 eV. By varying the length, the plasmon resonance can be tuned in energy, and by changing the laser polarization the plasmon resonance can be switched on and off (see Fig. 6.2). An in-house implementation of the Fourier modal method was used for the antenna design [155, 156]. We fabricate antenna arrays with periodicity between the antennas of 160 nm and extensions of $200 \times 200\,\mu\mathrm{m}^2$ in order to guarantee easy optical access in the experiments.

TABLE 6.1. Overview over different plasmonic antenna dimensions and the spectral position of their plasmonic resonance.

Name	length (nm) × width (nm)		Resonance
	Designed	Measured	
F1	110 × 30	115 × 40	> 600 nm
F2	90 × 30	95 × 40	600 nm
F3	80 × 30	85 × 35	575 nm
F4	70 × 30	75 × 35	550 nm
F5	60 × 30	65 × 35	525 nm

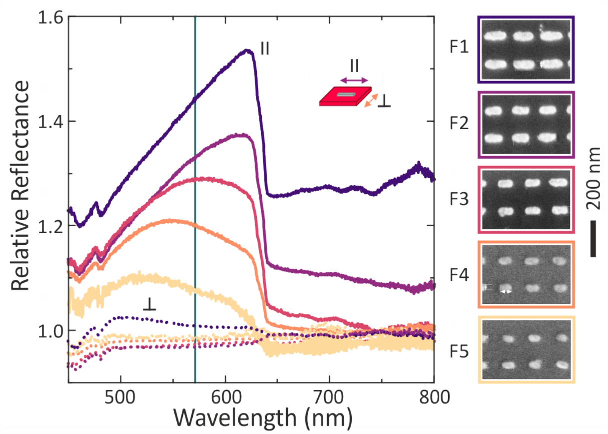

FIGURE 6.2. Measured plasmon resonances of antenna fields F1-F5 (on Sample 1 and Sample 3) together with their SEM images. The plasmon resonances are active for parallel (||) polarized light at energies around the exciton resonance at 571 nm (vertical green line). Relative reflectance is the ratio between reflectance measurements on the antenna fields over reflectance measurements on the Cu_2O surface without antennas.

The antenna resonances have been measured using bright field reflection microscopy (see Fig. 6.2). Under light excitation in parallel (||) polarization, the plasmon resonance is active along the long antenna axis, while no resonance appears for perpendicular (⊥) polarization. The plasmon resonances are very broad (> 100 nm) with their maximum shifting across the exciton resonance at 571 nm. While antenna field F5 has a plasmon resonance with maximum at 525 nm, antenna field F1 has the maximum above 600 nm. The antenna field reflectance is normalized to the pure cuprous oxide reflectance, so the displayed values are larger than 1, as Cu_2O has a lower reflectivity than aluminum. The corresponding SEM images of the different antenna fields in Fig. 6.2 illustrate that the overall reflectivity is largest on field F1 with the longest antennas, as the periodicity is the same for all antenna fields. The antennas in field F5 are the shortest, so their overall reflectivity is weakest.

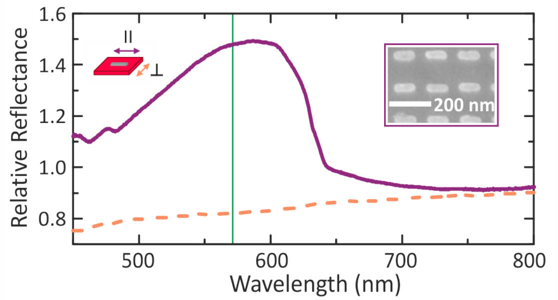

FIGURE 6.3. Measured plasmon resonance of antenna field on Sample 2 together with SEM image. The plasmon resonance is active for parallel polarized light at ∼ 575 nm. Vertical green line indicates the exciton resonance at 571 nm. Relative reflectance is the ratio between reflectance measurement on the antenna field over reflectance measurement on the Cu_2O surface without antennas.

Another sample with slightly different antenna parameters is used for pump-probe measurements in transmission configuration (Sample 2). The aluminum antennas are 100 nm long and 25 nm wide, arranged at a periodic distance of 150 nm. The antenna field plasmon resonance is shown in Fig. 6.3 together with an SEM image and the schematic laser polarization configurations as inset.

6.2 PURE REFLECTION SPECTRA FROM ANTENNA-COUPLED CUPROUS OXIDE RYDBERG EXCITONS

The sample used for the following measurement (Sample 1, see Table 4.1 in Section 4.5) has been polished to a thickness of 46 µm. Experiments are performed in reflection geometry with 15° angle of incidence on Setup A in the Dortmund lab (see Fig. 3.8). Due to the small sample thickness, reflection as well as transmission spectroscopy can be performed. The laser spot diameter is 100 µm, the laser power is 6 µW. The cuprous oxide sample used is of good quality, proven by the transmitted and reflected spectra of a reference point (no antenna field) on Sample 1 in Fig. 6.4, where Rydberg excitons with principal quantum numbers up to $n = 21$ are measured in parallel laser polarization configuration.

The implementation of spectroscopy experiments in reflection geometry on cuprous oxide is not straight-forward. However, the spectra in Fig. 6.4 show that we were able to achieve successful results. Rydberg excitons with principal quantum number up to $n = 21$ are detected in the transmitted as well as in the reflected signal. Still, the reflected signal is much weaker than the transmitted one. Here, noise and, in particular, the oscillations from interferences in optical elements manifest themselves to a larger extent. By dividing the reflected signal by a reference signal, we can, nevertheless, remove most of the oscillations. In both transmitted and reflected signals we distinguish well P- and F-excitons. The P-exciton line shapes in the reflected signal are broader and more triangular-shaped when comparing to the transmitted signal. This is in good agreement with simulations from Ref. [102].

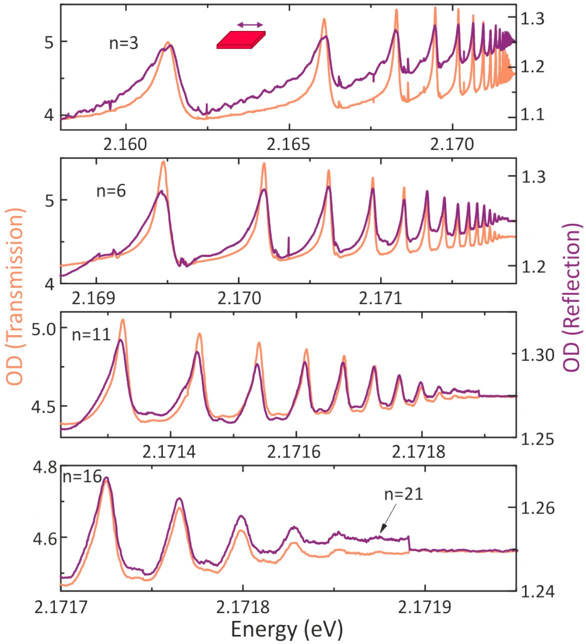

FIGURE 6.4. Optical density of transmitted and reflected signal on a reference spot on Sample 1. The spectra reveal the good quality of the crystal used, exhibiting Rydberg excitons with principal quantum numbers up to $n = 21$. The reflected signal is much weaker than the transmitted signal and exciton lines are broader with a flatter slope on the low-energy side.

The top row in Fig. 6.5 depicts the reflected signal from antenna field F5 on Sample 1 in parallel and perpendicular laser polarization configuration for $n = 5$ (left) and $n = 6$ (right) separately. The optical density data of the different polarization configurations have been shifted in y direction for a better comparison of the fitted oscillators. This does not change any physical content. The shifts are listed in Table 6.2. The key result is that 5S- and 6S-excitons appear on the left P-exciton shoulder for parallel laser polarization, while they are absent in perpendicular laser polarization.

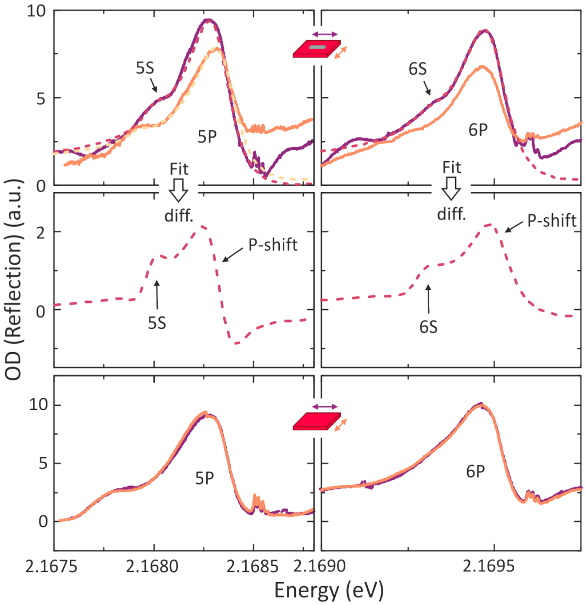

FIGURE 6.5. Top row: Comparison of the reflected signal in parallel and perpendicular laser polarization on antenna field F5 on Sample 1. 5S- and 6S-excitons appear on the left P-exciton shoulder in parallel laser polarization configuration, while they are absent in perpendicular laser polarization. Middle row: Fit difference of parallel and perpendicular data. Bottom row: Same data as in top row but for a reference (no antenna field). Here, no S-excitons appear in parallel laser polarization configuration.

TABLE 6.2. y-shift of optical density data from Sample 1 in arbitrary units for a better comparison of the fitted oscillators for parallel (||) and perpendicular (⊥) laser polarization and principal quantum numbers $n = 5$ and $n = 6$.

n	||	⊥
5	-1.105	+0.75
6	-1.13	+0.71

In order to highlight the antenna effect, 5S- and 6S-excitons have been fitted with a Lorentzian function S_n of the form of Eq. (2.23):

$$S_n(x) = C_n \frac{\Gamma_n/2}{\left(\Gamma_n/2\right)^2 + \left(x - E_n\right)^2}, \tag{6.1}$$

with principal quantum number n, oscillator strength C_n, damping constant Γ_n, and energy E_n. P-excitons have been fitted with an asymmetric Lorentzian function P_n (Eq. (2.24) in Section 2.2.4):

$$P_n(x) = C_n \frac{\Gamma_n/2 + 2q_n\left(x - E_n\right)}{\left(\Gamma_n/2\right)^2 + \left(x - E_n\right)^2}, \tag{6.2}$$

with an additional asymmetry parameter q_n that accounts for $q_5 = -0.35$ and $q_6 = -0.33$ for the 5P- and 6P-exciton, respectively. All other fit parameters are listed in Table 6.3.

The difference of the fits for parallel and perpendicular data are displayed in the middle row in Fig. 6.5. Despite a feature that accounts for the different P-exciton parameters in parallel and perpendicular measurements, the S-exciton, which appears stronger in parallel polarization, is clearly visible. The bottom row in Fig. 6.5 shows the same data as in the top row but for a reference spot. Here, no S-excitons appear in parallel laser polarization configuration.
The peak-to-peak energy difference between S- and P-excitons in Fig. 6.5 are $\Delta_{SP}^{n=5} = 250\,\mu\text{eV}$ and $\Delta_{SP}^{n=6} = 150\,\mu\text{eV}$, while the difference of energy positions of the fitted oscillators is $\Delta_{SP,fit}^{n=5} = 320\,\mu\text{eV}$ and $\Delta_{SP,fit}^{n=6} = 200\,\mu\text{eV}$. These values agree well with literature values: $\Delta_{SP,lit}^{n=5} = 270\,\mu\text{eV}$ and $\Delta_{SP,lit}^{n=6} = 168\,\mu\text{eV}$ [83].

For the P- and S-exciton fits, respectively, we use the same damping constant Γ_n in parallel and perpendicular measurement. This allows for a comparison of the oscillator strength ratio C_S/C_P . We find an increase of this relative S-exciton oscillator strength with respect to the P-exciton oscillator strength of 1.42 and 1.18 for $n = 5$ and $n = 6$, respectively (see Table 6.3), for parallel laser polarization compared to perpendicular laser polarization. One might attribute the enhancement of the dipole-forbidden S-exciton to strain or local electric fields from the antennas. However, this effect would also occur in perpendicular polarization, which clearly is not the case, and should be independent of the antenna detuning.

TABLE 6.3. Fit parameters of 5P-, 5S-, 6P-, and 6S-excitons for parallel (||) and perpendicular (⊥) measurements. A Lorentzian line shape has been fitted to the S-excitons, while an asymmetric Lorentzian has been fitted to the P-excitons. Energy positions are given as 2.168 eV + Δ_E.

Param.	5P $\parallel$	5S $\parallel$	5P $\perp$	5S $\perp$	6P $\parallel$	6S $\parallel$	6P $\perp$	6S $\perp$
C $(\cdot 10^{-7})$	99	6.2	80	3.5	57	4.0	42	2.5
Γ $(\cdot 10^{-4})$	2.6	1.4	2.6	1.4	1.6	1.2	1.6	1.2
Δ_E (meV)	0.32	0.00	0.50	-0.08	1.5	1.3	1.49	1.3
C_S/C_P $(\cdot 10^{-3})$	0.06263		0.04375		0.07017		0.05952	

For certain crystal orientations, as for the one of the investigated samples ({-1,-1,0}), the S-exciton is per se forbidden in one polarization configuration while it is allowed in the perpendicular polarization configuration. This can be determined by group-theoretical considerations with the help of the tables by Koster [88]. The reference measurement in the lower panel of Fig. 6.5 shows, that this effect is not visible in the chosen polarization configurations. Here, for both parallel and perpendicular laser polarization no S-exciton appears. This confirms that the effect seen in the upper panel is due to the quadrupole enhancement caused by the plasmonic antennas.

6.3 PUMP-PROBE SPECTRA FROM ANTENNA-COUPLED CUPROUS OXIDE RYDBERG EXCITONS

6.3.1 *Relative transmittance spectra*

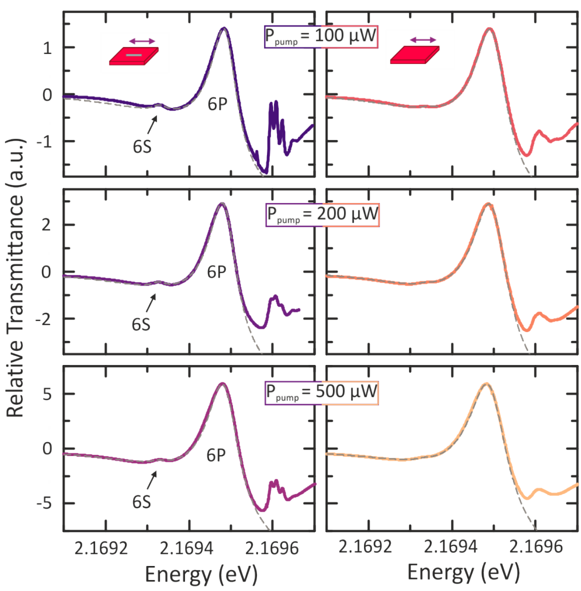

FIGURE 6.6. Relative transmittance data from antenna-coupled Cu_2O (Sample 2) for different pump power settings. Probe power accounts for 1 µW. Pump power varies from 100 µW (top) to 500 µW (bottom). Pump and probe lasers are both parallel polarized with respect to the plasmonic antenna long axis. Left column shows relative transmittance spectra together with fit functions for the antenna field, right column shows the same for a reference. P-excitons are scaled before fitting in order to adjust the P-exciton height for comparison. The 6S-exciton appears for all pump power settings on the antenna fields, while it is absent on the reference.

In this measurement pump-probe spectroscopy is performed on antenna-coupled cuprous oxide (Sample 2, see Table 4.1 in Section 4.5) in transmission configuration using Setup B in the

Dortmund lab (see Fig. 3.9). The Cu_2O sample has been polished to a thickness of 55-75 µm. The spectroscopy data are shown in the left column in Fig. 6.6 for Rydberg excitons with principal quantum number $n = 6$. The probe power accounts for 1 µW, the pump power is varied from 100 µW (top row) via 200 µW (middle row) to 500 µW (bottom row). Pump and probe lasers are both parallel polarized with respect to the plasmonic antenna long axis. Reference measurements are shown in the right column of Fig. 6.6. In all measurements on the antenna field, the 6S-exciton clearly appears at an energy 200 µeV lower than the P-exciton, while it is absent or only weakly present on the reference.

In order to quantify the relative increase of S-exciton oscillator strength with respect to the P-exciton caused by the plasmonic antennas, the data have been fitted. A Lorentzian function was used for describing the S-exciton, and an asymmetric Lorentzian function was used for describing the P-exciton. A parabolic background function was added. The complete fitting function reads:

$$\begin{aligned} f_6\left(x\right) &= A + D \cdot \left(x - E_d\right)^2 \\ &+ C_6 \frac{\Gamma_6/2 + 2q_6\left(x - E_6\right)}{\left(\Gamma_6/2\right)^2 + \left(x - E_6\right)^2} + C_s \frac{\Gamma_s/2}{\left(\Gamma_s/2\right)^2 + \left(x - E_s\right)^2}, \end{aligned} \tag{6.3}$$

with background parameters A, D, and E_d, as well as P- and S-exciton oscillator strengths C_6 and C_s, damping constants Γ_6 and Γ_s, and energies E_6 and E_s. For all measurements, the S-exciton damping constant Γ_s is kept constant. This way, we calculate from the fit function parameters C_6 and C_s for each pump power setting a relative enhancement factor of the S-exciton with respect to the P-exciton C_s/C_6 for measurements on the antenna field compared to a reference spot. These enhancement factors EF are listed in Table 6.4 together with all other fit parameters. The calculated S-exciton enhancement factor accounts for a factor of up to 4.

Table 6.4. Fit parameters for (asymmetric) Lorentzian function for 6S(6P)-excitons on an antenna field (Ant.) and a reference (Ref.) on Sample 2 in pump-probe experiment in transmission configuration. The ratio of S-exciton to P-exciton oscillator strength C_s/C_p as well as the enhancement factor EF of the S-excitons when being excited via nanoantennas is given. Data have been fitted for different pump power settings.

	$P_{\text{Pump}} = 100\,\mu\text{W}$		$P_{\text{Pump}} = 200\,\mu\text{W}$		$P_{\text{Pump}} = 500\,\mu\text{W}$	
Parameter	Ant.	Ref.	Ant.	Ref.	Ant.	Ref.
A	-0.16	-0.16	-0.4	-0.4	-0.9	-1.0
$D\left(\cdot 10^{6}\right)$	-5	-5	-10	-10.5	-20	-20
E_d	2.169	2.169	2.169	2.169	2.169	2.169
$C_6\left(\cdot 10^{-4}\right)$	1.0	1.2	2.25	2.8	5.1	6.2
$\Gamma_6\left(\cdot 10^{-5}\right)$	7.6	9.0	8.3	10	9.2	11
q_6	-0.18	-0.18	-0.19	-0.19	-0.16	-0.16
E_6	2.1695	2.1695	2.1695	2.1695	2.1695	2.1695
$C_s\left(\cdot 10^{-6}\right)$	2.5	0.7	4.0	1.5	5.0	2.7
$\Gamma_s\left(\cdot 10^{-5}\right)$	4.0	4.0	4.0	4.0	4.0	4.0
E_s	2.1693	2.1693	2.1693	2.1693	2.1693	2.1693
C_s/C_6	0.025	0.0058	0.0177	0.0053	0.0098	0.0043
EF	4.3		3.3		2.3	

From the antenna enhancement point of view we expect the relative enhancement to be as large as 10. Measuring in transmission configuration, we do not only capture the quadrupole contribution from the antennas that sit on the sample surface but also the dipole contribution coming from the inner bulk sample. As the quadrupole transition (S-exciton) is three orders of magnitude smaller than the dipole transition (P-exciton), its contribution to the measurement signal might remain small despite the antenna enhancement. In order not to measure the bulk contribution, in the next section, we performed pump-probe spectroscopy in reflection configuration.

6.3.2 *Relative reflectance spectra*

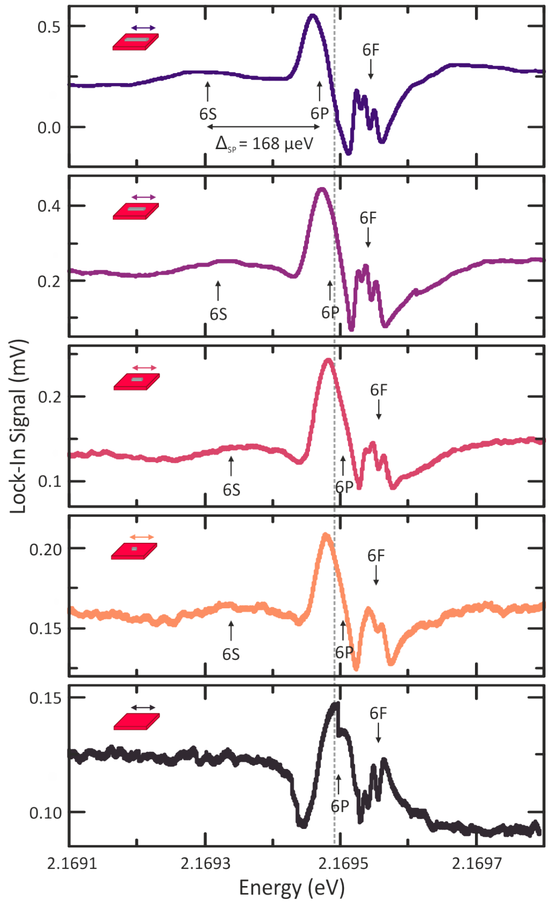

Figure 6.7. Pump-probe spectroscopy in reflection geometry. Data of $n = 6$ excitons on different antenna fields (F1-F4) and a reference point (from top to bottom) on Sample 3 for parallel laser polarization with respect to the plasmonic antenna long axis are shown. The S-exciton appears on different antenna fields, while it is absent in the reference. A fixed P-exciton energy is indicated at 2.17079 eV by the gray dashed line.

The cuprous oxide crystal used for the pump-probe measurement in reflection geometry is Sample 3 (see Table 4.1 in Section 4.5). In order to only capture the influence of the antennas sitting on the crystal surface, experiments are performed in reflection geometry with 15° angle of incidence using pump-probe spectroscopy (Setup C, Stuttgart lab, see Fig. 3.10). The probe laser spot diameter is 150 µm, pump power is 3 mW, and probe power is 40 µW. Pump and probe lasers are both parallel polarized with respect to the plasmonic antenna long axis.

Pump-probe spectroscopy in reflection geometry on $n = 6$ excitons reveals that in parallel laser polarization the S-exciton clearly appears on different antenna fields (F1-F4), while it is absent in the reference measurement (see Fig. 6.7). The S-exciton appears much broader in the reflection measurement compared to the transmission measurement. This time, we cannot give a quantitative number for the relative S-exciton enhancement caused by the plasmonic antennas, as no data for perpendicular laser polarization are available. Still, the appearance of the S-exciton, triggered by the plasmonic antennas, remains a small feature.
Furthermore, we would expect the appearance of the S-exciton to come along with a decrease in oscillator strength of the P-exciton. Despite the fact that the signal has been measured in reflection geometry, most probably both reflections from sample front and back facets have been captured due to the small thickness of the sample. Hence, not only the influence of the antennas that sit on the sample surface is displayed in the spectroscopy data, but also the influence of the dipole transitions (P-excitons) in the inner bulk sample. Therefore, also in the reflected signal, we detect large P-excitons accompanied by small S-excitons.

From the measurements on different antenna fields and the reference we notice that the signal strength continuously increases from the reference via antenna fields F4, F3, F2, towards field F1.

Here, the overall reflectivity of the sample plays a crucial role. On antenna field F1, the antennas are longest. As the periodicity is kept constant for all antenna fields, more aluminum covers the cuprous oxide, so the overall reflectivity is highest. This could also have an influence on the coupling strength between plasmonic antenna and Rydberg exciton.

6.4 POSSIBLE INFLUENCE OF PUMP-PROBE SPECTROSCOPY ON ANTENNA-COUPLED Cu_2O RYDBERG EXCITONS

Spectroscopy on Rydberg excitons in cuprous oxide is quite difficult, as the excitons manifest themselves as tiny features on a huge background. In such a case, linear absorption spectroscopy often yields not enough signal-to-noise ratio. Therefore, we use pump-probe spectroscopy, which is a differential spectroscopy method, yielding a higher signal resolution. Using pump-probe spectroscopy one is able to capture much better small signals on a larger background. This way, more precise data can be acquired.

Nevertheless, with respect to Rydberg excitons in cuprous oxide, the data becomes more difficult to interpret. In pure transmission or reflection measurements the P-excitons can be modeled as asymmetric Lorentzian oscillators, representing the interplay of a discrete excitation in the crystal and a broad phonon background. The absorption through the crystal is clearly defined. In pump-probe spectroscopy, however, things become more complicated. One of the main difficulties is that the exciton lineshape is not clearly defined anymore and takes odd shapes. With respect to the antenna-coupled measurements, the comparison to a reference is often not possible, due to different signal strengths and the fact that scaling the data is not straight-forward anymore.

Furthermore, shining two lasers onto the sample implies one more influence on the excitons. The pump laser creates an exciton plasma. With the pump laser on, no excitons can be created. With the pump laser off, a signal similar to the one of linear absorption spectroscopy is detected. In the end, both signals are subtracted. The influence of the pump laser on the exciton plasma is, in particular, a challenge. We noticed a high sensitivity of the Rydberg exciton spectra with respect to the pump power settings, i.e., changing oscillator shapes, which we attributed to the influence of the pump laser on the electron-hole plasma. Our focus is on the overall signal behavior in dependence on different plasma environments, meaning different pump and probe laser powers, but also laser polarization and antenna configuration settings.

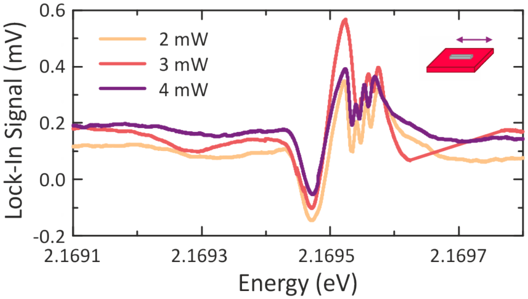

FIGURE 6.8. Relative reflectance spectra from antenna-coupled cuprous oxide Rydberg excitons with principal quantum number $n = 6$, measured on antenna field F1 on Sample 3. Data are shown for 40 µW probe laser power for three different pump laser powers (2 mW, 3 mW, and 4 mW).

In Fig. 6.8 relative reflectance spectra from antenna-coupled cuprous oxide Rydberg excitons with principal quantum number $n = 6$, measured on antenna field F1 on Sample 3 (see Table 4.1 in Section 4.5) using Setup C in the Stuttgart lab (see Fig. 3.10), are shown. Pump and probe lasers are parallel polarized with respect to the long antenna axis. The probe laser power is kept constant at 40 µW, while the pump laser power is varied from 2 mW to 4 mW. We find an increase in signal strength towards the pump power setting $P_{\mathrm{Pump}} = 3\,\mathrm{mW}$.

In order to investigate the dispersive and absorptive behavior of different *n*P-exciton resonances for a certain pump-probe power setting, we measured a relative reflectance spectrum from antenna field F4 on Sample 4 for a complete Rydberg series with principal quantum numbers $n = 5$ to $n = 14$. For complete sample specifications see Table 4.1 in Section 4.5. The spectroscopic data are shown in Fig. 6.9. Pump and probe lasers are parallel polarized. The probe laser power accounts for 40 µW, the pump laser power is 3.3 mW. Pump and probe laser powers have been optimized for the 5P-exciton to have a clear absorptive appearance. With this particular setting, the lineshape of the 6P-exciton experiences a flip, and all higher-*n* excitons appear with opposite sign. When we create a plasma, we have free carriers of electrons and holes separated, forming a charge cloud that prevents further exciton formation. However, lower-*n* state excitons are created with less energy. Therefore, $n = 5$ excitons can still be created, resulting in nice lineshapes, while it is not possible anymore for $n = 6$ states or higher. Increasing the pump power, should move the flip towards lower-*n* states. This, however, would at some point also reduce the signal-to-noise ratio.

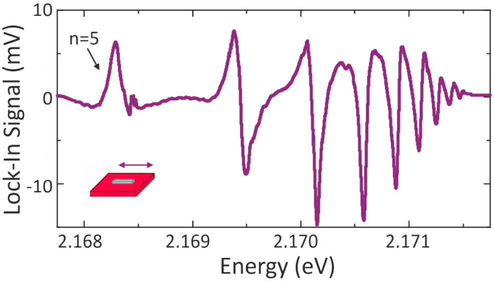

FIGURE 6.9. Influence of a certain pump-probe power setting on *n*P-exciton lineshape. Relative reflectance spectra are taken on antenna field F4 on Sample 4 with 3.3 mW pump power and 40 µW probe power. The exciton lineshape changes in dependence on the principal quantum number *n*.

In Fig. 6.10 we observe the exciton line flip in dependence on pump and probe laser powers. Data are shown for antenna field F4 on Sample 4. When increasing the pump laser power from 5 mW to 10 mW at a constant probe laser power of 25 µW (see Fig. 6.10 (a)) the exciton line flip indeed moves towards lower-n states. For higher pump power, more oscillator strength is shuffled towards lower-n states, therefore the flipping occurs at lower n. For $P_{\text{Pump}} = 10$ mW the flip occurs at $n = 8$, while for $P_{\text{Pump}} = 5$ mW the flip occurs at $n = 9$. In Fig. 6.10 (b) we observe another relation between pump and probe power. For higher probe powers higher pump powers are needed in order to achieve absorptive lineshapes. This also means that the lineshape flip occurs at higher pump powers for a given higher probe power. For $P_{\text{Probe}} = 20\,\mu$W probe power the lineshape flip occurs at $n \leq 8$, while for $P_{\text{Probe}} = 60\,\mu$W probe power the lineshape flip occurs at $n \gg 8$. Furthermore, for $P_{\text{Probe}} = 20\,\mu$W probe power, increasing pump power yields increasing oscillator strength at $n = 8$, while for $P_{\text{Probe}} = 60\,\mu$W probe power, increasing pump power yields decreasing oscillator strength. Here, different lock-in settings may play a role, too.

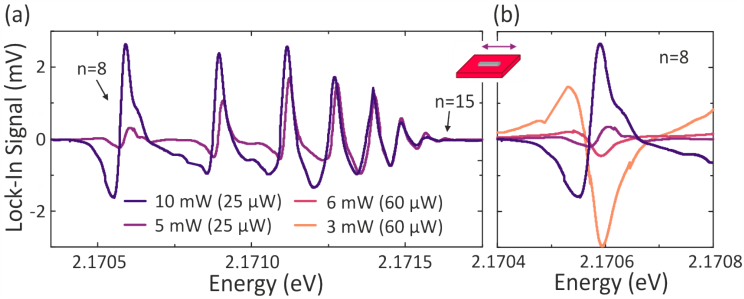

FIGURE 6.10. Influence of different pump-probe power settings on nP-exciton lineshape. Relative reflectance spectra are taken on antenna field F1 on Sample 4. Pump and probe laser powers are varied. The exciton line flip depends on both the pump and the probe laser powers.

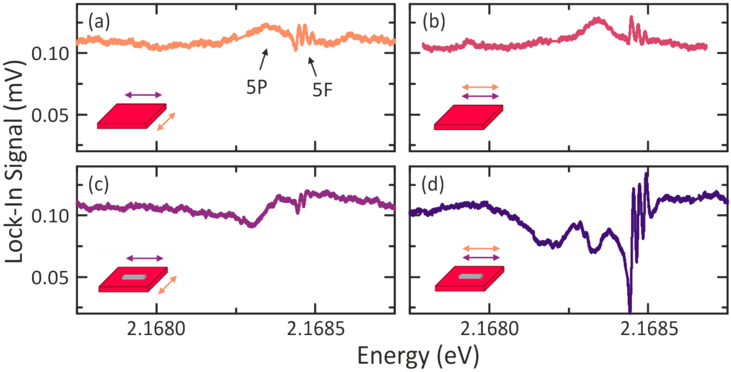

Figure 6.11. Influence of different laser polarization configurations with respect to the nanoantennas as well as influence of the nanoantennas themselves on the exciton lineshape. Data are shown for antenna field F4 as well a reference point on Sample 4. Pump laser power is 4 mW and probe laser power is 40 µW.

Not only pump and probe laser powers, but also the laser polarization configuration with respect to the nanoantennas as well as the nanoantennas themselves have an influence on the electron-hole plasma. These influences are shown by pump-probe measurements on antenna field F4 as well as on a reference point (no antenna field) on Sample 4, which are plotted in Fig. 6.11. The probe laser power is 40 µW, the pump laser power is 4 mW. For both probe and pump laser being parallel polarized with respect to the long antenna axis, 5P- and 5F-excitons appear stronger (see Fig. 6.11 (d)) compared to the case when only the probe laser is parallel polarized (see Fig. 6.11 (c)). This effect is absent when no antenna is present (see Fig. 6.11 (a,b)). Due to the fact that the antenna plasmon resonances are spectrally broad (100 nm, see Section 6.1), they are also excited by the pump laser that lases at 561 nm, only 10 nm shorter in wavelength than the probe laser. When comparing the reference data with the antenna data, for both laser polarization configurations and for the same pump and probe laser powers, the P-exciton resonance is absorptive on the reference (Fig. 6.11

(a,b)), but dispersive on the antenna field (Fig. 6.11 (c,d)). This is in agreement with the previous interpretation about the influence of the pump laser power on the electron-hole plasma. Due to a better coupling between light field and exiton, mediated by the plasmonic nanoantennas, with the same pump and probe powers, the effective plasma should already be stronger on the antenna field. This prevents exciton formation earlier, meaning at a lower pump power or lower principal quantum number *n*, than for the reference.

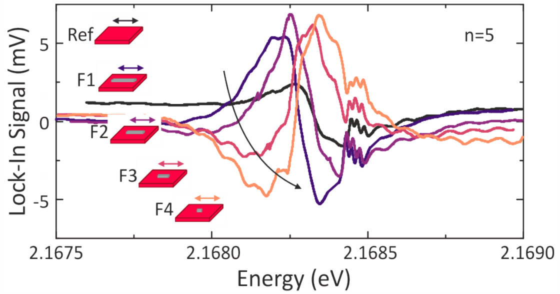

FIGURE 6.12. Influence of different plasmonic nanoantennas (F1-F4) on Sample 4 on the 5P-exciton lineshape. With increasing resonance match of nanoantenna and Rydberg exciton, the P-exciton lineshape becomes increasingly dispersive.

Another measurement series, shown in Fig. 6.12, strengthens the above assumption that the coupling between light field and exciton, mediated by the plasmonic nanoantenna, has an influence on the electron-hole plasma. Fig. 6.12 shows pump-probe measurements with pump and probe laser both parallel polarized with respect to the long antenna axis and 3 mW pump as well as 40 µW probe laser power. For all different measurements, the 5P-exciton lineshape is not very nice, however, we detect a flip of the lineshape from absorptive when measuring on the reference point towards increasingly dispersive when measuring on the antenna fields F1 through F4. For antenna field F4 the match between plasmon resonance energy and exciton energy is the best. The antennas channel the incoming light, which results in a higher effective plasma on the field, which then has an influence on the exciton formation and would most likely change their lineshape. This would also be in accordance with the previous interpretation. On antenna field F4 we also expect the largest shuffling-away of oscillator strength from the P-exciton towards quadrupole-allowed excitons due to the best matched resonance position. Quadrupole-allowed S- and D-excitons, however, remain absent in this measurement.

In summary, we can say that pump and probe laser power settings determine the exciton lineshape nature, meaning whether they appear as absorptive or dispersive lineshape. Pump and probe laser polarization configurations with respect to the long antenna axis do also have an influence on the signal strength due to better coupling of the light field into the crystal and to the Rydberg exciton when the plasmon antenna is active. This means that the enhanced quadrupole fields from the nanoantennas on the cuprite crystal surface directly influence the strength and lineshape nature of the Rydberg excitons. Furthermore, lock-in settings can be responsible for whether the excitons appear with positive or negative sign in the spectrum.

6.5 CONCLUSION AND OUTLOOK

The increase of oscillator strength of the S-exciton under excitation via plasmonic nanoantennas is apparent in the different measurements presented in this chapter but still much weaker than expected. The plasmonic field enhancement accounts for a factor of ten, which is up to a factor of ten larger than the observed enhancement of even-parity Rydberg excitons in cuprous oxide. The Rydberg excitons might not couple as well as expected with the plasmonic antennas. The plasmonic antennas might also produce surface charges that partly cancel out the exciton charge distribution. This effect, also known as purifying effect [83], could lead to a suppression of exciton resonances.

In order to increase the quadrupole enhancement caused by plasmonic antennas with respect to Rydberg excitons, several methods could be used. First, the coupling between antenna and Rydberg excitons could be enhanced by localizing the Rydberg excitons very close to the antennas. This could be done by energy potential landscapes or by a stepwise excitation scheme involving microwave radiation. Second, one could polish the crystal to ultra-thin flakes with thickness below 10 µm and measure in transmission configuration. The transmitted signal is easier to interpret but will contain a significant amount of dipolar excited P-excitons. This amount will, however, be reduced in comparison to our current measurement setting by a factor of ten, so the antenna contribution gains more weight in the transmitted signal. Third, one could measure cuprite microcrystals [44] scattered among plasmonic nanoantennas. This way, the antenna field would cover the whole microcrystal. However, border effects might play a role.

We discovered that Rydberg excitons in cuprous oxide are very sensitive to pump-probe measurements. There are many factors, such as laser power and exciton plasma, that influence good experimental results. We succeeded with the implementation of reflection measurement schemes on Rydberg excitons in cuprous oxide, which is a first step towards quantum integrated fiber-detection schemes with Rydberg excitons. Spectroscopy of nanoantenna-covered cuprous oxide provides an additional way to manipulate excitonic states. The combination of plasmonic structures and Rydberg excitons in cuprous oxide creates a new functional material that allows for selectively addressing different angular momentum and principal quantum number states. This approach is attractive for quantum state engineering.

7

CONFINING RYDBERG EXCITONS INTO QUANTUM WELLS

This chapter is based on the following publication [45]:
A. Konzelmann, B. Frank, and H. Giessen, *Quantum confined Rydberg excitons in reduced dimensions*, J. Phys. B **53**, 024001 (2019).

Studies of Rydberg excitons in cuprous oxide have dynamically developed over the past years with the focus moving from the bulk medium towards nanostructures. The growing interest in optical properties of low-dimensional systems, such as quantum wells, wires, and dots, and their interplay with Rydberg excitons has been supported by the emergence of fabrication techniques [44]. One-dimensional chains of trapped Rydberg excitons [174], as well as radiative coupling of weakly confined excitons in cuprous oxide [175] and Rydberg exciton-polaritons in a cuprous oxide microcavity [176] have been studied. Interacting quasiparticles in semiconductor nanosystems are very attractive. Manipulation of their properties by external fields and tailoring of the environment by nanotechnology offers unique possibilities to control the quasiparticles, their arrangement, and their interactions on demand.

The local response of excitons changes on mesoscopic length scales, i.e., dimensions that are large compared to the lattice constant. Quantum confinement effects arise as soon as the spatial confinement is comparable to the quantum object's Bohr radius. Mesoscopic spatial confinements of the order of several µm are already known from studies of semiconductor thin films [177] and slabs [178, 179], as well as weakly confined excitons in wide quantum wells [180] and strongly confined excitons in quantum dots [181–183]. The band structure of a semiconductor in a mesoscopic confinement is only weakly changed compared to the bulk material [184]. This assumption allows to investigate solely changes in the envelope part of the wave function caused by the confinement potential and is called envelope function approximation.

Excitons in quantum wells are theoretically described by potential well calculations, the concept of which is well known and has already been performed extensively for electrons and holes in semiconductors [185]. An excitons is a fundamental optical excitation, where the Coulombic electron–hole attraction gives rise to bound states of its relative motion. Excitonic bound states in quantum wells are in many respects similar to impurity bound states, meaning that the electron and hole relative motion can be described by a Hamiltonian that is similar to that of an impurity [186].

In this chapter, theoretical calculations on the energies of quantum confined Rydberg excitons are performed. In Section 7.1 the calculation method is presented. Section 7.2 focuses on the Rydberg exciton diameter with respect to the quantum well size, which serves as a good parameter for defining different confinement regimes. Section 7.3 outlines the theory behind electron states for infinite potential barriers, which is then applied to weakly and strongly confined Rydberg excitons in cuprous oxide quantum wells in Section 7.4 and Section 7.5, respectively. Section 7.6 gives a summary and an outlook on Rydberg excitons in quantum wells.

7.1 METHOD FOR CALCULATING ENERGIES OF QUANTUM CONFINED RYDBERG EXCITONS

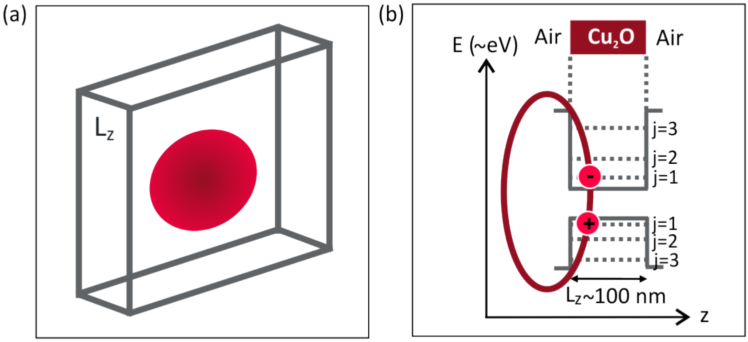

FIGURE 7.1. (a) Rydberg exciton confined in a cuprous oxide slab with a width comparable to the exciton diameter. This way the quantum object is weakly confined along the confinement axis. (b) In the weak confinement regime the exciton center-of-mass motion becomes quantized. Electron and hole are in a potential well with energy barrier of a few eV.

The quantum wells investigated consist of a cuprite slab that is extended many micrometers in x and y direction but confined to a few hundreds of nanometers only in z direction (see Fig. 7.1). They are surrounded by air or vacuum. The potential barrier accounts for 2.98 eV, which is given by subtracting the Rydberg exciton energy (2.17 eV) from the work function energy of electrons in cuprite to air (5.15 eV). This is much larger than the few hundreds of meV in GaAs-AlGaAs quantum well structures. The finite potential well energy in cuprous oxide quantum wells can be treated as an infinite potential barrier, as the linear dimension of the confinement exceeds the lattice constant of the semiconductor [184].

In the following, we focus on the weak confinement regime, where the confinement acts only on the center-of-mass motion of the exciton, i.e. the plane-wave part of the exciton wave function,

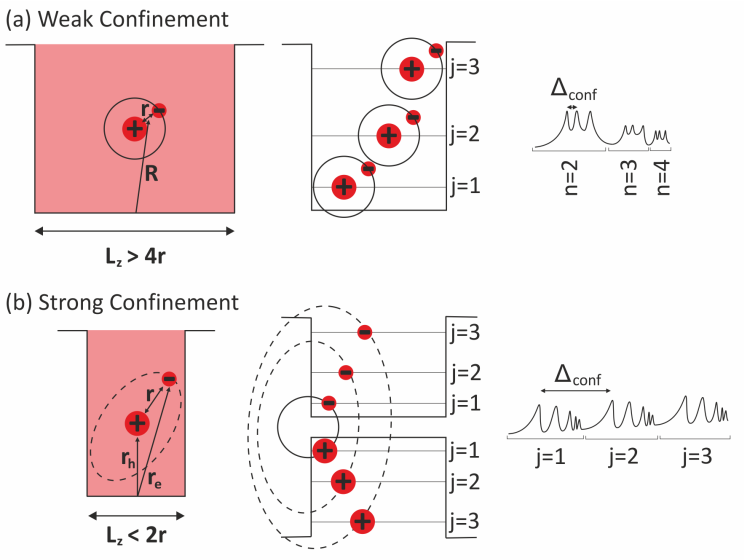

FIGURE 7.2. Quantum confined Rydberg exciton. (a) Weak confinement regime: The quantum well width L_z is larger than four times the exciton radius r. The confinement acts only on the center-of-mass coordinate R of the exciton. The energy shifts Δ_{conf} are small compared to the exciton binding energy. (b) Strong confinement regime: The quantum well width L_z is smaller than the exciton diameter $2r$. The confinement acts on electron r_e and hole r_h, which become confined into their own, separate quantum wells. The common energy shift of electron and hole is larger than the exciton binding energy.

and does not interfere with the relative motion of the electron-hole pair (see Fig. 7.2 (a)). Here, the Rydberg exciton binding energies are larger than the confinement effects. In contrast, in the strong confinement limit, the picture of an exciton would be destroyed, as one would then treat electron and hole separately with their individual motions being quantized (see Fig. 7.2 (b)). In this case, the confinement energy dominates over the Rydberg exciton binding energy.

As for a weak confinement of the exciton, the confinement or perturbation acts only on the center-of-mass coordinate and the relative motion is not disturbed, separation into center-of-mass and relative coordinates for solving the problem is possible. However, with this approximation a transition to the bulk material can not be realized. Furthermore, the Coulomb interaction, causing the electron and hole relative motion, is always of three-dimensional nature. Nevertheless, it depends on the relative electron-hole distance only, and, the perturbation of the weak confinement is assumed not to disturb the relative motion. Hence, a separation into relative and center-of-mass coordinates is possible as an approximation. Such potential well calculations for the center-of-mass coordinates of Rydberg excitons will give us a first estimation about the size of the energy shifts they experience when being confined to a cuprous oxide quantum well.

7.2 RYDBERG EXCITON DIAMETER VERSUS QUANTUM WELL SIZE

From quantum dots it is known that for confinements smaller than $0.4 \cdot a_B$, excitons break up [184]. On the other hand, for well widths $L_z \approx 4 \cdot a_B$, the energy shift should be most pronounced. In the following, we focus on weakly confined Rydberg excitons, i.e., Rydberg excitons in quantum wells of sizes

$$L_z \geq 4 \cdot r. \tag{7.1}$$

As the Rydberg exciton radius r increases with increasing principal quantum number n, we define a confinement parameter:

$$\Delta_L = L_z - 2r. \tag{7.2}$$

This allows to include the n-dependence of the confinement potential for a certain confinement length L_z. The weak confinement regime is then defined as:

$$\Delta_L \geq 2 \cdot r. \tag{7.3}$$

We calculated the Rydberg P-exciton radii in cuprite according to Eq. (2.16) in Section 2.2.3. The confinement parameter Δ_L for four different confinement lengths L_z is plotted together with the exciton diameter $d = 2r$ for excitons in different principal quantum number states $n = 2 \ldots 20$ in Fig. 7.3. The weak confinement regime holds in 2 µm wide quantum wells for Rydberg excitons in principal quantum number states up to $n = 16$, in 1.5 µm wide wells up to $n = 13$, in 1 µm wide wells up to $n = 11$, and in 500 nm wide wells up to $n = 8$. The higher the principal quantum number state, the larger the exciton, the smaller the remaining space in the quantum well and, thus, the smaller the confinement parameter Δ_L.

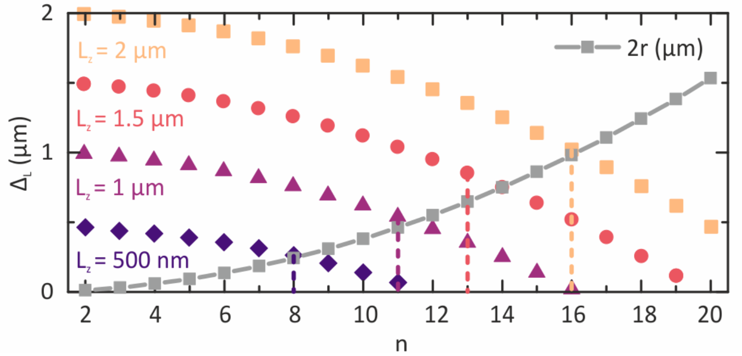

FIGURE 7.3. P-exciton diameter $d = 2r$ and confinement parameter $\Delta_L = L_z - 2r$ for four different confinement lengths L_z in dependence on the principal quantum number $n = 2 \ldots 20$.

7.3 ELECTRON STATES FOR INFINITE POTENTIAL BARRIERS

When a quantum object, such as an electron, is spatially confined in one dimension, it gains potential energy $V(z)$, which can be expressed in the Schrödinger equation as:

$$\left[-\frac{\hbar^2}{2m_e}\nabla^2 + V(z)\right]\psi(x,y,z) = E\psi(x,y,z)\,. \tag{7.4}$$

The electron wave function can be separated into

$$\psi(x,y,z) = \phi(x,y)\,\zeta(z)\,, \tag{7.5}$$

which allows for solving the Schrödinger equation via the separation ansatz:

$$-\frac{\hbar^2}{2m_e}\nabla_\perp^2\phi(x,y) = E_\perp\phi(x,y) \tag{7.6a}$$

$$\left[-\frac{\hbar^2}{2m_e}\frac{\partial^2}{\partial z^2} + V(z)\right]\zeta(z) = E_z\zeta(z)\,. \tag{7.6b}$$

Eq. (7.6a) yields the particle kinetic energy $E_\perp$, while Eq. (7.6b) determines the particle's quantized energy eigenvalues E_z due to the quantum confinement:

$$E_\perp = \frac{\hbar^2\left(k_x^2 + k_y^2\right)}{2m_e} \tag{7.7a}$$

$$E_z = \frac{\hbar^2\pi^2}{2m_e}\left(\frac{j}{L_z}\right)^2, \tag{7.7b}$$

with k_i, $i = x, y$, being the wavevector components in x and y direction, m_e the electron mass, j the quantum state index in the quantum well, and L_z the well width. The quantized bound-state energies increase with decreasing quantum well width and are proportional to the quantum state index j^2.

7.4 WEAKLY CONFINED RYDBERG EXCITONS IN CUPRITE QUANTUM WELLS

Following the calculation scheme of the previous section, we calculate the Rydberg exciton energies in a cuprite quantum well with quasi-infinite potential well barrier:

$$V_{\text{conf}} = V_0\left(z_{e,h}\right) = \begin{cases} 2.98\,\text{eV}, & |z_{e,h}| > L_z/2 \qquad (7.8\text{a}) \\ 0\,\text{eV}, & |z_{e,h}| \leq L_z/2. \qquad (7.8\text{b}) \end{cases}$$

The Hamiltonian describing this problem is given by

$$\begin{aligned} H =& -\frac{\hbar^2}{2m_e}\nabla_e^2 - \frac{\hbar^2}{2m_h}\nabla_h^2 + V_{\text{Coulomb}} + V_{\text{conf}} \\ =& -\frac{\hbar^2}{2m_e}\left(\frac{\partial^2}{\partial x_e^2} + \frac{\partial^2}{\partial y_e^2} + \frac{\partial^2}{\partial z_e^2}\right) - \frac{\hbar^2}{2m_h}\left(\frac{\partial^2}{\partial x_h^2} + \frac{\partial^2}{\partial y_h^2} + \frac{\partial^2}{\partial z_h^2}\right) \qquad (7.9) \\ & - \frac{e^2}{\varepsilon_0|r_e - r_h|} + V_0\left(z_{e,h}\right), \end{aligned}$$

with x_e, y_e, z_e (x_h, y_h, z_h) being the spatial coordinates of the electron (hole), r_e and r_h being the relative coordinate of electron and hole, and, m_e and m_h being the electron and hole mass, respectively. Separating the Hamiltonian into

$$\begin{aligned} H =& H_\perp + H_z \\ =& \overbrace{-\frac{\hbar^2}{2m_e}\left(\frac{\partial^2}{\partial x_e^2} + \frac{\partial^2}{\partial y_e^2}\right) - \frac{\hbar^2}{2m_h}\left(\frac{\partial^2}{\partial x_h^2} + \frac{\partial^2}{\partial y_h^2}\right) - \frac{e^2}{\varepsilon_0|r_e - r_h|}}^{H_\perp} \qquad (7.10) \\ & \underbrace{-\frac{\hbar^2}{2m_e}\frac{\partial^2}{\partial z_e^2} - \frac{\hbar^2}{2m_h}\frac{\partial^2}{\partial z_h^2} + V_0\left(z_{e,h}\right)}_{H_z}, \end{aligned}$$

and applying it to the separated exciton wave function (Eq. (2.18)), with $e^{i\boldsymbol{KR}} = e^{i\left(K_\perp R_\perp + k_z z\right)}$, yields a series of bound exciton lines at energies:

$$E_n^{3D,Q} = E_g - \frac{Ry^*}{\left(n - \delta_l\right)^2} + \frac{\hbar^2 \pi^2}{2m_r} \left(\frac{j}{L_z}\right)^2 . \tag{7.11}$$

E_g is the bandgap energy, Ry^* the modified Rydberg energy, n the principal quantum number, δ_l the quantum defect, and m_r the relative electron-hole mass. The additional quantized energy term,

$$\Delta_{\text{conf}} = \frac{\hbar^2 \pi^2 j^2}{2m_r L_z^2} = \frac{\hbar^2 \pi^2 j^2}{2m_r \left(\Delta_L + 2r\right)^2}, \tag{7.12}$$

arises due to the quantum confinement along one dimension. This quantum confinement causes an increase in potential energy of the confined Rydberg exciton dependent on the quantum object mass m_r, the confinement quantum state j, the well width L_z or the confinement parameter Δ_L, and the quantum object radius r.

We show in Fig. 7.4 (a) and (b) the calculated energy blue-shifts Δ_{conf}, experienced by Rydberg excitons in cuprite quantum wells, for the lowest and third excited quantum states, $j = 1$ and $j = 3$, respectively, and, for four different well widths $L_z \in \{0.5; 1; 1.5; 2\}$ µm. The data are only displayed for the weak confinement regime, which applies for Rydberg excitons with up to a different principal quantum number n for different quantum well sizes L_z (see Fig. 7.3). For both the lowest ($j = 1$) and third excited ($j = 3$) quantum state index, and for all different well widths L_z shown here, the energy shift Δ_{conf} increases with increasing principal quantum number n. This increase in energy is absolutely larger and steeper the smaller the well widths. For the lowest quantum state index $j = 1$, Δ_{conf} accounts for up to 14 µeV, while for the third excited quantum state index $j = 3$ Δ_{conf} reaches values of up to 140 µeV, which is one order of magnitude larger.

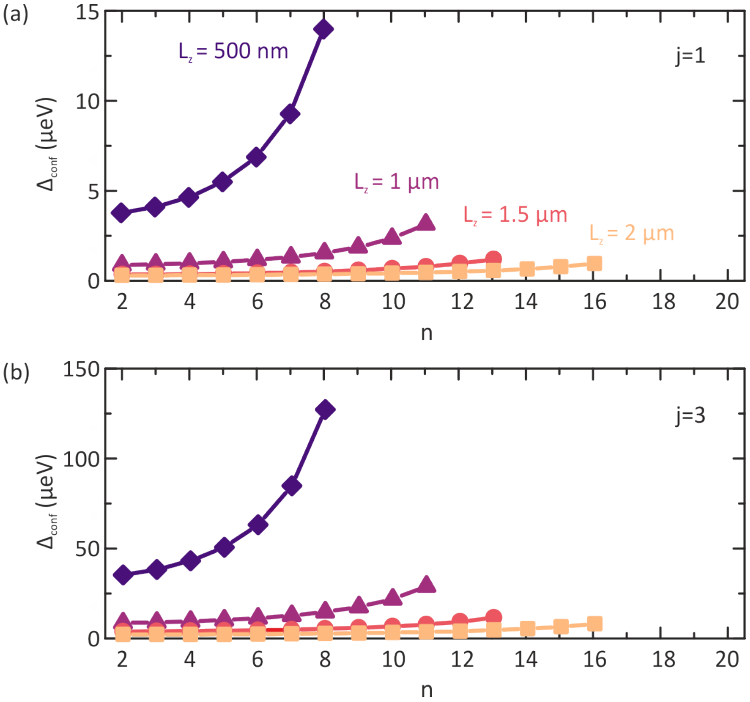

FIGURE 7.4. (a) Rydberg exciton energy gain Δ_{conf} due to the quantum confinement for the lowest excited quantum state $j = 1$. (b) The same as in (a) but for quantum state $j = 3$. Data are only shown for the weak confinement. The lines are guides to the eye.

Quantum confinement inhibits free motion and, thus, influences the kinetic energy of the quantum object. Only discrete values are allowed, leading to a series of quantized states [93]. Confined to a quantum well, Rydberg excitons gain energy, so they experience an energy blue-shift. Within the weak confinement regime, this energy shift accounts for a few and a few tens of µeV for the lowest and third excited quantum state index, respectively. The energy shifts are controllable via the three parameters principal quantum number n, quantum state index in the quantum well j, and quantum well width L_z over a wide range. Such controllable energy shift could be used for realizing quantum technologies using Rydberg excitons in cuprous oxide [187]. In order to enlarge the range over which the energy can be shifted, one could go to higher confinements, meaning a more tight confinement along one dimension (intermediate or strong confinement regime in 2D), or to a confinement along two or three dimensions.

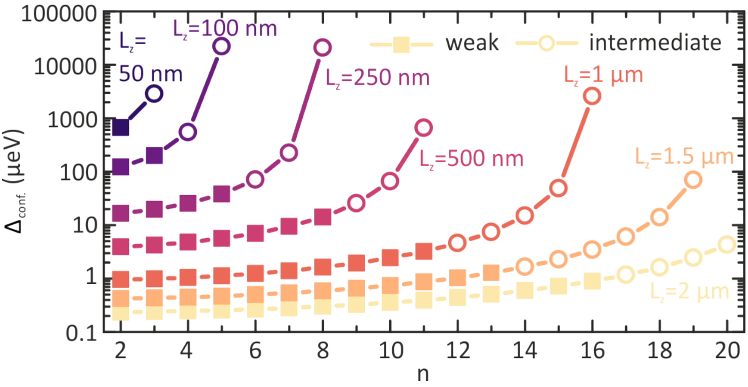

Figure 7.5. Rydberg exciton energy shifts in μeV due to quantum confinement Δ_{conf} for the lowest quantum state index $j = 1$, for weak ($L_z \geq 4r$) and intermediate ($2r < L_z < 4r$) regimes. The energy shifts are shown in dependence on the principal quantum number n and for seven different well widths L_z.

The conditions for the strong confinement regime become more complicated. Strictly speaking, for a very strong exciton confinement, electron and hole become quantized separately, so the quantization energy dominates over the Coulomb interaction energy and we cannot speak of an exciton any more. In order to get a first estimation for how the energy shifts would develop when going towards the intermediate regime ($2r < L_z < 4r$), we apply the weak confinement model to excitons in this intermediate confinement. The resulting energy blue-shifts Δ_{conf} are shown in Fig. 7.5 for the lowest quantum state index $j = 1$, for different well widths L_z, and in dependence on the principal quantum number n. The transition from weak to intermediate regime is smooth. As expected, the energy blue-shifts become significantly larger the narrower the quantum wells are, and account for up to several tens of meV.

7.5 STRONGLY CONFINED RYDBERG EXCITONS IN CUPRITE QUANTUM WELLS

In the strong confinement regime, the confinement energy exceeds the exciton binding energy. In this case, electron and hole are confined separately in their respective confinement potentials. In the strict 2D limit, the exciton binding energy changes. The 3D Rydberg P-exciton energy is given by Eq. (2.20) as

$$E_n^{3D,p} = E_g + E_B^* = E_g - \frac{Ry^*}{\left(n - \delta_l\right)^2}. \tag{7.13}$$

In strictly two dimensions, the Rydberg exciton binding energy E_B^* becomes modified to [188]

$$E_B^{2D} = -\frac{Ry^*}{\left(n - 1/2\right)^2}. \tag{7.14}$$

This implies that the lowest 2D exciton energy ($n = 1$) has a magnitude four times larger than the 3D exciton ground state, when neglecting the quantum defect δ_l: $E_{B,n=1}^{2D} = -4Ry^*$. Thus, the exciton ground state is farther away from the bandgap in 2D, and the 2D Bohr radius is half as big as the 3D one. The excitonic resonances as well as the exciton binding energies are stronger in 2D. The transition from 3D to 2D would cause exciton energy shifts of a few meV:

$$\begin{aligned} \Delta^{2D} &= E_n^{2D} - E_n^{3D,P} = E_g + E_B^{2D} - \left(E_g + E_B^*\right) = E_B^{2D} - E_B^* \\ &= \frac{Ry^*}{\left(n - \delta_l\right)^2} - \frac{Ry^*}{\left(n - 1/2\right)^2} < 0. \end{aligned} \tag{7.15}$$

The absolute value of the exciton binding energy in three dimensions decreases rapidly with increasing n. So does the absolute value of the binding energy in two dimensions, too, however, at some larger values. Their difference, defined as the energy shift Δ^{2D}, thus, follows the same trend. Note that, as the binding energy is negative, an absolutely larger Rydberg binding energy implies a smaller Rydberg exciton energy (see Eq. (7.13)). Therefore, the effect the 2D confinement will have on the total exciton energy, will be a red-shift towards lower energies. These results are visualized in Fig. 7.6.

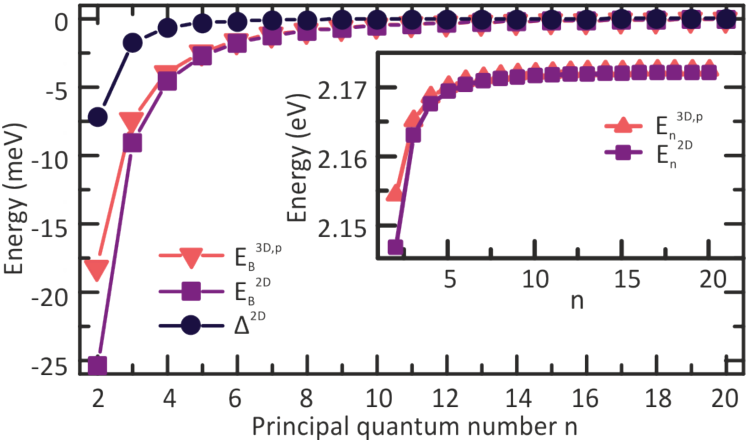

FIGURE 7.6. Energy shift $\Delta^{2D} = E_B^{2D} - E_B^{3D,p}$ that an exciton experiences when being squeezed into two dimensions together with the exciton binding energies $E_B^{3D,p} = E_B^*$ and E_B^{2D} in three and two dimensions, respectively. The inset shows the Rydberg exciton energies $E_n^{3D,p} = E_g + E_B^{3D,p}$ and $E_n^{2D} = E_g + E_B^{2D}$. The lines are guides to the eye.

An exciton's total energy shift inside a quantum well is:

$$\begin{aligned}\Delta^{\text{tot}} &= E_n^{2D,Q} - E_n^{3D,p} \\ &= \left(E_g + E_B^{2D} + \Delta_{\text{conf}}\right) - \left(E_g + E_B^{3D,p}\right) \\ &= \Delta_{\text{conf}} + \Delta^{2D}.\end{aligned} \tag{7.16}$$

It will change from red- to blue-shifting with increasing principal quantum number n. The transition depends on the confinement strength (well width L_z). This is shown in Fig. 7.7 for the third excited quantum level ($j = 3$) for four different well widths $L_z \in \{0.5, 1, 1.5, 2\}$ µm.

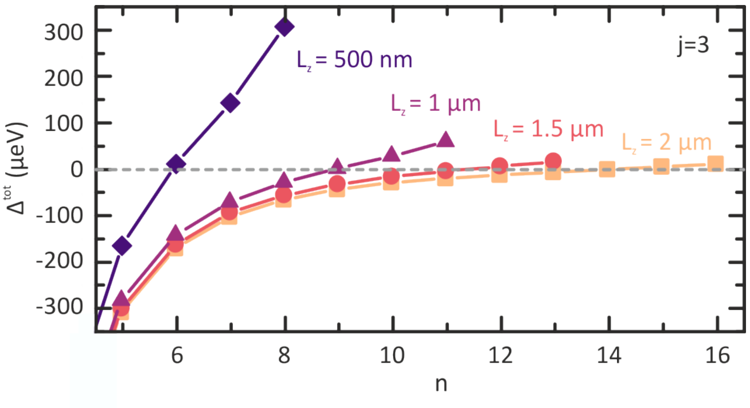

FIGURE 7.7. Total energy shifts $\Delta^{\text{tot}} = E_n^{2D,Q} - E_n^{3D,p}$ for the third excited quantum level $j = 3$, for four different well widths $L_z \in \{0.5, 1, 1.5, 2\}$ µm in dependence on the principal quantum number n.

For a very narrow quantum well, the permittivity of the surrounding material outside the quantum well will have an influence, too. The Coulomb interaction between electron and hole in an exciton is of three-dimensional character and, thus, not squeezed inside the well, but occurs primarily outside the well with less effective screening (see Fig. 7.8) [189]. The binding energy then becomes:

$$E_B^{2D^*} = -\left(\frac{2\varepsilon}{\varepsilon_I + \varepsilon_{III}}\right)^2 \frac{Ry^*}{(n-1/2)^2}, \tag{7.17}$$

with cuprous oxide permittivity $\varepsilon = 9.8$ and air permittivity $\varepsilon_I = \varepsilon_{III} = 1$, surrounding the narrow well structure. This implies an increase in binding energy of almost two orders of magnitude:

$$\left(\frac{2\varepsilon}{\varepsilon_I + \varepsilon_{III}}\right)^2 = \left(\frac{2 \cdot 9.8}{2}\right)^2 = (9.8)^2 = 96.04 \approx 10^2. \tag{7.18}$$

In the strong confinement regime, electron and hole confinement energies would exceed the exciton binding energy.

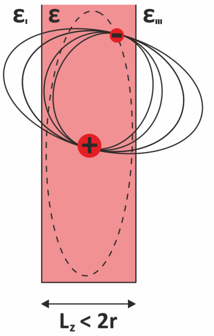

FIGURE 7.8. Schematic drawing of an exciton strongly confined inside a narrow quantum well. The Coulomb interaction between electron and hole occurs primarily outside the well with less effective screening.

Higher quantum confinements can also be reached by confining a quantum object in two or three dimensions. This can be realized by confining Rydberg excitons into cuprite quantum wires or quantum dots. In such structures the energy shift caused by the confinement geometry reads:

$$\Delta_{\text{conf}}^{1D} = \frac{\hbar^2 \pi^2}{2m_r} \left(\frac{j_z^2}{L_z^2} + \frac{j_y^2}{L_y^2} \right) \overset{L_z = L_y}{\longrightarrow} 2 \cdot \Delta_{\text{conf}}^{2D} \tag{7.19}$$

$$\Delta_{\text{conf}}^{0D} = \frac{\hbar^2 \pi^2}{2m_r} \left(\frac{j_z^2}{L_z^2} + \frac{j_y^2}{L_y^2} + \frac{j_x^2}{L_x^2} \right) \overset{L_z = L_y = L_x}{\longrightarrow} 3 \cdot \Delta_{\text{conf}}^{2D}. \tag{7.20}$$

The blue-shift could, thus, be enhanced by a factor of 2 and 3 compared to the quantum well structures. It remains, however, unknown, how the Rydberg binding energy would change in such structures.

7.6 SUMMARY AND OUTLOOK

We performed first steps towards calculating the energy shifts of confined Rydberg excitons in Cu_2O quantum wells. The macroscopic size of Rydberg excitons with high quantum numbers n implies that already µm-sized lamellar, wire-like, or box-like structures lead to quantum size effects, which depend on the principal Rydberg quantum number n. Such structures can straightforwardly be fabricated using focused ion beam milling (see Fig. 3.12 in Section 3.7.2).

Quantum confinement causes an energy shift as a series of discrete bound states. This size-dependent radiative coupling of the Rydberg excitons is interesting for quantum technologies based on cuprous oxide as it allows for tailoring optical properties in a well controllable environment [174, 190]. Furthermore, the exploitation of large nonlinearities for quantum applications can be promoted by quantum confinement of Rydberg excitons [176]. We find in our calculations that the Rydberg excitons gain a potential energy Δ_{conf}

in the μeV range due to the quantum confinement. At the same time the exciton energy suffers some loss Δ^{2D} in the meV range due to an increased binding energy that occurs for two-dimensional excitons. Only in the very limit of the weak confinement regime, the potential energy gain starts to dominate. Both effects are dependent on the Rydberg exciton size and, thus, the principal quantum number n. The calculated energy shifts in the μeV to meV energy range should be experimentally accessible and detectable.

In the above ansatz, we only indirectly take into account the relative size ratio between confinement size and exciton Bohr radius for different quantum numbers n. Furthermore, the Coulomb interaction between electron and hole occurs primarily through the medium outside the well with less effective screening, which is not included in our calculations. Last, we have not treated an interpolation between the limits of weak and strong confinement. More detailed calculations of the optical functions of Rydberg exciton-polaritons in cuprous oxide have been performed recently for quantum well structures [191], confirming that a blue-shift in the optical spectra is an evidence of the quantum confinement effect. It has been shown that the calculated spectra of all low-dimensional systems exhibit a smooth transition to the bulk absorption in the limit of large nanostructures.

We are convinced that the present study will trigger further interest into this topic. Owing to their giant microscopic dimensions (1 μm) leading to the onset of the exciton blockade, Rydberg excitons in cuprous oxide exhibit enhanced optical nonlinearities at much smaller densities compared with other traditional semiconductors [15, 24]. Highly excited Rydberg states with large Bohr radii and a relative motion exceeding the light wavelength provide a unique opportunity to observe size-dependent enhancement of the nonlocal optical response [174]. Mesoscopic confinements are on the order of several micrometers, which are experimentally feasible sizes. The complex dynamics and enhanced nonlinear properties of systems containing Rydberg excitons indicate that Cu_2O might become one of the most versatile, scalable and tunable platforms for quantum computing technologies. Studying Cu_2O Rydberg excitons in confined dimensions presents a crucial step towards Rydberg polaritonics in the quantum regime [48, 176] and exploiting Rydberg excitons for high refractive optical nonlinearities (self-Kerr effect) [192], as well as even harnessing these nonlinearities for quantum applications, such as single-photon sources [193] and single-photon switches [70].

A

AUSFÜHRLICHE ZUSAMMENFASSUNG

Halbleiter sind sowohl in der Grundlagenforschung als auch in der angewandten Physik seit langer Zeit von großem Interesse. Eine fundamentale Anregung im Halbleiter bildet das Exziton, ein gebundener Zustand von Elektron und Loch. Exzitonen wurden in den 1930er Jahren theoretisch vorhergesagt [1, 2] und zwanzig Jahre später im Halbleiter Kupferoxydul (Cu_2O) experimentell nachgewiesen [3, 4]. Ab den 1970er Jahren wurde an diesen Quasiteilchen intensiver geforscht [5–8]. Hierbei wurde die Feinstruktur der Exzitonenzustände im Kupferoxydul nicht nur experimentell untersucht, z.B. durch Anlegen externer Felder [11] oder in Zwei-Photonen-Experimenten [12], sondern auch theoretisch beschrieben [9, 13, 14].

Kupferoxydul hat insgesamt zehn Valenz- und vier Leitungsbänder, sowie eine direkte Bandlücke ($E_g = 2.17\,\mathrm{eV}$). In dieser Arbeit liegt der Fokus auf Exzitonen, die sich zwischen dem höchsten Valenz und dem niedrigsten Leitungsband bilden. Da diese Bänder die gleiche positive Parität haben, verschwindet das Dipolmoment und die Lebenszeiten der mit dipolarem Licht anregbaren P-Exzitonen sind relativ lang. Während die maximal anregbare Hauptquantenzahl der Exzitonen in Kupferoxydul lange Zeit bei nur $n = 7$ lag, lebte das Forschungsinteresse wieder auf, als man 2014 P-Exzitonen mit Hauptquantenzahlen bis zu $n = 25$ nachwies [15]. Diese hochangeregten Exzitonen wurden fortan *Rydbergexzitonen* genannt, in Analogie zum Rydbergzustand eines Atoms.

Rydbergexzitonen haben große Ähnlichkeit mit Rydbergatomen. Letztere besitzen ein hochangeregtes Valenzelektron, wodurch sie sich aufgrund ihrer daraus resultierenden enormen Größe und hoher Sensibilität gegenüber äußerer Einwirkungen von Atomen im Grundzustand grundlegend unterscheiden. Rydbergatome fungieren als wichtiges, hochsensibles Messinstrument für die feinen Prozesse der Quantenphysik, wie z.B. als optische Sensoren [16] oder Gasdetektoren [17]. Darüber hinaus werden Rydbergatome auch als Bausteine für Quantencomputer eingesetzt [64, 74, 76, 79, 80]. Im Gegensatz zu Rydbergatomen sind Rydbergexzitonen direkt in einem Halbleiter eingebettet. In Kupferoyxdul liegen die Bohrradien für Hauptquantenzahlen um $n = 20$ schon im µm-Bereich. Die damit vorliegenden Gegebenheiten eines makroskopischen Quantensystems erleichtern die Verwirklichung von integrierbaren, skalierbaren Festkörper-Quantentechnologien.

Ähnlichkeiten und Unterschiede zwischen Rydbergexzitonen und Rydbergatomen wurden in den letzten Jahren intensiv experimentell [15, 24, 26], sowie auch theoretisch [21, 25, 27, 29–31] untersucht. Hierbei wurde der Fokus auch auf festkörperspezifische Effekte gelegt, wie die phononenassistierte Absorption [32] und das Elektronen-Loch-Plasma [33, 34]. Drehimpulslicht [45] und Zweite-Harmonische-Erzeugung wurde genutzt um dipolverbotene Exzitonen mit ungerader Parität bis $n = 12$ experimentell nachzuweisen [35–37], sowie auch theoretisch zu beschreiben [39, 40]. Rydbergexzitonen in Potenzialtöpfen [41–43] und in Mikrokristallen [44], sowie auch Rydbergexziton-Polaritonen in Mikrokavitäten [48] wurden untersucht. Unlängst wurden mittels Transmissions- und Photolumineszenz-Emissions-Messungen sogar Rydbergexzitonen mit Hauptquantenzahlen bis $n = 30$ nachgewiesen [47, 194], und über Pump-Probe-Spektroskopie wurde herausgefunden, dass Ladungsstörstellen der limitierende Faktor für die Existenz von Rydbergexzitonen mit noch höheren Hauptquantenzahlen $n > 25$ sind [46, 47].

Die Schlüsselvoraussetzung für alle oben genannten Experimente ist die Verfügbarkeit von Kristallen hoher Qualität und extremer Reinheit. Die experimentellen Untersuchungen werden bei tiefkalten Temperaturen durchgeführt, um den Phononenhintergrund im Halbleiterkristall zu unterdrücken und somit die Exzitonensignale sichtbar zu machen. In der vorliegenden Arbeit wird hierfür ein Kryostat von Oxford Instruments verwendet, mit dem die Probe auf 1.5 K gekühlt werden kann. Zudem verfügt der Kryostat über optische Zugänge an allen vier Seiten. Die Probe wird auf einem Probenstab befestigt der ±15 mm entlang seiner Längsachse bewegt und um 360° gedreht werden kann. Für integrierte Anwendungen werden 3D gedruckte Mikrooptiken, diffraktive optische Elemente hoher Qualität, sowie plasmonische Antennen benötigt.

Spektroskopische Untersuchungen setzten eine geeignete Lichtquelle, sowie präzise Detektion voraus. Die Exzitonenserie im Kupferoxydul wird mithilfe eines durchstimmbaren Lasers (574.67 nm – 570.84 nm oder 2.1575 eV – 2.1720 eV) untersucht. Für Pump-Probe Spektroskopie wird ein weiterer Laser bei 561 nm (2.21 eV) zum Pumpen verwendet. Die Laser werden auf einen Durchmesser von zehn bis mehrere 100 µm auf die Probe fokussiert und das kollimierte Signal wird in Transmission oder Reflektion mittels Photodioden detektiert, welches bei Pump-Probe Spektroskopie an einen Lock-In Verstärker weitergeleitet wird. Wenn nötig, wird ein Referenzsignal aufgenommen um Interferenzen zu kompensieren. Für konstante Laserintensität während eines Scans, werden die Lichtstrahlen mit einem Leistungsregler stabilisiert. Abschwächung wird mit der Kombination von $\lambda/2$-Platte und Glan-Taylor Prisma erreicht. Die Daten werden von einem Oszilloskop oder Hochgeschwindigkeitsmultimeter, welche mit einem Computer verbunden sind, ausgelesen und mittels geeigneter Software ausgewertet.

RYDBERGEXZITONEN IN KUPFEROXYDUL: ÄNDERUNG DER DIPOLAUSWAHLREGELN MITTELS DREHIMPULSLICHT

Der erste Teil dieser Dissertation befasst sich mit der Frage, wie die Dipolauswahlregeln bei Rydbergexzitonen in Kupferoxydul mithilfe von Bahndrehimpulslicht verändert werden können. Atomare Übergänge können getrieben werden, wenn der Überlapp von Grund- und angeregtem Zustand die Symmetry des Lichtfeldoperators enthält. Die komplette Wechselwirkung von Licht mit Materie wird durch die Multipolentwicklung des elektromagnetischen Feldes gekoppelt an die Momente der atomaren Ladungsverteilung beschrieben. Während das elektrische Dipolmoment mit der elektrischen Feldamplitude koppelt, wechselwirkt das Quadrupolmoment mit deren Feldgradienten. Der longitudinale Feldgradient in Dipollicht ist jedoch sehr schwach. Hingegen kann ein transversaler Feldgradient, wie z.B. durch die örtliche Struktur des Strahlquerschnitts in Bahndrehimpulslicht gegeben, einen Quadrupolübergang sehr viel effektiver treiben [119, 120, 122, 123, 163, 164]. Atome müssen dazu exakt im Zentrum des Bahndrehimpulslichtstrahls plaziert, und letzterer muss bis zum Beugungslimit fokussiert werden [118]. Für die Anregung von Rydbergexzitonen in Kupferoxydul ist deren Größe (hunderte Nanometer bis einige Mikrometer) von Vorteil und garantiert großen Überlapp mit dem fokussierten Drehimpulslichtstrahl [165]. Die räumliche Mode des Bahndrehimpulslichts kann dann aufgrund von Drehimpulserhaltung (Phasenerhaltung) auf den Exzitonenzustand übertragen werden. Die folgenden Ergebnisse wurden in Ref. [45] veröffentlicht.

Unser Ziel ist es vorherzusagen ob ein optischer Übergang zwischen dem Grundzustand des Kristalls und Exzitonenzuständen mit unterschiedlicher Bahndrehimpulsquantenzahl (l^{exc}) erlaubt oder verboten sind, wenn sie mit Bahndrehimpulslicht ($l = 0, 1, 2, 3$)

angeregt werden. Dazu muss zum einen berechnet werden, welche Symmetrien Exzitonen mit unterschiedlicher Bahndrehimpulsquantenzahl in Kupferoxydul haben, und zum anderen, wie sich die Symmetrie von Bahndrehimpulslicht in der Kristallumgebung (O_h Punktsymmetrie) verhält.

Die Symmetrien der Exzitonenzustände werden von den Cu_2O-Bandsymmetrien abgeleitet. Da die Anregung innerhalb des Kristalls stattfindet, nutzen wir die Tabellen von Koster [88] um die Symmetrien des Bahndrehimpulslichts innerhalb der Symmetriegruppe von Kupferoxydul (O_h) zu bestimmen. Zunächst betrachten wir, wie sich die Koordinatenfunktionen der verschiedenen Objekte, also von Licht und Exziton, in Bezug auf die verschiedenen O_h-Symmetrieoperationen ändern. Die Koordinatenfunktionen bilden die Basisfunktionen der irreduziblen Repräsentationen innerhalb einer bestimmten Punktgruppe. Hiervon ausgehend leiten wir reduzible Darstellungen der Objekte her und zerlegen sie wiederum in irreduzible Darstellungen, wodruch wir die komplette Symmetrie der Objekte erhalten. Zuletzt vergleichen wir die Symmetrien von Bahndrehimpulslicht und Exzitonen.

Tabelle A.1. Symmetrien von Dipol- und Quadrupolübergangsoperator von Bahndrehimpulslicht ($l = 0 \dots 4$).

l	Dipol	Quadrupol
0 (gerade)	Γ_4^-	$\Gamma_3^+ + \Gamma_5^+$
1 (ungerade)	$\Gamma_1^+ + \Gamma_2^+ + 2\Gamma_3^+ + 2\Gamma_4^+ + 2\Gamma_5^+$	$\Gamma_1^- + \Gamma_2^- + 2\Gamma_3^- + 4\Gamma_4^- + 4\Gamma_5^-$
2 (gerade)	$\Gamma_2^- + \Gamma_3^- + 2\Gamma_4^- + 3\Gamma_5^-$	$2\Gamma_1^+ + \Gamma_2^+ + 3\Gamma_3^+ + 4\Gamma_4^+ + 3\Gamma_5^+$
3 (ungerade)	$\Gamma_1^+ + \Gamma_2^+ + 2\Gamma_3^+ + 2\Gamma_4^+ + 2\Gamma_5^+$	$\Gamma_1^- + \Gamma_2^- + 2\Gamma_3^- + 4\Gamma_4^- + 4\Gamma_5^-$
4 (gerade)	$\Gamma_1^- + \Gamma_3^- + 3\Gamma_4^- + 2\Gamma_5^-$	$\Gamma_1^+ + 2\Gamma_2^+ + 3\Gamma_3^+ + 3\Gamma_4^+ + 4\Gamma_5^+$

In Tabelle A.1 sehen wir, dass Bahndrehimpulslicht mit $l = 1$ und $l = 3$ die gleiche Symmetrie besitzen. Wenn der Dipol-Lichtfeldoperator positive Parität besitzt, hat der dazugehörigen Quadrupol-Lichtfeldoperator negative Parität, und umgekehrt. Für sukzessives Erhöhen der Drehimpulsquantenzahl l, ändert sich die Parität alternierend. Wenn Kupferoxydul mit einem Gaußstrahl ($l = 0$) angeregt wird, sehen wir P-Exzitonen im Absorptionsspektrum. Gemäß unseren Berechnungen sind P-Exzitonen auch als Quadrupolübergänge mit $l = 1$ oder $l = 3$ Bahndrehimpulslicht anregbar. Im Gegensatz dazu, können die sonst Dipol-verbotenen S-Exzitonen nicht nur als Quadupolübergänge von Bahndrehimpulslicht mit gerader Drehimpulsquantenzahl ($l = 0, 2, 4$) sondern auch als Dipolübergäne von Bahndrehimpulslicht mit ungerader Drehimpulsquantenzahl ($l = 1, 3$) angeregt werden. Das gleiche gilt auch für D- und G-Exzitonen, während F- und H-Exzitonen den Auswahlregeln von P-Exzitonen entsprechen. Die Ergebnisse sind in Tabelle A.2 zusammengefasst.

TABELLE A.2. Gesamte Exzitonenübergangssymmetrie $\varGamma_{\text{exc}}$ für verschiedene Einhüllende l^{exc}, deren Parität (+/-), und Dipol- sowie Quadrupollichtfeld mit unterschiedlichem Bahndrehimpuls l^{Dipol} / $l^{\text{Quadrupol}}$ (gerade / ungerade), mit dem der Übergang angeregt werden kann.

l^{exc}	$\varGamma_{\text{exc}}$	Parität	l^{Dipol}	$l^{\text{Quadrupol}}$
S	$\varGamma_2^+ + \varGamma_5^+$	+	ungerade	gerade
P	$\varGamma_2^- + \varGamma_3^- + \varGamma_4^- + 2\varGamma_5^-$	-	gerade	ungerade
D	$\varGamma_1^+ + 2\varGamma_3^+ + 3\varGamma_4^+ + \varGamma_5^+$	+	ungerade	gerade
F	$2\varGamma_1^- + \varGamma_2^- + 2\varGamma_3^- + 4\varGamma_4^- + 3\varGamma_5^-$	-	gerade	ungerade
G	$\varGamma_1^+ + 2\varGamma_2^+ + 3\varGamma_3^+ + 4\varGamma_4^+ + 5\varGamma_5^+$	+	ungerade	gerade
H	$\varGamma_1^- + 2\varGamma_2^- + 4\varGamma_3^- + 5\varGamma_4^- + 6\varGamma_5^-$	-	gerade	ungerade

Bahndrehimpulslicht kann erzeugt werden, indem man einer ebenen Welle oder Gaußmode eine räumlich variierende Phasenverzögerung, durch z.B. eine spirale Phasenplatte, aufprägt. Dadurch entsteht eine Laguerre-Gaussmode. Solche spiralen Phasenplatten wurden mit 3D-Laserdruck direkt auf die Kupferoxyduloberfläche aufgebracht und mit einem fokussierten Laserstrahl bestrahlt. Somit konnte unsere theoretische Vorhersage einer Verstärkung der

Quadrupolübergänge von Cu_2O Rydbergexzitonen durch Anregung mit Bahndrehimpulslicht auch experimentell bestätigt werden.

Bahndrehimpulslicht ist ein ideales Werkzeug um gezielt dipolverbotene Zustände in linearer Ein-Photonen-Absorption anzuregen. Insbesondere sind Rydbergexzitonen in Kupferoxydul aufgrund ihrer makroskopischen Größe eine vielversprechende Plattform um Wechselwirkungen zwischen Bahndrehimpulslicht und Materie zu testen. Ein effizienter Bahndrehimpulsaustausch zwischen Licht und elementaren Anregungen in Festkörpersystemen könnte den Grundstein für neue Festkörperbauteile in Bezug auf Quantentechnologien darstellen [170]. Des Weiteren erlauben die neuen Auswahlregeln für Bahndrehimpulslicht nicht nur das Freilegen verbotener Anregungen von Rydbergexzitonen in Kupferoxydul, sondern auch die Anwendung neuer spektroskopischer Techniken in einer Vielzahl physikalischer Systeme [169]. Die Möglichkeit von Bahndrehimpulslicht, Übergänge jenseits des Dipollimits anzuregen, stellt eine aufregende mögliche Anwendung für Quanteninformation dar [171].

VERSTÄRKUNG VON QUADRUPOLÜBERGÄNGEN IN Cu_2O EXZITONEN MITTELS PLASMONISCHER ANTENNEN

Im zweiten Teil der vorliegenden Arbeit wird gezeigt, dass Quadrupolübergänge in Rydbergexzitonen in Kupferoxydul auch durch Kopplung an plasmonische Antennen verstärkt werden können. Der Inhalt dieses Kapitels wurde zur Veröffentlichung bei Physical Review B eingereicht (31.08.2022).

Inspiriert von den theoretischen und experimentellen Untersuchungen mit Bahndrehimpulslicht, haben wir nach einer zweiten Methode gesucht, wie Exzitonenzustände mit verschiedenen Bahndrehimpulsquantenzahlen angeregt werden können. Nicht nur der transversale Feldgradient in Bahndrehimpulslicht, sondern auch jener in Hotspots von plasmonischen Antennen, kann Quadrupolübergänge treiben. Plasmonische Antennen sammeln eingestrahlte elektromagnetische Energie in einem komprimierten Nahfeld. Dies resultiert in einer ungleichmäßigen Feldlinienverteilung an den Antennenkanten – wie bei einem Dipol – und geht mit starken transversalen Feldgradienten einher. Plasmonischen Antennen können mit Hilfe von Elektronenstrahllithographie direkt auf der polierte Oberfläche eines Kupferoxydulkristalls aufgebracht werden.
Eine große Vielfalt an Exzitonenzuständen mit unterschiedlicher Bahndrehimpulsquantenzahl anzuregen ist interessant für optisches Schalten in Quantenanwendungen. Insbesondere ist es dann wichtig, an- und ausschalten zu können. Dies wird dadurch erreicht, dass die Antennen so konzipiert sind, dass die Plasmonenresonanz nur in einer bestimmten Polarisationsrichtung (parallel) aktiv ist, während sie in der anderen (senkrecht) inaktiv ist. Durch Variieren der Antennenlänge kann die Plasmonenresonanz durchgestimmt werden kann. Des Weiteren ist die Größe von Rydbergexzitonen in Kupferoxydul vergleichbar mit der Ausdehnung des plasmonischen Feldgradienten. Dies bedeutet, dass die Rydbergexzitonen mit dem gesamten optischen Lichtfeld wechselwirken, was zu einer weiteren Verstärkung des Quadrupolübergangs führen sollte.

Wir konnten mittels Pump-Probe-Spektroskopie in Reflektionsgeometrie zeigen, dass bei paralleler Laserpolarisation (aktive Plasmonenresonanz) das 6S-Exziton auf einem Antennenfeld auftaucht, während es auf einem Referenzfeld abwesend bleibt. Des Weiteren konnten wir zeigen, dass 5S- und 6S-Exzitonen bei Messungen mit paralleler Laserpolarisation auf Antennenfeldern auftauchen, während sie bei senkrechter Laserpolarisation auf Antennenfeldern abwesend sind. Jedoch trat diese Quadrupolverstärkungen nur mit

einen kleinen Faktor von maximal 1.4 auf.
Gründe hierfür wären, dass die Kopplung der Rydbergexzitonen mit den plasmonischen Antennen nicht optimal war. Diese könnte durch Lokalisieren der Rydbergexzitonen in *strain traps* [20] verstärkt werden. Außerdem könnten durch die plasmonische Feldverstärkung (Faktor 1000) Ladungsverteilungen erzeugt worden sein, die gemäß des *purifying effects* [47] die Ladungsverteilung der Rydbergexzitonen abgeschwächt haben könnte. Simulationen könnten hier helfen, um den genauen Einfluss der verschiedenen Faktoren zu bestimmen. Des Weiteren könnte man den Kristall zu ultradünnen Plättchen mit Dicken kleiner als 10 µm polieren und mit Transmissionsspektroskopie vermessen. Transmittierte Exzitonsignale sind leichter zu messen und zu interpretieren, würden jedoch auch einen gewissen Anteil der Dipolanregung beinhalten, da nun auch der Beitrag aus dem Inneren des Kristalls gemessen würde und die Antennen nur auf der Oberfläche Einfluss nehmen. Der Dipolbeitrag wäre jedoch um einiges geringer als bei den bisherigen Messungen. Zuletzt könnten auch Cu_2O-Mikrokristalle zwischen plasmonischen Antennen verteilt und gemessen werden. Hier würde das plasmonische Gradientenfeld den gesamten Kristall ausfüllen. Allerdings würden auch Randeffekte auftreten, die Vieles verkomplizieren würden. Gleichwohl ist die erfolgreiche Umsetzung von Reflektionsmessungen an Kupferoxydul ein erster Schritt in Richtung eines Quanten-integrierten, Faser-gekoppelten Detektionskonzepts mit Rydbergexzitonen.

RYDBERGEXZITONEN IN QUANTENTÖPFEN

Der dritten Teil der Doktorarbeit befasst sich mit Rydbergexzitonen in Quantentöpfen. Das Konzept dieses Problems ist allseits bekannt. Die Beschreibung erfolgt über Potentialtopfberechnungen, welche schon ausführlich an Elektronen und Löchern in Halbleitern durchgeführt wurde [185]. Dennoch wurde speziell das Verhalten von

Rydbergexzitonen in Quantentöpfen noch nicht untersucht. Der folgende Inhalt wurde in Ref. [43] veröffentlicht.

Quanteneffekte treten auf, sobald die räumliche Begrenzung eines Objekts in Größenordnungen vergleichbar mit dem Bohrradius des Objekts liegt. Rydbergexzitonen in Cu_2O haben Bohrradien bis µm-Größe. Deshalb genügt es, sie in sogenannten mesoskopischen Strukturen – deren Größe sehr viel größer ist als die Gitterkonstante des Kristalls – einzusperren, um Quanteneffekte zu beobachten. Mesoskopische Beschränkungen in der Größenordnung von einigen µm sind schon von Quantenpunkten her bekannt [182, 183]. Die Bandstruktur eines Halbleiters in einer mesoskopischen Beschränkung wird nur leicht verändert im Vergleich zum unbeschränkten Material [184]. Diese Voraussetzung erlaubt es, nur die Änderungen in der Einhüllenden der Wellenfunktion durch das Beschränkungspotential zu untersuchen, was auch als *envelope function approximation* bekannt ist.
Des Weiteren spielen in räumlich beschränkten Strukturen auch Oberflächenpolarisationseffekte eine Rolle. Diese werden verursacht durch die unterschiedlichen Permittivitäten von Material und Umgebung, und sind gerade bei der Untersuchung von Rydbergexzitonen wichtig. Die coulombische Elektronen-Loch-Anziehung ist hier verantwortlich für die Entstehung von gebundenen Zuständen der Relativbewegung des Exzitons. Die gebundenen Exzitonenzustände in Quantentöpfen sind in vielen Aspekten den gebundenen Coloumb-Störstellen ähnlich. Dies bedeutet, dass die Relativbewegung von Elektron und Loch durch einen Hamilton-Operator beschrieben wird, der dem von Störstellen gleicht [186]. Intuitiv assoziieren wir eine zusätzliche kinetische Energie mit der Lokalisierung eines Teilchens in einer endlichen Raumregion, was damit vergleichbar ist, dass die Störstellenbindungsenergie mit abnehmender Quantentopfgröße anwächst.

Die untersuchten Quantentöpfe bestehen aus einer Kupferoxydulscheibe, die in x- und y-Richtung über viele hunderte Mikrometer bis wenige Millimeter ausgedehnt, und in z-Richtung auf wenige hunderte Nanometer beschränkt ist. Das Material ist von Luft umgeben. Da die Coulombwechselwirkung, welche die Elektron-Loch-Relativbewegung verursacht, immer von dreidimensionaler Natur und abhängig vom relativen Elektronen-Loch-Abstand ist, lässt sich normalerweise ein solches quantenmechanisches Problem aufgrund der gegebenen Geometrie nicht in Schwerpunkts- und Relativkoordinaten separieren. Für sehr große Quantentöpfe jedoch (schwache Beschränkung) wirkt die Beschränkung, oder der Störeinfluss, nur auf die Schwerpunktskoordinate, also auf die Einhüllende der Blochfunktion, und stört die Relativbewegung nicht. In diesem Fall ist eine Trennung von Schwepunkts- und Relativkoordinaten möglich. In jenem Regime ist die Rydbergbindungsenergie größer als der Beschränkungseffekt. Die resultierenden Energien der gebundenen Exzitonenzustände in einem schwach beschränkendem Quantentopf betragen:

$$E_n^{3D,Q} = E_g - \frac{Ry^*}{(n-\delta_l)^2} + \underbrace{\frac{\hbar^2\pi^2}{2m_r}\left(\frac{j}{L_z}\right)^2}_{\Delta_{\text{conf}}}, \tag{A.1}$$

wobei Δ_{conf} den zusätzlichen quantisierten Energieterm darstellt, mit Quantenzustandsindex j und Quantentopfbreite L_z. Der Gesamteffekt ist abhängig von der Rydbergexzitonengröße, also von der Hauptquantenzahl n. Die Quantenbeschränkung unterdrückt die freie Bewegung und hat einen Einfluss auf die kinetische Energie des Quantenobjekts. Nur diskrete Werte sind erlaubt, was zu einer Serie von quantisierten Zuständen führt [93]. Eingeschlossen in einem Quantentopf, gewinnen Rydbergexzitonen Energie, erfahren also eine Blauverschiebung. Im schwachen Beschränkungsregime beträgt diese Blauverschiebung wenige bis wenige zehn Mikroelektronenvolt für den niedrigsten und dritten angeregten

Quantenzustandsindex j, und liegt somit in experimentell nachweisbaren Größenordnungen. Die Energieverschiebung kann über große Bereiche kontrolliert werden durch die Parameter Hauptquantenzahl n, Quantenzustandsindex j, und Quantentopfbreite L_z. Solche kontrollierbaren Energieverschiebungen können für die Realisierung von Quantentechnologien mit Rydbergexzitonen in Kupferoxydul genutzt werden [187].

Der Bereich, in dem die Energien verschoben werden können, kann vergrößert werden, indem man zu höheren Beschränkungen übergeht (mittleres oder starkes Beschränkungsregime in 2D). In der Berechnung für sehr kleine Quantentöpfe (starke Beschränkung) müssen folgende Aspekte in Betracht gezogen werden:
Erstens, die Exzitonenbindungsenergie in zwei Dimensionen ist gegeben durch:

$$E_B^{2D} = -\frac{Ry^*}{\left(n - 1/2\right)^2}. \tag{A.2}$$

Zweitens, die Permittivität außerhalb des Quantentopfes (Medium II) hat einen Einfluss auf Geschehnisse innerhalb des Quantentopfes (Medium I). Dadurch verändert sich die Bindungsenergie zu:

$$E_B^{2D*} = -\left(\frac{2\varepsilon}{\varepsilon_I + \varepsilon_{II}}\right)^2 \frac{Ry^*}{\left(n - 1/2\right)^2}. \tag{A.3}$$

Der wohl wichtigste Aspekt jedoch ist die Tatsache, dass das Exziton im Extremfall nicht mehr als Exziton sondern als Elektron und Loch separat, also mit einzeln quantisierten Bewegungen, betrachtet werden muss.
Um ein Gefühl dafür zu bekommen, wie sich die Energieverschiebung in Richtung des mittleren Beschränkungsregimes entwickeln ($L_z \approx 2r$), wenden wir das Modell für schwache Beschränkungen auf Exzitonen in mittleren Beschränkungen an. Wie erwartet, werden die Blauverschiebungen signifikant größer umso enger

der Quantentopf wird, und betragen bis zu mehreren zehn Millieketronenvolt. Im starken Beschränkungsregime würde die Beschränkungsenergie die Exzitonenbindungsenergie $Ry^* = 96\,\mathrm{meV}$ übersteigen. Höhere Beschränkungen können auch dadurch erreicht werden, dass das zu beschränkende Objekt in zwei oder drei Dimensionen eingeschränkt wird, also Rydbergexzitonen in Quantendrähten oder in Quantenpunkten. In solchen Strukturen wäre die Beschränkungsenergie gegeben durch:

$$\Delta^{1D}_{\mathrm{conf}} = \frac{\hbar^2\pi^2}{2m_r}\left(\frac{j_z^2}{L_z^2} + \frac{j_y^2}{L_y^2}\right) \xrightarrow{L_z=L_y} 2 \cdot \Delta^{2D}_{\mathrm{conf}} \tag{A.4}$$

und

$$\Delta^{0D}_{\mathrm{conf}} = \frac{\hbar^2\pi^2}{2m_r}\left(\frac{j_z^2}{L_z^2} + \frac{j_y^2}{L_y^2} + \frac{j_x^2}{L_x^2}\right) \xrightarrow{L_z=L_y=L_x} 3 \cdot \Delta^{2D}_{\mathrm{conf}}. \tag{A.5}$$

Die Blauverschiebung könnte demnach nochmals um einen Faktor von 2 und 3 verstärkt werden. Es ist jedoch noch unbekannt, wie sich die Rydbergbindungsenergie in solchen Strukturen verändern würde.

Jüngste Fortschritte in fokussierter Ionenstrahllithographie mit Au^+-Ionen (Raith IonLine) ermöglichen es, maßgefertigte Quantentöpfe mit Breiten von hunderten von Nanometern herzustellen. Demnach wäre es möglich, auch experimentell Rydbergexzitonen in Kupferoxydul-Quantentöpfen einzusperren. Die Hauptschwierigkeit liegt darin, die Quantentopfoberflächen glatt genug herzustellen, sodass das Kristallgitter, seine Symmetrie, und somit die Bildung von Exzitonen nicht durcheinandergebracht werden. Mit Pump-Probe-Spektroskopie hätte man zum ersten Mal die Möglichkeit solche großen Quantenobjekte in definierten, beschränkten Geometrien zu untersuchen.

BIBLIOGRAPHY

[1] J. Frenkel, *On the transformation of light into heat in solids. I*, Phys. Rev. **37**, 17–44 (1931).

[2] G. H. Wannier, *The structure of electronic excitation levels in insulating crystals*, Phys. Rev. **52**, 191 (1937).

[3] M. Hayashi, *Absorption spectra of cuprous oxide*, Prog. Theo. Phys. Suppl. **12**, 160–173 (1959).

[4] E. F. Gross, *Optical spectrum of excitons in the crystal lattice*, Suppl. Nuovo Cimento **4**, 672–701 (1956).

[5] J. C. Merle, C. Wecker, A. Daunois, J. L. Deiss, and S. Nikitine, *Modulated excitonic absorption on* Cu_2O *in magnetic or parallel electric and magnetic fields*, Surf. Sci. **37**, 347–354 (1973).

[6] M. Washington et al., *Spectroscopy of excited yellow exciton states in* Cu_2O *by forbidden resonant Raman scattering*, Phys. Rev. B **15**, 2145 (1977).

[7] S. Nikitine, J. B. Grun, and M. Sieskind, *Etude spectrophotometrique de la serie jaune de* Cu_2O *aux basses temperatures*, J. Phys. Chem. Solids **17**, 292–300 (1961).

[8] A. Werner and H. D. Hochheimer, *High-pressure x-ray study of* Cu_2O *and* Ag_2O, Phys. Rev. B **25**, 5929 (1982).

[9] G. M. Kavoulakis, Y.-C. Chang, and G. Baym, *Fine structure of excitons in* Cu_2O, Phys. Rev. B **55**, 7593 (1997).

[10] R. J. Elliott, *Intensity of optical absorption by excitons*, Phy. Rev. B **108**, 1384 (1957).

[11] V. T. Agekyan, B. S. Monozon, and I. P. Shiryapov, *The fine structure of Wannier-Mott excitons in a cubic crystal and its behaviour in an electric field*, Phys. Status Solidi B **66**, 359–370 (1974).

[12] H. Matsumoto, K. Saito, M. Hasuo, S. Kono, and N. Nagasawa, *Revived interest on yellow-exciton series in* Cu_2O *: An experimental aspect*, Solid State Commun. **97**, 125–129 (1996).

[13] D. Fröhlich, R. Kenklies, C. Uihlein, and C. Schwab, *Assignment of the even-parity excitons in cuprous oxide*, Phys. Rev. Lett. **43**, 1260–1263 (1979).

[14] C. Uihlein, D. Fröhlich, and R. Kenklies, *Investigation of exciton fine structure in* Cu_2O, Phys. Rev. B **23**, 2731 (1981).

[15] T. Kazimierczuk, D. Fröhlich, S. Scheel, H. Stolz, and M. Bayer, *Giant Rydberg excitons in the copper oxide* Cu_2O, Nature **514**, 343–347 (2014).

[16] F. Engel et al., *Observation of Rydberg blockade induced by a single ion*, Phys. Rev. Lett. **121**, 193401 (2018).

[17] J. Schmidt et al., *An optogalvanic gas sensor based on Rydberg excitations*, J. Phys. B **53**, 094001 (2020).

[18] C. Veit et al., *Pulsed ion microscope to probe quantum gases*, Phys. Rev. X **11**, 011036 (2021).

[19] F. Ripka, H. Kübler, R. Löw, and T. Pfau, *A room-temperature single-photon source based on strongly interacting Rydberg atoms*, Science **362**, 446–449 (2018).

[20] S. O. Krüger and S. Scheel, *Waveguides for Rydberg excitons in* Cu_2O *from strain traps*, Phys. Rev. B **97**, 205208 (2018).

[21] F. Schweiner, J. Main, M. Feldmaier, G. Wunner, and C. Uihlein, *Impact of the valence band structure of cuprous oxide on excitonic spectra*, Phys. Rev. B **93**, 195203 (2016).

[22] F. Schöne et al., *Coupled valence band dispersions and the quantum defect of excitons in* Cu_2O, J. Phys. B **49** (2016).

[23] F. Schöne et al., *Deviations of the exciton level spectrum in* Cu_2O *from the hydrogen series*, Phys. Rev. B **93**, 075203 (2016).

[24] J. Thewes et al., *Observation of high angular momentum excitons in cuprous oxide*, Phys. Rev. Lett. **115**, 027402 (2015).

[25] F. Schweiner et al., *Magnetoexcitons in cuprous oxide*, Phys. Rev. B **95**, 035202 (2016).

[26] M. Aßmann, J. Thewes, D. Fröhlich, and M. Bayer, *Quantum chaos and breaking of all anti-unitary symmetries in Rydberg excitons*, Nat. Mater. **15**, 741–745 (2016).

[27] P. Grünwald et al., *Signatures of quantum coherences in Rydberg excitons*, Phys. Rev. Lett. **117**, 133003 (2016).

[28] J. H. Koo and G. Cho, *Checkerboard patterns and magnetic resonance peak in cuprate superconductors*, Solid State Commun. **134**, 287–289 (2005).

[29] S. Zielińska-Raczyńska, G. Czajkowski, and D. Ziemkiewicz, *Optical properties of Rydberg excitons and polaritons*, Phys. Rev. B **93**, 075206 (2016).

[30] S. Zielińska-Raczyńska, D. Ziemkiewicz, and G. Czajkowski, *Electro-optical properties of Rydberg excitons*, Phys. Rev. B **94**, 045205 (2016).

[31] S. Zielińska-Raczyńska, D. Ziemkiewicz, and G. Czajkowski, *Magneto-optical properties of Rydberg excitons: Center-of-mass quantization approach*, Phys. Rev. B **95**, 075204 (2017).

[32] F. Schöne, H. Stolz, and N. Naka, *Phonon-assisted absorption of excitons in* Cu_2O, Phys. Rev. B **96**, 115207 (2017).

[33] D. Semkat, H. Fehske, and H. Stolz, *Influence of electron-hole plasma on Rydberg excitons in cuprous oxide*, Phys. Rev. B **100**, 155204 (2019).

[34] V. Walther, P. Grünwald, and T. Pohl, *Controlling exciton-phonon interactions via electromagnetically induced transparency*, Phys. Rev. Lett. **125**, 173601 (2020).

[35] A. Farenbruch, D. Fröhlich, D. R. Yakovlev, and M. Bayer, *Rydberg series of dark excitons in* Cu_2O, Phys. Rev. Lett. **125**, 207402 (2020).

[36] J. Mund, D. Fröhlich, D. R. Yakovlev, and M. Bayer, *High-resolution second harmonic generation spectroscopy with femtosecond laser pulses on excitons in* Cu_2O, Phys Rev B **98**, 085203 (2018).

[37] J. P. Rogers et al., *High-resolution nanosecond spectroscopy of even-parity Rydberg excitons in* Cu_2O, Phys. Rev. B **105**, 115206 (2022).

[38] L. A. Gallagher et al., *Microwave-optical coupling via Rydberg excitons in cuprous oxide*, Phys. Rev. Res. **4**, 013031 (2022).

[39] P. Rommel et al., *Second harmonic generation of cuprous oxide in magnetic fields*, Phys. Rev. B **101**, 115202 (2020).

[40] A. Farenbruch et al., *Magneto-Stark and Zeeman effect as origin of second harmonic generation of excitons in* Cu_2O, Phys. Rev. B **101**, 115201 (2020).

[41] N. Naka and N. Nagasawa, *Dynamics of paraexcitons generated in a 3D confined potential well by two-photon resonance excitation in* Cu_2O, J. Lumin. **94-95**, 413–416 (2001).

[42] N. Naka and N. Nagasawa, *Two-photon diagnostics of stress-induced exciton traps and loading of 1s-yellow excitons in* Cu_2O, Phys. Rev. B **65**, 075209 (2002).

[43] A. Konzelmann, B. Frank, and H. Giessen, *Quantum confined Rydberg excitons in reduced dimensions*, J. Phys. B **53**, 024001 (2020).

[44] S. Steinhauer et al., *Rydberg excitons in* Cu_2O *microcrystals grown on a silicon platform*, Commun. Mater. **1**, 1–7 (2020).

[45] A. M. Konzelmann, S. O. Krüger, and H. Giessen, *Interaction of OAM light with Rydberg excitons: Modifying dipole selection rules*, Phys. Rev. B **100**, 115308 (2019).

[46] S. O. Krüger, H. Stolz, and S. Scheel, *Interaction of charged impurities and Rydberg excitons in cuprous oxide*, Phys. Rev. B **101**, 235204 (2020).

[47] J. Heckötter, D. Janas, R. Schwartz, M. Aßmann, and M. Bayer, *Experimental limitation in extending the exciton series in* Cu_2O *towards higher principal quantum numbers*, Phys. Rev. B **101**, 235207 (2020).

[48] K. Orfanakis et al., *Rydberg exciton-polaritons in a* Cu_2O *microcavity*, Nat. Mater. **21**, 767–772 (2022).

[49] A. J. Ångström, *On the Fraunhofer-lines visible in the solar spectrum*, Philos. Mag. **24**, 1–11 (1862).

[50] J. J. Balmer, *Notiz über die Spectrallinien des Wasserstoffs*, Ann. d. Phys. u. Chem. N. F. XXV **7**, 80–87 (1884).

[51] J. R. Rydberg, *XXXIV. On the structure of the line-spectra of the chemical elements*, Lond. Edinb. Dubl. Philos. Mag. J. Sci. **29**, 331–337 (1890).

[52] N. Bohr, *I. On the constitution of atoms and molecules*, Lond. Edinb. Dubl. Philos. Mag. J. Sci. **26**, 1–25 (1913).

[53] B. Höglund and P. G. Mezger, *Hydrogen emission line n110 to n109: Detection at 5009 Megahertz in galactiv H II Regions*, Science **150**, 339–348 (1965).

[54] T. W. Hänsch, *Repetitively pulsed tunable dye laser for high resolution spectroscopy*, Appl. Opt. **11**, 895 (1972).

[55] T. F. Gallagher, *Rydberg atoms*, Rep. Prog. Phys. **51**, 143–188 (1988).

[56] S. Chu, *The manipulation of neutral particles*, Rev. Mod. Phys. **70**, 685–706 (1998).

[57] C. Cohen-Tannoudji, *Manipulating atoms with photons*, Rev. Mod. Phys. **70**, 707–719 (1998).

[58] W. D. Phillips, *Laser cooling and trapping of neutral atoms*, Rev. Mod. Phys. **70**, 721–741 (1998).

[59] T. F. Gallagher, *Rydberg Atoms* (Cambridge University Press, 1994).

[60] N. Sibalic and C. S. Adams, *Rydberg physics* (IOP Publishing, 2018).

[61] V. Bendkowsky et al., *Observation of ultralong-range Rydberg molecules*, Nature **458**, 1005–1008 (2009).

[62] S. Haroche, *Nobel lecture: Controlling photons in a box and exploring the quantum to classical boundary*, Rev. Mod. Phys. **85**, 1083–1102 (2013).

[63] D. Jaksch et al., *Fast quantum gates for neutral atoms*, Phys. Rev. Lett. **85**, 2208 (2000).

[64] M. D. Lukin et al., *Dipole blockade and quantum information processing in mesoscopic atomic ensembles*, Phys. Rev. Lett. **87**, 037901 (2001).

[65] M. Saffman, *Quantum computing with atomic qubits and Rydberg interactions: Progress and challenges*, J. Phys. B **49**, 1–24 (2016).

[66] K. Singer, M. Reetz-Lamour, T. Amthor, L. G. Marcassa, and M. Weidemüller, *Suppression of excitation and spectral broadening induced by interactions in a cold gas of Rydberg atoms*, Phys. Rev. Lett. **93**, 163001 (2004).

[67] D. Tong et al., *Local blockade of Rydberg excitation in an ultracold gas*, Phys. Rev. Lett. **93**, 063001 (2004).

[68] T. Peyronel et al., *Quantum nonlinear optics with single photons enabled by strongly interacting atoms*, Nature **57**, 8–11 (2012).

[69] O. Firstenberg et al., *Attractive photons in a quantum nonlinear medium*, Nature **502**, 71–75 (2013).

[70] S. Baur, D. Tiarks, G. Rempe, and S. Dürr, *Single-photon switch based on Rydberg blockade*, Phys. Rev. Lett. **112**, 073901 (2014).

[71] D. Tiarks, S. Baur, K. Schneider, S. Dürr, and G. Rempe, *Single-photon transistor using a Förster resonance*, Phys. Rev. Lett. **113**, 053602 (2014).

[72] H. Gorniaczyk, C. Tresp, J. Schmidt, H. Fedder, and S. Hofferberth, *Single-photon transistor mediated by interstate Rydberg interactions*, Phys. Rev. Lett. **113**, 053601 (2014).

[73] H. Labuhn et al., *Single-atom addressing in microtraps for quantum-state engineering using Rydberg atoms*, Phys. Rev. A **90**, 023415 (2014).

[74] L. Isenhower et al., *Demonstration of a neutral atom controlled-NOT quantum gate*, Phys. Rev. Lett. **104**, 010503 (2010).

[75] P. Schauß et al., *Observation of spatially ordered structures in a two-dimensional Rydberg gas*, Nature **491**, 87–91 (2012).

[76] T. Xia et al., *Randomized benchmarking of single-qubit gates in a 2D array of neutral-atom qubits*, Phys. Rev. Lett. **114**, 100503 (2015).

[77] H. Labuhn et al., *Tunable two-dimensional arrays of single Rydberg atoms for realizing quantum Ising models*, Nature **534**, 667–670 (2016).

[78] J. Ningyuan et al., *Observation and characterization of cavity Rydberg polaritons*, Phys. Rev. A **93**, 041802 (2016).

[79] H. Bernien et al., *Probing many-body dynamics on a 51-atom quantum simulator*, Nature **551**, 579–584 (2017).

[80] F. Meinert et al., *Indium tin oxide films meet circular Rydberg atoms: Prospects for novel quantum simulation schemes*, Phys. Rev. Res. **2**, 023192 (2020).

[81] Y. Y. Jau, A. M. Hankin, T. Keating, I. H. Deutsch, and G. W. Biedermann, *Entangling atomic spins with a Rydberg-dressed spin-flip blockade*, Nature **12**, 71–74 (2016).

[82] D. Tiarks, S. Schmidt, G. Rempe, and S. Dürr, *Optical π phase shift created with a single-photon pulse*, Sci. Adv. **2**, 1–6 (2016).

[83] J. Heckötter, *Strongly interacting Rydberg excitons in Cu_2O*, PhD thesis, Technische Universität Dortmund, 2020.

[84] J. E. Arem, *Color encyclopedia of gemstones* (Van Nostrand Reinhold, 1977).

[85] C. Klein and C. S. J. Hurlbut, *Manual of mineralogy* (John Wiley & Sons, Inc., 1985).

[86] S. A. Lynch et al.: *Giant Rydberg excitons in synthetic and artificial cuprous oxide*, 20^{th} International Conference on Transparent Optical Networks (ICTON), IEEE, 2018.

[87] S. A. Lynch et al., *Rydberg excitons in synthetic cuprous oxide (Cu_2O)*, Phys. Rev. Mater. **5**, 084602 (2021).

[88] G. F. Koster, J. O. Dimmock, R. G. Wheeler, and H. Statz, *Properties of the thirty-two point groups* (The MIT Press Research Monographs, 1963).

[89] R. J. Elliott, *Symmetry of excitons in Cu_2O*, Phys. Rev. **124**, 340 (1961).

[90] J. W. Hodby, T. E. Jenkins, C. Schwab, H. Tamura, and D. Trivich, *Cyclotron resonance of electrons and of holes in cuprous oxide, Cu_2O*, J. Phys. C **9**, 1429–1439 (1976).

[91] K. Suzuki and J. C. Hensel, *Quantum resonances in the valence bands of germanium. I. theoretical considerations*, Phys. Rev. B **9**, 4184 (1974).

[92] N. Peyghambarian, S. W. Koch, and A. Mysyrowiccz, *Introduction to semiconductor optics* (Prentice Hall, 1993).

[93] H. Haug and S. W. Koch, *Quantum theory of the optical and electronic properties of semiconductors* (World Scientific, 1993).

[94] P. Dawson, M. M. Hargreave, and G. R. Wilkinson, *The dielectric and lattice vibrational spectrum of cuprous oxide*, J. Phys. Chem. Solids **34**, 2201–2208 (1973).

[95] M. M. Beg and S. M. Shapiro, *Study of phonon dispersion relations in cuprous oxide by ineslastic neutron scattering*, Phys. Rev. B **13**, 1728 (1976).

[96] P. Y. Yu and Y. R. Shen, *Resonance Raman studies in Cu_2O. I. The phonon-assisted 1 s yellow excitonic absorption edge*, Phys. Rev. B **12**, 1377 (1975).

[97] P. Y. Yu and Y. R. Shen, *Resonance Raman studies in Cu_2O. II. The yellow and green excitonic series*, Phys. Rev. B **17**, 4017 (1978).

[98] P. Baumeister, *Optical absorption of cuprous oxide*, Phys. Rev. **121**, 359 (1961).

[99] Y. Toyozawa, *Further contribution to the theory of the line-shape of the exciton absorption band*, Prog. Theo. Phys. **27**, 89–104 (1962).

[100] Y. Toyozawa, *Interband effect of lattice vibrations in the exciton absorption spectra*, J. Phys. Chem. Solids **25**, 59–71 (1964).

[101] N. Naka, S. Hashimoto, and T. Ishihara, *Thin films of single-crystal cuprous oxide grown from the melt*, Jpn. J. Appl. Phys. **44**, 5096–5101 (2005).

[102] H. Stolz et al., *Coherent transfer matrix analysis of the transmission spectra of Rydberg excitons in cuprous oxide*, Phys. Rev. B **104**, 035206 (2021).

[103] V. Heine, *Group theory in quantum mechanics* (Pergamon, 1960).

[104] V. T. Agekyan, *Spectroscopic properties of semiconductor crystals with direct forbidden energy gap*, Phys. Status Solidi A **43** (1977).

[105] W. Demtröder, *Experimentalphysik 2: Elektrizität und Optik* (Springer-Verlag Berlin Heidelberg, 2006).

[106] J. D. Jackson and R. F. Fox, *Classical electrodynamics*, 3^{rd} *ed.* (American Association of Physics Teachers, 1999).

[107] S. A. Maier, *Plasmonics: Fundamentals and applications* (Springer, 2007).

[108] R. W. Boyd, *Nonlinear optics* (Elsevier Inc., 2008).

[109] M. Kira and S. W. Koch, *Semiconductor quantum optics* (Cambridge University Press, 2012).

[110] M. Padgett, J. Courtial, and L. Allen, *Light's orbital angular momentum*, Phys. Today **57**, 35 (2004).

[111] N. B. Simpson, K. Dholakia, L. Allen, and M. J. Padgett, *Mechanical equivalence of spin and orbital angular momentum of light: an optical spanner*, Opt. Lett. **22**, 52–54 (1997).

[112] N. R. Heckenberg, R. McDuff, C. P. Smith, H. Rubinsztein-Dunlop, and M. J. Wegener, *Laser beams with phase singularities*, Opt. Quant. Electron. **24**, 951–962 (1992).

[113] Y. Yan et al., *Efficient generation and multiplexing of optical orbital angular momentum modes in a ring fiber by using multiple coherent inputs*, Opt. Lett. **37**, 3645–3647 (2012).

[114] G. Turnbull, D. Robertson, G. Smith, L. Allen, and M. Padgett, *The generation of free-space Laguerre-Gaussian modes at millimetre-wave frequencies by use of a spiral phaseplate*, Opt. Commun. **127**, 183–188 (1996).

[115] L. Allen, M. W. Beijersbergen, R. J. C. Spreeuw, and J. P. Woerdman, *Orbital angular momentum of light and the transformation of Laguerre-Gaussian laser modes*, Phys. Rev. A **45**, 8185 (1992).

[116] G. Spektor et al., *Revealing the subfemtosecond dynamics of orbital angular momentum in nanoplasmonic vortices*, Science **355**, 1187–1191 (2017).

[117] M. Beijersbergen, R. Coerwinkel, M. Kristensen, and J. Woerdman, *Helical-wavefront laser beams produced with a spiral phaseplate*, Opt. Commun. **112**, 321–327 (1994).

[118] C. T. Schmiegelow and F. Schmidt-Kaler, *Light with orbital angular momentum interacting with trapped ions*, Eur. Phys. J. D **66**, 1–9 (2012).

[119] C. T. Schmiegelow et al., *Transfer of optical orbital angular momentum to a bound electron*, Nat. Commun. **7**, 1–6 (2016).

[120] A. Afanasev, C. E. Carlson, and A. Mukherjee, *High-multipole excitation of hydrogen-like atoms by twisted photons near a phase singularity*, J. Opt. **18**, 1–7 (2016).

[121] N. Rivera, I. Kaminer, B. Zhen, J. D. Joannopoulos, and M. Soljacic, *Shrinking light to allow forbidden transitions on the atomic scale*, Science **353**, 263–269 (2016).

[122] S. Franke-Arnold, *Optical angular momentum and atoms*, Phil. Trans. R. Soc. A **375**, 20150435 (2017).

[123] V. E. Lembessis and M. Babiker, *Enhanced quadrupole effects for atoms in optical lattices*, Phys. Rev. Lett. **110**, 083002 (2013).

[124] P. K. Jain, D. Ghosh, R. Baer, E. Rabani, and A. P. Alivisatos, *Near-field manipulation of spectroscopic selection rules on the nanoscale*, Proc. Natl. Acad. Sci. USA **109**, 8016–8019 (2012).

[125] G. Mie, *Beiträge zur Optik trüber Medien, speziell kolloidaler Metallösungen*, Ann. Phys. **3**, 377–445 (1908).

[126] L. Novotny and N. Van Hulst, *Antennas for light*, Nat. Photonics **5**, 83–90 (2011).

[127] S. B. Hasan, F. Lederer, and C. Rockstuhl, *Nonlinear plasmonic antennas*, Mater. Today **17**, 478–485 (2014).

[128] M. Hentschel, *Complex 2D & 3D plasmonic nanostructures: Fano resonances, chirality, and nonlinearities*, PhD thesis, University of Stuttgart, 2013.

[129] N. C. Panoiu, W. E. Sha, D. Y. Lei, and G. C. Li, *Nonlinear optics in plasmonic nanostructures*, J. Opt. **20** (2018).

[130] I. Zorić, B. Kasemo, C. Langhammer, and M. Zaaach, *Nanodisk plasmons: Material damping mechanisms*, ACS Nano **5**, 2535–2546 (2011).

[131] B. Metzger, M. Hentschel, M. Lippitz, and H. Giessen, *Third-harmonic spectroscopy and modeling of the nonlinear response of plasmonic nanoantennas*, Opt. Lett. **37**, 4741 (2012).

[132] G. Albrecht, M. Hentschel, S. Kaiser, and H. Giessen, *Hybrid organic-plasmonic nanoantennas with enhanced third-harmonic generation*, ACS Omega **2**, 2577–2582 (2017).

[133] K. D. Ko et al., *Nonlinear optical response from arrays of Au bowtie nanoantennas*, Nano Lett. **11**, 61–65 (2011).

[134] M. Hentschel et al., *Three-dimensional chiral plasmonic oligomers*, Nano Lett., 2542–2547 (2012).

[135] N. Feth et al., *Second-harmonic generation from complementary split-ring resonators*, Opt. Lett. **33**, 1975 (2008).

[136] F. B. P. Niesler et al., *Second-harmonic generation from split-ring resonators on a GaAs substrate*, Opt. Lett. **34**, 1997 (2009).

[137] S. Linden et al., *Collective effects in second-harmonic generation from split-ring-resonator arrays*, Phys. Rev. Lett. **109**, 015502 (2012).

[138] C. Menzel et al., *Asymmetric transmission of linearly polarized light at optical metamaterials*, Phys. Rev. Lett. **104**, 253902 (2010).

[139] N. Liu, H. Liu, S. Zhu, and H. Giessen, *Stereometamaterials*, Nat. Photonics **3**, 157–162 (2009).

[140] Y. Zhang, N. K. Grady, C. Ayala-Orozco, and N. J. Halas, *Three-dimensional nanostructures as highly efficient generators of second harmonic light*, Nano Lett. **11**, 5519–5523 (2011).

[141] M. Decker et al., *Strong optical activity from twisted-cross photonic metamaterials*, Opt. Lett. **34**, 2501 (2009).

[142] C. Helgert et al., *Chiral metamaterial composed of three-dimensional plasmonic nanostructures*, Nano Lett. **11**, 4400–4404 (2011).

[143] L. Novotny and B. Hecht, *Principle of nano-optics* (Cambridge University Press, 2012).

[144] L. Novotny, *Effective wavelength scaling for optical antennas*, Phys. Rev. Lett. **98**, 266802 (2007).

[145] M. Hentschel, T. Utikal, H. Giessen, and M. Lippitz, *Quantitative modeling of the third harmonic emission spectrum of plasmonic nanoantennas*, Nano Lett. **12**, 3778–3782 (2012).

[146] B. Metzger, *Ultrafast nonlinear plasmonics from dipole nanoantennas to hybrid complex plasmonic structures*, PhD thesis, University of Stuttgart, 2014.

[147] T. Hanke et al., *Tailoring spatiotemporal light confinement in single plasmonic nanoantennas*, Nano Lett. **12**, 992–996 (2012).

[148] E. Ringe, B. Sharma, A. I. Henry, L. D. Marks, and R. P. Van Duyne, *Single nanoparticle plasmonics*, Phys. Chem. Chem. Phys. **15**, 4110–4129 (2013).

[149] R. Taubert, M. Hentschel, and H. Giessen, *Plasmonic analog of electromagnetically induced absorption: simulations, experiments, and coupled oscillator analysis*, J. Opt. Soc. Am. B **30**, 3123 (2013).

[150] A. Aubry, D. Y. Lei, S. A. Maier, and J. B. Pendry, *Plasmonic hybridization between nanowires and a metallic surface: A transformation optics approach*, ACS Nano **5**, 3293–3308 (2011).

[151] E. Prodan, C. Radloff, N. J. Halas, and P. Nordlander, *A hybridization model for the plasmon response of complex nanostructures*, Science **302**, 419–422 (2003).

[152] P. Nordlander, C. Oubre, E. Prodan, K. Li, and M. I. Stockman, *Plasmon hybridization in nanoparticle dimers*, Nano Lett. **4**, 899–903 (2004).

[153] N. Liu and H. Giessen, *Coupling effects in optical metamaterials*, Angew. Chem. Int. Ed. **49**, 9838–9852 (2010).

[154] J. Heckötter et al., *Rydberg excitons in the presence of an ultralow-density electron-hole plasma*, Phys. Rev. Lett. **121**, 097401 (2018).

[155] T. Weiss, G. Granet, N. A. Gippius, S. G. Tikhodeev, and H. Giessen, *Matched coordinates and adaptive spatial resolution in the Fourier modal method*, Opt. Express **17**, 8051 (2009).

[156] T. Weiss, N. A. Gippius, S. G. Tikhodeev, G. Granet, and H. Giessen, *Derivation of plasmonic resonances in the Fourier modal method with adaptive spatial resolution and matched coordinates*, J. Opt. Soc. Am. A **28**, 238–244 (2011).

[157] D. Dregely, F. Neubrech, H. Duan, R. Vogelgesang, and H. Giessen, *Vibrational near-field mapping of planar and buried three-dimensional plasmonic nanostructures*, Nat. Commun. **4** (2013).

[158] B. Metzger et al., *Doubling the efficiency of third harmonic generation by positioning*, Nano Lett. **14**, 2867–2872 (2014).

[159] C. Zhu and M. J. Panzer, *Etching of electrodeposited Cu_2O films using ammonia solution for photovoltaic applications*, Phys. Chem. Chem. Phys. **18**, 6722–6728 (2016).

[160] Q. Hua, K. Chen, S. Chang, Y. Ma, and W. Huang, *Crystal plane-dependent compositional and structural evolution of uniform Cu_2O nanocrystals in aqueous ammonia solutions*, J. Phys. Chem. C **115**, 20618–20627 (2011).

[161] Q. Hua et al., *Morphological evolution of Cu_2O nanocrystals in an acid solution: Stability of different crystal planes*, Langmuir **27**, 665–671 (2011).

[162] J. Pal et al., *Crystal-plane-dependent etching of cuprous oxide nanoparticles of varied shapes and their application in visible light photocatalysis*, J. Phys. Chem. C **117**, 24640–24653 (2013).

[163] S. M. Lloyd, M. Babiker, and J. Yuan, *Interaction of electron vortices and optical vortices with matter and processes of orbital angular momentum exchange*, Phys. Rev. A **86**, 023816 (2012).

[164] G. F. Quinteiro, F. Schmidt-Kaler, and C. T. Schmiegelow, *Twisted-light-ion interaction: The role of longitudinal fields*, Phys. Rev. Lett. **119**, 253203 (2017).

[165] A. Syouji, S. Saito, and A. Otomo, *Creation of excitons excited by light with a spatial mode*, J. Phys. Soc. Jpn. **86**, 1–6 (2017).

[166] J. Heckötter et al., *High-resolution study of the yellow excitons in Cu_2O subject to an electric field*, Phys. Rev. B **95**, 035210 (2017).

[167] T. Kitamura, M. Takahata, and N. Naka, *Quantum number dependence of the photoluminescence broadening of excitonic Rydberg states in cuprous oxide*, J. Lumin. **192**, 808–813 (2017).

[168] V. Walther and T. Pohl, *Plasma-enhanced interaction and optical nonlinearities of Cu_2O Rydberg excitons*, Phys. Rev. Lett. **125**, 097401 (2020).

[169] S. Reich, N. S. Mueller, and M. Bubula, *Selection rules for structured light in nanooligomers and other nanosystems*, ACS Photonics **7**, 1537–1550 (2020).

[170] T. Arikawa et al., *Transfer of orbital angular momentum of light to plasmonic excitations in metamaterials*, Sci. Adv. **6**, 1–7 (2020).

[171] C. D. Aiello et al., *A chirality-based quantum leap*, ACS nano **16**, 4989–5035 (2022).

[172] A. Neubauer et al., *Spectroscopy of nanoantenna-covered Cu_2O: Towards enhancing quadrupole transitions in Rydberg excitons*, Phys. Rev. B **106**, 165305 (2022).

[173] A. Mokhberi, M. Hennrich, and F. Schmidt-Kaler, *Trapped Rydberg ions: A new platform for quantum information processing*, Adv. At. Mol. Opt. Phys. **69**, 233–306 (2020).

[174] A. N. Poddubny and M. M. Glazov, *Polarized edge state emission from topological spin phases of trapped Rydberg excitons in Cu_2O*, Phys. Rev. B **102**, 125307 (2020).

[175] M. Takahata, K. Tanaka, and N. Naka, *Nonlocal optical response of weakly confined excitons in Cu2 O mesoscopic films*, Phys. Rev. B **97**, 205305 (2018).

[176] K. Orfanakis et al., *Quantum confined Rydberg excitons in Cu_2O nanoparticles*, arXiv preprint arXiv:2011.12006v3 (2021).

[177] H. Ishihara et al., *Large four-wave mixing of spatially extended excitonic states in thin GaAs layers*, Phys. Rev. Lett. **89**, 017402 (2002).

[178] D. Fröhlich et al., *Coherent propagation and quantum beats of quadrupole polaritons in Cu_2O*, Phys. Rev. Lett., 2343.

[179] G. Malpuech, A. Kavokin, and G. Panzarini, *Propagation of exciton polaritons in inhomogeneous semiconductor films*, Phys. Rev. B **60**, 16788 (1999).

[180] E. S. Khramtsov et al., *Radiative decay rate of excitons in square quantum wells: Microscopic modeling and experiment*, J. Appl. Phys. **119**, 184301 (2016).

[181] T. Itoh, M. Furumiya, and T. Ikehara, *Size-dependent radiative decay time of confined excitons in CuCl microcrystals*, Solid State Commun. **73**, 271 (1990).

[182] D. B. Thoai, Y. Z. Hu, and S. W. Koch, *Influence of the confinement potential on the electron-hole-pair states in semiconductor microcrystallites*, Phys. Rev. B **42**, 11261 (1990).

[183] G. Einevoll, *Confinement of excitons in quantum dots*, Phys. Rev. B **45**, 3410 (1992).

[184] L. Bányai and S. W. Koch, *Semiconductor quantum dots* (World Scientific, 1993).

[185] G. Bastard, E. Mendez, L. Chang, and L. Esaki, *Exciton binding energy in quantum wells*, Phys. Rev. B **26**, 1974 (1982).

[186] G. Bastard, *Wave mechanics applied to semiconductors* (Halsted Press, 1988).

[187] M. Saffman, T. G. Walker, and K. Mølmer, *Quantum information with Rydberg atoms*, Rev. Mod. Phys. **82**, 2313–2363 (2010).

[188] A. Chernikov et al., *Exciton binding energy and nonhydrogenic Rydberg series in monolayer WS_2*, Phys. Rev. Lett. **113**, 076802 (2010).

[189] J. H. Grönqvist, T. Stroucken, G. Berghäuser, and S. W. Koch, *Excitons in graphene and the influence of the dielectric environment*, arXiv preprint arXiv:1107.5653v1 (2011).

[190] M. Aßmann and M. Bayer, *Semiconductor Rydberg Physics*, Adv. Quantum Technol. **3**, 1900134 (2020).

[191] D. Ziemkiewicz, K. Karpiński, G. Czajkowski, and S. Zielińska-Raczyńska, *Excitons in Cu_2O: From quantum dots to bulk crystals and additional boundary conditions for Rydberg exciton-polaritons*, Phys. Rev. B **101**, 205202 (2020).

[192] C. Morin et al., *Self-Kerr effect across the yellow Cu_2O Rydberg series*, arXiv preprint arXiv:2202.09239 (2022).

[193] M. Khazali and K. Heshami, *Single-photon source based on Rydberg exciton blockade*, J. Phys. B **50**, 215301 (2017).

[194] M. A. Versteegh et al., *Giant Rydberg excitons in Cu_2O probed by photoluminescence excitation spectroscopy*, Phys. Rev. B **104**, 245206 (2021).

ACKNOWLEDGMENT

The past few years have been an eventful time of my life. And, in particular, the past few months have been very demanding. I am deeply grateful to many people that supported me during this time.

I thank Prof. Dr. Harald Giessen for accepting me as a PhD student and for offering me to work on the research topic *Rydberg excitons in cuprous oxide.* I thank him for his ideas and advices, and for sending me to many national and international conferences. I thank Prof. Dr. Tilman Pfau for creating the amazing Rydberg community within the DFG funding program *GiRyd*, opening up many possibilities for discussion and scientific exchange. I thank Prof. Dr. Peter Michler for agreeing to be my second examiner and Prof. Dr. Maria Daghofer for being head of the examination board.

I thank Dr. Christine von Rekowski for her support in many administrative matters and Michael Kube for providing help during the lab setup. I thank the mechanical workshop for their quick processing of mechanical components and their always helpful advice with mechanical drawings. I thank the low-temperature workshop for supplying liquid Helium and for their readiness to help with any low-temperature issues.

I thank Arnold Weible, Gabriele Untereiner, and Dirk Schemionek for their help with crystal orientation, slicing, and polishing, as well as Dr. Mario Hentschel, Monika Ubl, Dr. Bettina Frank, Dr. Simon

Ristok, and Dr. Ksenia Weber for help with sample structuring.

I thank Prof. Dr. Manfred Bayer, Prof. Dr. Marc Assmann, and Dr. Julian Heckötter for sharing their ideas in scientific discussions and for supporting measurements. I thank Prof. Dr. Tim Davis for his advice in conducting experiments.

I thank my colleagues for a comfortable working atmosphere and a pleasant time at the 4th Physics Institute, and, in particular, Dr. Mario Hentschel, Dr. Joachim Krauth, Dr. Julian Karst, Dr. Simon Ristok, Moritz Flöß, and Philipp Flad for many exciting scientific and lovely non-scientific discussions, as well as mental support during the past months.

Last but not least I am eternally grateful for the constant support my family gives me. I thank my parents for giving me the chance to study physics and making a Ph.D. I thank them for their constant support and encouragement with studies, travels, work, and children. I thank my husband for giving me strength and encouragement, whenever I was stuck in one of the *deep valleys of tears of a Ph.D.*, and for constantly supporting me, in particular, for lately taking care of all family duties at home, while I was writing this thesis and preparing for the final examination. I thank my dearly loved children for being so wonderful little persons and for being patient with me most of the time.